Quantum gases in optical lattices: the atomic Mott insulator

Dries van Oosten

Oosten van, Dries

Quantum gases in optical lattices: the atomic Mott insulator
D. van Oosten - Utrecht
Universiteit Utrecht
Faculteit Natuur- en Sterrenkunde
Thesis Universiteit Utrecht - With a summary in Dutch
ISBN 90-393-3776-4
Subject heading: atomic physics / laser cooling / Bose-Einstein condensation
Druk: PrintPartners Ipskamp, Enschede

Quantum gases in optical lattices: the atomic Mott insulator

Quantumgassen in optische roosters:
de atomaire Mott-isolator

(met een samenvatting in het Nederlands)

PROEFSCHRIFT

ter verkrijging van de graad van doctor
aan de Universiteit Utrecht op gezag van
de Rector Magnificus, Prof. Dr. W.H. Gispen,
ingevolge het besluit van het College voor Promoties
in het openbaar te verdedigen
op maandag 13 september 2004
des ochtends te 10:30 uur

door

Dries van Oosten

geboren op 23 januari 1976, te Utrecht

Promotoren: Prof. Dr. Ir. H. T. C. Stoof
Prof. Dr. P. van der Straten

Faculteit Natuur- en Sterrenkunde
Universiteit Utrecht

Contents

Chapter 1

Introduction

1.1 Optical lattices

In 1992 Jessen *et al.* [1] proved that the motion of atoms in a standing light field is quantized, thus creating what is known now as a one-dimensional optical lattice. In more detail, this was achieved by collecting rubidium atoms in a magneto-optical trap (MOT) and switching on the laser light of the standing wave. Due to the light shift the atoms are trapped at the (anti-)nodes of the standing wave [2]. Subsequently, Grynberg *et al.* [3] showed that atoms could also be trapped in two- and three-dimensional optical lattices. As the density of lattice sites in the two- and three-dimensional case is high compared to the density of atoms, only a small fraction of the lattice sites is occupied. However, since the achievement

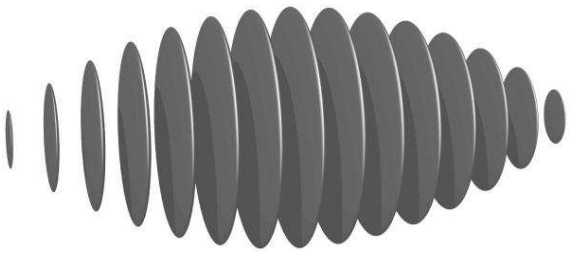

Figure 1.1: Graphical representation of the atomic density in a one-dimensional optical lattice.

of Bose-Einstein condensation [4, 5, 6], optical lattices have also been used to split a harmonically trapped condensate into an one-dimensional array

of disk-shaped condensates [7], as illustrated in Fig. 1.1. In this situation, the average occupation number is a few hundred atoms per lattice site. The aspect ratio of the disks is large, as the thickness of the disks is of the order of the wave length of the laser light and the diameter is of the order of the width of the laser beams. In a two-dimensional lattice the atoms are confined in cigar-shaped traps. When such a lattice is loaded from a MOT, the average occupation number is now a few percent, but loaded from a condensate, the average occupation number is on the order of 10-20 atoms per site. This situation is illustrated in Fig. 1.2. Loading a three-

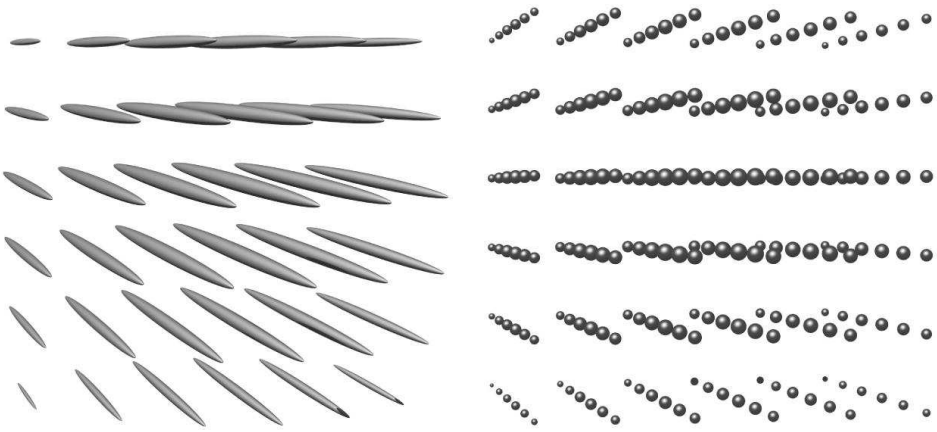

Figure 1.2: Graphical respresentation of the atomic density in a two-dimensional (left figure) and a three-dimensional (right figure) optical lattice.

dimensional optical lattice is only feasible starting from a Bose-Einstein condensate, as even with such a high density, at maximum a few atoms per site can be loaded into the lattice. It should be noted that although the average occupation number per site is much lower in the three-dimensional case than in the one-dimensional case, the number of lattice sites that is occupied increases dramatically. This means that in practice, one-, two- and three-dimensional lattice can be loaded with the same total number of atoms. Besides the simple square and cubic lattices shown in Fig. 1.2 it is also possible to create other structures, such as face-centered-cubic, body-centered-cubic and two-dimensional hexagonal lattices.

1.2 Quantum phase transitions

In the three-dimensional periodic potential mentioned in the previous section, it is experimentally possible to confine a few atoms per lattice site. This offers the possibility of performing molecular spectroscopy experiments using, for instance, photo-association. Besides these spectroscopic measurements, atoms in an optical lattice are an excellent model system for solid-state-like physics. For instance, cesium atoms in a one-dimensional optical lattice have been used to measure Bloch oscillations by Dahan *et al.* [8]. These oscillations cannot be measured in natural crystals, because of the impurities that are always present in such a crystal. Bloch oscillations have been observed only very indirectly in superlattice structures that have been grown especially for this purpose. With optical lattices, the Bloch oscillations can be measured directly using time-of-flight measurements.

The fact that these measurements are more easily done in optical lattices than in true solid-state systems is due to a number of reasons, but most importantly because the energy scales, such as the lattice depth and the temperature of the atoms, are easily accesible to the experimentalist. Furthermore, as all neccesary microscopic details about the lattice and about the atoms are known, a theoretical description of the system can be given from first principles. As a result it is much easier to make predictions and to make a good analyses of experimental results. In short, the methods of solid-state physics are more easily applied to atoms in optical lattices than to true solid-state systems.

An example of this is the application of the so-called Bose-Hubbard model to atoms in an optical lattice, as was done in 1998 by Jaksch *et al.* [9]. This model had been very well studied by Fisher *et al.* [10], who used it to predict the behaviour of superfluid helium in porous media such as Vycor. Jaksch *et al.* calculated that, when a sufficiently deep optical lattice is applied to an harmonically trapped gas of bosonic atoms, a phase transition can be achieved from a superfluid phase to an insulating phase. The reason that this phase transition occurs can be qualitatively understood as follows. When an optical lattice is loaded from a Bose-Einstein condensate, the density of the atoms can be chosen such that there is on average exactly one particle at each lattice sites. When the lattice potential is relatively weak, the atoms can tunnel between the lattice sites and it can be shown that in this case, the atoms are still in a superfluid phase. However, when the lattice potential is very large, two atoms on the same lattice site have

a very large interaction energy, as their relative distance is on average very small. This means that tunneling between the lattice sites is strongly suppressed, because an atom that tunnels to a neighbouring site has a high probability of encountering another atom. As shown by Fisher *et al.* this phase transition is a quantum phase transition, which means it occurs only at zero temperature and is driven by competing terms in the ground-state energy of the system, as opposed to competing terms in the free energy. This so-called superfluid to Mott insulator phase transition will be the focus of this thesis. An in-depth description of quantum phase transitions in general is given in Ref. [11].

1.3 Outlook

In this thesis, both experimental and theoretical work is presented. Chapter 2 contains an overview of the atomic physics and solid-state physics necessary to understand the behaviour of atoms in an optical lattice. Furthermore, a derivation of the Bose-Hubbard model is given. The experimental work is described in Chapter 3 and consists mainly of an introduction to the experimental setup that is presently being built in the lab and of the absorption-imaging setup that is used to analyse the atom cloud. A discussion is given of as many intermediate results as were available at the time this thesis was written. A more thorough description of the experimental setup will ultimately be given in Ref. [12].

The remainder of this thesis consists of theoretical work. In Chapters 4 and 5 theoretical techniques are developed to describe both the superfluid phase and the Mott-insulating phase of atoms in an optical lattice. In Chapter 4 the theory to describe the properties of the phase transition is derived and in Chapter 5 it is generalized to lower-dimensional lattices, where there are no longer a few atoms on every site, but rather a Bose-Einstein condensate containing hundreds of atoms. In Chapter 6 the theory developed in Chapter 4 is used to calculate the light-scattering properties of the Mott-insulating state and it is shown that these properties can be used as a probe for the behaviour of the particle-hole gap of the Mott insulator. Spectra are calculated for the two-photon scattering rate in a Bragg-spectroscopy experiment. Chapter 7 elaborates on the subject of Chapter 6, by giving derivations for the more technical parts of the calculations involved.

Chapter 2

Optical lattices and the Bose-Hubbard model

Abstract

We present some theoretical aspects of optical lattices and discuss their practical implications. First, the solid-state physics, such as the band structure and crystallography is discussed, assuming non-interacting atoms. Second, the effects of interactions between the atoms are incorporated, which leads to a description in terms of the Bose-Hubbard model.

2.1 Atomic physics

The force that light exerts on atoms can be split into two catagories, the radiation force and the dipole force. The radiation force is the force due to the scattering of photons from a laser beam. Photons are absorbed from the laser beam and subsequently emitted symmetrically, resulting in an average force in the direction of the laser beam. Because this force depends on the process of spontaneous emission, it is necessarily non-conservative, which means one cannot associate a potential to this force. Although the radiation force is an important tool in laser cooling, it will not be discussed in more detail here.

The dipole force is caused by the fact that the ground and excited-state energies of the atom shift due to the presence of the light. This force does

not require spontaneous emission, but it does require a gradient in the intensity of the light. By using a large light intensity and a frequency that is far from the atomic resonance, it is possible to obtain a large force, while simultaneously making the contribution of spontaneous emission small. This means that this force is to a good approximation conservative and a potential energy can be associated with it. By using a standing wave of light that obeys the criteria of high intensity and large detuning, one can thus create a periodic potential for atoms with a lattice spacing equal to half the wave length of the light used to create the standing wave and with potentially large trapping frequencies as compared to magnetic traps.

2.1.1 Light shift and spontaneous emission

The optical potential of a standing wave is related to the light shift. For a detuning δ, a natural line width Γ, and a position-dependent Rabi frequency $\Omega(\mathbf{r})$, the light shift $E_{\mathrm{ls}}(\mathbf{r})$ can be written as [2]

$$\begin{aligned} E_{\mathrm{ls}}(\mathbf{r}) &= \frac{\hbar\delta}{1+4(\delta/\Gamma)^2}\left(\frac{\Omega(\mathbf{r})}{\Gamma}\right)^2 \\ &= \frac{1}{2}\frac{\hbar\delta s_0(\mathbf{r})}{1+4(\delta/\Gamma)^2}, \end{aligned} \tag{2.1}$$

where s_0 is the on-resonance saturation parameter. The force acting on the atom can be written as $\mathbf{F}(\mathbf{r}) = -\nabla E_{\mathrm{ls}}(\mathbf{r})/(1+s(\mathbf{r}))$, where $s(\mathbf{r}) = s_0(\mathbf{r})/(1+4(\delta/\Gamma)^2)$ is the off-resonance saturation parameter. Note that the factor $1/(1+s)$ accounts for the fact that in general the atom undergoes cycles of absorption and spontaneous emission, which means that the force on the atom is an average of the force in the ground state and in the excited state. For a conservative force we can write $\mathbf{F}(\mathbf{r}) = -\nabla U(\mathbf{r})$, which means that in general the potential is given by $U(\mathbf{r}) = \hbar\delta\log(1+s(\mathbf{r}))/2$. However, in experiments the saturation parameter is usually taken to be very small, so we can write $U(\mathbf{r}) = E_{\mathrm{ls}}(\mathbf{r}) = \hbar\delta s(\mathbf{r})/2$. The other important parameter is the photon scattering rate, which is given by

$$\Gamma_{\mathrm{sc}} = \frac{1}{2}\frac{s\Gamma}{1+s}, \tag{2.2}$$

and which reduces to $\Gamma_{\mathrm{sc}} = s\Gamma/2$ for low saturation. This implies that in order to have a low rate of spontaneous emission, the saturation parameter

must be reduced, while keeping the light shift large. For large detuning δ and saturation s_0 the light shift scales as $E_{\mathrm{ls}} \propto s_0/\delta$ and the scattering rate as $\Gamma_{\mathrm{sc}} \propto s_0/\delta^2$. So in the limit of $\delta, s_0 \to \infty$ with $s_0/\delta = \mathrm{const}$, a deep lattice can be created with a negligible rate of spontaneous emission.

2.2 Crystalography of an optical lattice

The simplest optical lattice is a single standing wave of linearly polarized light. A standing wave is only periodic in one direction. For light detuned to the red of the atomic transition, confinement in the directions perpendicular to the laser beams is provided by the waist of the laser beams. A graphical representation of a one-dimensional lattice is shown in Fig. 2.1. Note that the aspect ratio of the trap is understated in this figure. In a typical experiment, the waist of the laser beam is on the order of $50\,\mu$m and the lattice spacing is half the wave length of the laser light, which corresponds to roughly 300 nm for the case of sodium. Potentials such as the one illustrated

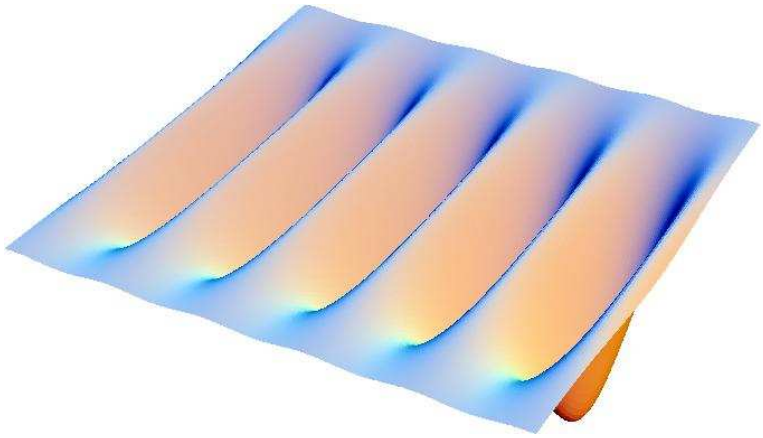

Figure 2.1: Graphical representation of a one-dimensional lattice.

in Fig. 2.1 have been used succesfully to trap cold atoms in several groups, since it is relatively easy to reach an average occupation number of a few particles per site, starting from atoms in a magneto-optical trap. Starting from a Bose-Einstein condensate an average occupation number of up to 100 particles per site can be achieved [7].

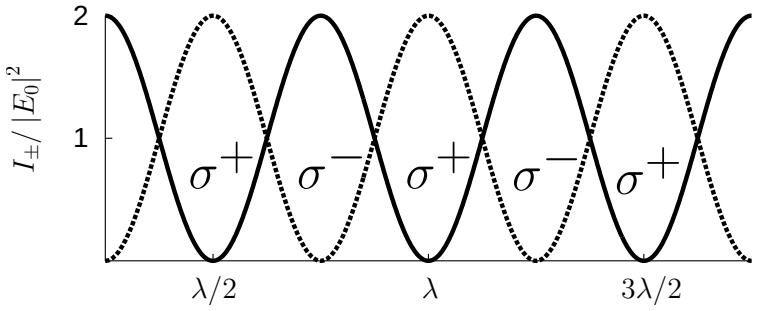

Figure 2.2: The intensity of the σ^+ and σ^- components of the standing wave relative to the intensity of one laser beam.

2.2.1 Polarization

The simplest generalization of the above situation is to use a so-called lin⊥lin configuration. In that configuration the polarization vectors of the two lasers that form the optical lattice, are both linear, but perpendicular to each other. In that case the polarization is not constant along the standing wave. If near-resonant laser beams are used, this property gives rise to polarization gradient cooling [2]. Here, only the case of large detuning is discussed, since this is most relevant for our purposes. If we denote the electric field due to one of the lasers by $\mathbf{E}_\mathrm{l}$ and the field due to the counterpropagating laser as $\mathbf{E}_\mathrm{r}$ and assume that the beams have the same transverse profile $E_0(x, y)$, the electric-field components can be written as

$$\begin{aligned}\mathbf{E}_\mathrm{l}(\mathbf{r}, t) &= E_0(x, y)\mathbf{e}_x e^{i(kz-\omega t)} + c.c.,\\ \mathbf{E}_\mathrm{r}(\mathbf{r}, t) &= E_0(x, y)\mathbf{e}_y e^{-i(kz+\omega t)} + c.c.,\end{aligned} \tag{2.3}$$

where $\mathbf{e}_x$ and $\mathbf{e}_y$ are unit vector in the x and y direction, respectively. To determine the polarization at every point along the standing wave, we define circular polarization vectors $\mathbf{e}_\pm = (\mathbf{e}_x \pm i\mathbf{e}_y)/\sqrt{2}$ Using this definition we find that the circularly polarized components of the electric field are given

by

$$E_{\pm}(\mathbf{r}) = \frac{E_0(x,y)}{\sqrt{2}}\left(e^{ikz} \mp ie^{-ikz}\right)$$
$$= \frac{E_0(x,y)}{\sqrt{2}}e^{ikz}\left(1 \pm e^{-2ikz'}\right), \tag{2.4}$$

where $z' = z - \pi/4k$. Using these equations we find that the intensities $I_{\pm}$ of the circularly polarized components are given by

$$I_{\pm}(\mathbf{r}) = |E_0(x,y)|^2\left(1 \pm \cos 2kz'\right). \tag{2.5}$$

This means that the intensity maxima for the σ^+ component of the light are at $kz'_+ = 0, \pi, ...$ whereas for the σ^- component the maxima are at $kz'_- = \pi/2, 3\pi/2, ...$. In Fig. 2.2 it is shown that the lattice spacing is still $\lambda/2$ and that the potential well depth for both the circulair polarizations is the same. However the maxima for σ^+ and σ^- are shifted by a distance $\lambda/4$ with respect to each other. This feature has been used to spin selectively transport rubidium atoms through an optical lattice [13].

2.2.2 Two-dimensional lattices

The above discussion applies only to one-dimensional lattices, but there are several ways of generalizing the laser configuration to two-dimensional structures. The naive approach is to simply superimpose two standing waves. However, such a configuration is not stable with respect to changes

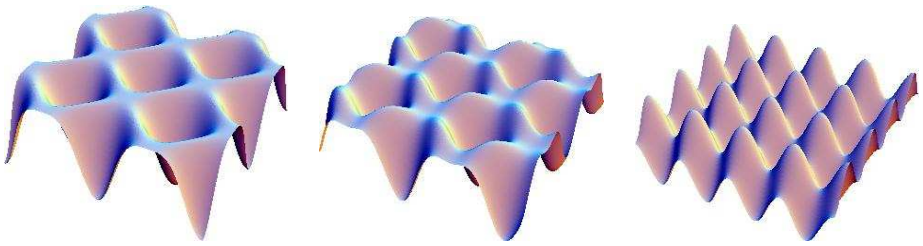

Figure 2.3: Graphical representation of the trapping potential in a two-dimensional optical lattice using four laser beams, where the phase of one of the beams is varied from 0 (left), through $\pi/2$ (center) to π (right).

in the relative phase of the laser beams, as is illustrated in Fig. 2.3. From this figure it is evident that using this configuration can be very problematic experimentally, as it takes for instance only the movement of one mirror by a distance of half a wave length to cause the potential to change from the left-most situation to the right-most situation. One way to solve this problem is to measure the relative phase of the laser beams and using a feedback loop to control them, as was achieved by Greiner *et al.* [14]. A second, much simpler approach is to give the two standing waves a frequency offset. In this way the standing waves are effectively decoupled, as the interference patterns moves much to fast for the atoms to follow [15]. A third approach

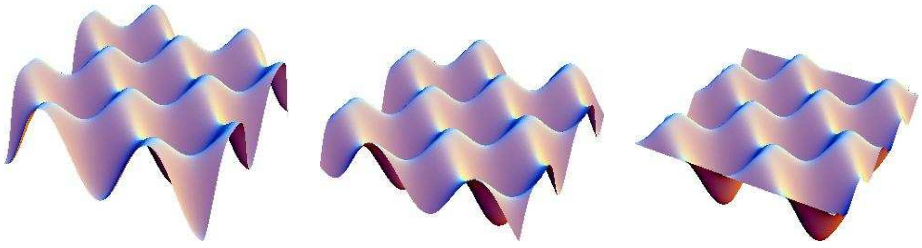

Figure 2.4: Graphical representation of the trapping potential in a two-dimensional optical lattice using three laser beams, where the phase of one of the beams is varied from 0 (left), through $\pi/2$ (center) to π (right).

due to Petsas *et al.* [16] is to use only three laser beams. In that case there are only two relative phases between the laser beams, which means that any fluctuation in the phases results in a translation of the lattice and not in a deformation. In Fig. 2.4 the potential is shown for the configuration where there is a standing wave in one direction and a single travelling wave from a direction perpendicular to the standing wave. It can be seen that there is indeed no deformation of the lattice, and that there is only a translation. This translation can also be a problem, as the atoms are shaken with the same frequency as the mirror that generates the phase variation. However, as long as the frequency of this vibration is far from the trapping frequency of an atom in the lattice, this is not a serious problem. When the three lasers beams are chosen in the xy-plane with an angle of $2\pi/3$ between them, a hexagonal structure is formed, as shown in Fig. 2.5. Lateron in this chapter the band structure of this configuration is analysed, as well as the band structure of the one-dimensional optical lattice.

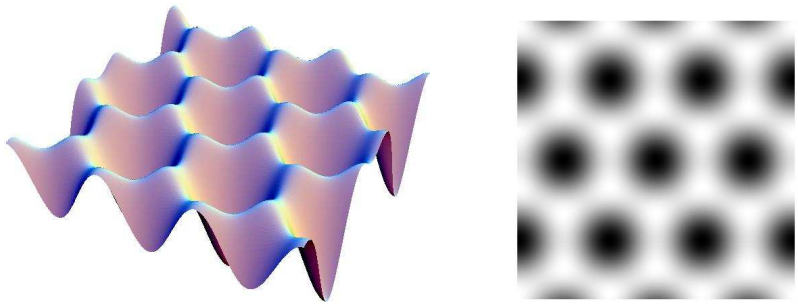

Figure 2.5: Graphical representation of the trapping potential in a two-dimensional optical lattice using three beams, in the xy-plane, with an angle of $2\pi/3$ between them.

2.2.3 Three-dimensional lattices

In the case of a three-dimensional lattice, the situation is similar to the case of two dimensions. If four laser beams are used, the lattice is inherently stable against phase variations, but also three superimposed standing waves with a frequency offset can be used. However, in three dimensions there is an additional complexity. In the discussion of the previous paragraph, the polarization of all the beams was taken equal and orthogonal to all the laser-beam directions. In three dimensions, the laser beams are in all three Cartesian directions, which means it is no longer possible to choose all the polarization vectors in the same direction. Two possible configurations are discussed in Ref. [16]. One of these configurations is presented in Fig. 2.6. We call this the perpendicular-planes configuration, for the obvious reason that there are two pairs of laser beams which span two perpendicular planes. The small arrows indicate the polarization vectors, which in this case point out of the plane spanned by each pair of laser beams. As this configuration is a generalization of the lin$\perp$lin standing wave, it is expected that the σ^+ and σ^- components have their maxima at different positions, as was the case in one dimension. The actual crystallographic structure strongly depends on the angle θ between the laser beams that form a pair. If the angle is such that $\cos\theta = 1/\sqrt{5}$, the lattice exhibits a face-centered-cubic structure as shown in Fig. 2.7(a). However, when the angle is chosen such that $\cos\theta = 1/\sqrt{3}$, the lattice has a body-centered-cubic structure.

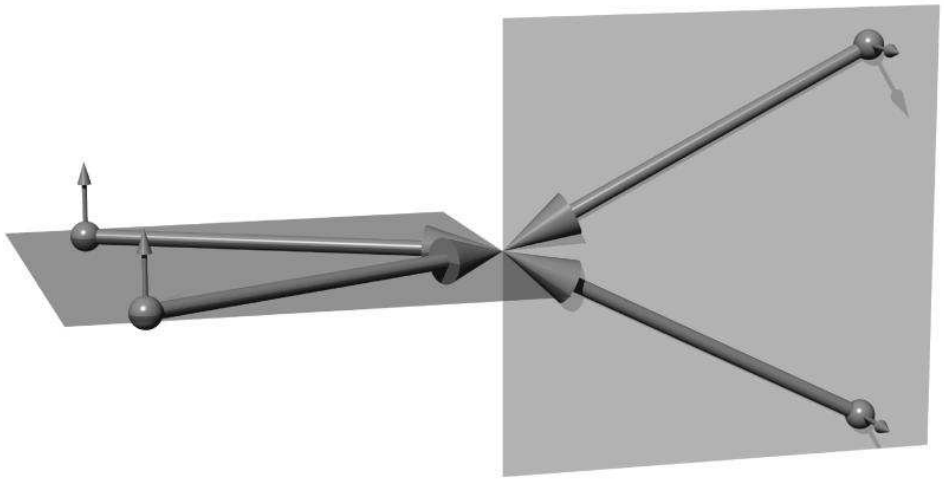

Figure 2.6: Graphical representation of the perpendicular-planes configuration

The other configuration discussed in Ref. [16] is shown in Fig. 2.8. This configuration is known as the umbrella configuration, because it has an umbrella-like appearance.

When three standing waves offset in frequency are used, the lattice shape is stable with respect to the phase of the laser beams, but there remains the problem of how to choose the polarization vectors. When three standing waves with linear polarization are used, the polarization vectors cannot all be chosen in the same direction. In the situation illustrated in Fig. 2.9, two standing waves in the xy-plane are used with their polarization vectors out of the plane and the third standing wave has a linear polarization in the direction of one of the other standing waves. The polarization at every point in the lattice is determined by the interference between all three standing waves. However, as the standing waves have a frequency offset the interference pattern changes very rapidly over time. If the frequency offset is large enough, the atom experiences only the time averaged direction of the polarization, which in the case of Fig. 2.9 makes an angle ϕ with the normal of the plane spanned by the first two standing waves, where $\tan\phi = 1/2$.

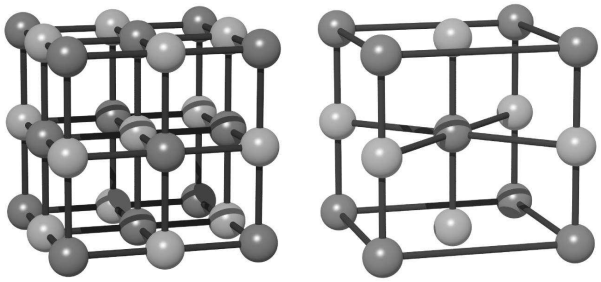

Figure 2.7: Schematic representation of a unit cells of the lattice for an angle of $\cos\theta = 1/\sqrt{5}$ (left) and an angle of $\cos\theta = 1/\sqrt{3}$ (right). The dark and light spheres represent the minima for the two circular polarizations of the light.

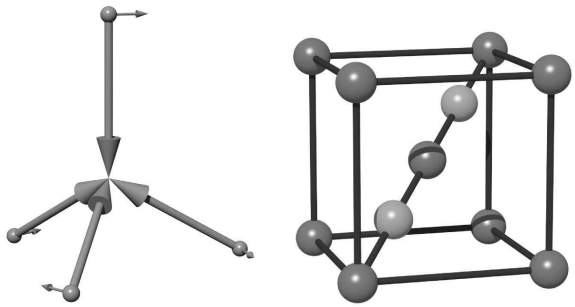

Figure 2.8: Schematic representation of the umbrella configuration (left) and the unit cell associated with this configuration (right).

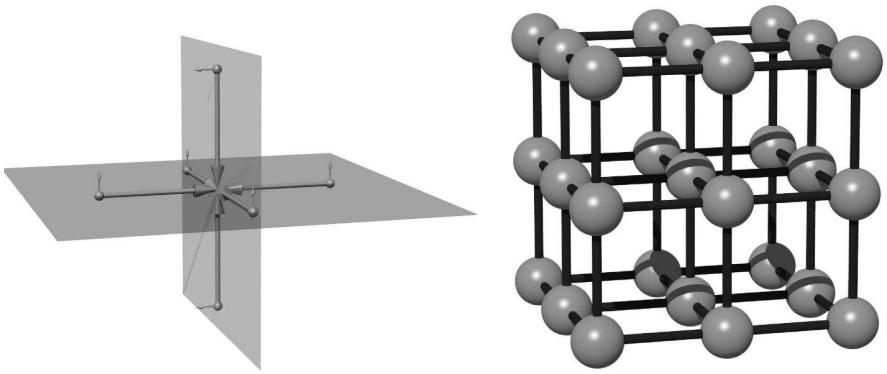

Figure 2.9: Schematic representation of the laser configuration for a three-dimensional optical lattice (left) and the lattice structure associated with this configuration (right).

2.3 Band structure

To understand the physics of an atom in a standing light field, we calculate the band structure for three of the configurations described in the previous sections. We first present the appropriate Hamiltonian and then numerically diagonalize it. We show how the eigenvalues of the Hamiltonian allow us to construct the band structure of the lattice and we discuss its features.

2.3.1 Hamiltonian

When an atom is placed in a standing wave of far-detuned light, the atom can absorb a photon from one beam and be stimulated to emit a photon in the same beam, or in the other beam. This means that momenta of either 0 or $\pm 2\hbar k_{\mathrm{ph}}$ can be transfered, where $\hbar k_{\mathrm{ph}}$ is the momentum of the photon. The zero-momentum transfer corresponds to the homogeneous part of the light shift and the $\pm 2\hbar k_{\mathrm{ph}}$ transfers cause the lattice potential, as will become apparant in the following. If we assume the atom to be in a box, we can write the Hamiltonian of the atom in the light field as a matrix operating on a basis of the momentum states of the atom. In detail

$$H_{\mathbf{k},\mathbf{k}'} = \frac{\hbar^2 \mathbf{k}^2}{2m} \delta_{\mathbf{k},\mathbf{k}'} + \sum_{\mathbf{k}_i} V_{\mathbf{k}_i} \delta_{\mathbf{k}+\mathbf{k}_i,\mathbf{k}'}. \tag{2.6}$$

In the case of a one-dimensional lattice $\{k_i\} = 0, \pm 2k_{\mathrm{ph}}$ as argued above, but for two and three-dimensional lattices more terms have to be taken into account. The zero-momentum term is the homogeneous light shift, given by $V_0 = \hbar\delta s$ and the other terms, which determine the lattice depth, are given by $V_{\pm 2k_{\mathrm{ph}}} = \hbar\delta s/2$. As is conventional in solid-state physics, we can now fold the momentum of the atom into the first Brillouin zone by defining a quasimomentum $\mathbf{q}$, such that $-\pi/a < q_x, q_y, q_z < \pi/a$ and $\mathbf{k} = \mathbf{q} + \mathbf{K}$, where $\mathbf{K}$ is a reciprocal lattice vector. Since the lattice spacing of the standing wave is $a = \lambda/2$, the edge of the first Brillouin zone π/a exactly equals the wavenumber of the lattice light, so $-k_{\mathrm{ph}} < q_x, q_y, q_z < k_{\mathrm{ph}}$. The light therefore only couples momentum states that correspond to the same quasimomentum, which is called the family momentum in the field of laser cooling. Using the fact that the different quasimomenta are uncoupled, we can treat $\mathbf{q}$ as a parameter and write

$$H_{\mathbf{K},\mathbf{K}'} = \frac{\hbar^2(\mathbf{q}+\mathbf{K})^2}{2m}\delta_{\mathbf{q}+\mathbf{K},\mathbf{q}+\mathbf{K}'} + \sum_{\mathbf{k}_i} V_{\mathbf{k}_i}\delta_{\mathbf{q}+\mathbf{K}+\mathbf{k}_i,\mathbf{q}+\mathbf{K}'}. \qquad (2.7)$$

This Hamiltonian can be diagonalized to find the spectrum $\varepsilon_{\mathbf{q}}$ for each $\mathbf{q}$. This procedure is completely analogous to techniques used in solid-state physics, but there is an important difference. In solid-state physics much more couplings have to be taken into account, as the couplings in that case correspond to the spatial Fourier components of the Coulomb potentials due to all the nucleï in the lattice. In the case of optical lattices the number of components is determined only by the number of laser beams n. There are n^2 combinations of absorbtion and stimulated emission, of which n combinations transfer no momentum and thus only cause a light shift. This means that in general, the zero momentum component is equal to $V_0 = n\hbar\delta s/2$. The remaining $n(n-1)$ combinations can be written as $\{\mathbf{k}_i\} = \pm\mathbf{k}_1, ..., \pm\mathbf{k}_{n(n-1)/2}$. However, this is only true in the case of low saturation, because only in that case is the optical potential exactly proportional to the light shift. When the saturation is not low, the probability that an atom is in the excited state has to be taken into account. In the above formalism, this is achieved by adding higher-order Fourier components. Also, spontaneous emission would become non-neglegible. This would have two further implications for the above procedure. First, an imaginary term has to be added to account for the energy loss associated with the spontaneous emission. Second, due to the fact that light is spon-

taneously emitted in all directions, it couples all the quasimomenta, which makes the parameterization in Eq. (2.7) invalid. Physically speaking, both a dissipation and a fluctuation term would have to be added to account for the competing effects of cooling and heating due to spontaneous emission.

2.3.2 Numerical results in one dimension

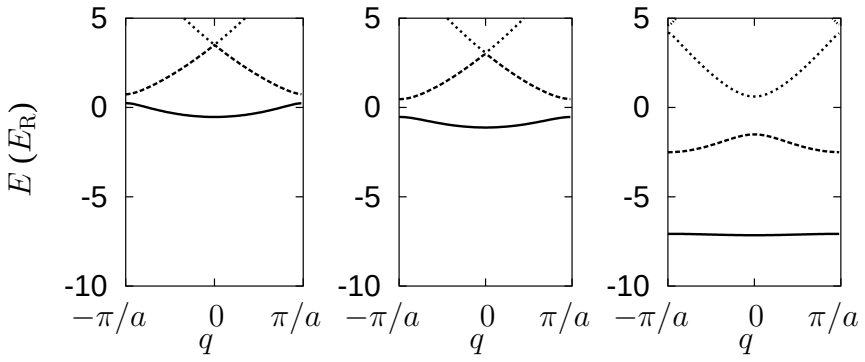

Figure 2.10: The band structure of an atom in an one-dimensional optical lattice for a Rabi frequency of .5, 1 and $5\,E_{\mathrm{R}}/\hbar$, respectively.

As mentioned above, the couplings are rather simple in one dimension. The momenta are $\{k_i\} = 0, \pm 2k_{\mathrm{ph}}$ and the couplings are given by $V_0 = \hbar\delta s$ and $V_{\pm 2k_{\mathrm{ph}}} = \hbar\delta s/2$. We diagonalize the matrix in Eq. (2.7), with Rabi frequencies of .5, 1 and $5\,E_{\mathrm{R}}/\hbar$, with $E_{\mathrm{R}} = \hbar^2 k_{\mathrm{ph}}^2/2m$ the recoil energy. In a numerical calculation a truncation value for the momentum must be chosen such that the calculation converges. In practice convergence is reached when only a few states above the trapping threshold are taken into account. The results of the calculation is shown in Fig. 2.10, where we plot the eigenvalues as a functions of the quasimomentum q. Note that for a Rabi frequency of $.5\,E_{\mathrm{R}}/\hbar$ there is only one band-gap, while for $5\,E_{\mathrm{R}}/\hbar$ there are three. Also note that for $5\,E_{\mathrm{R}}/\hbar$ the lowest band is very flat, which means the atom is very tightly bound to a site.

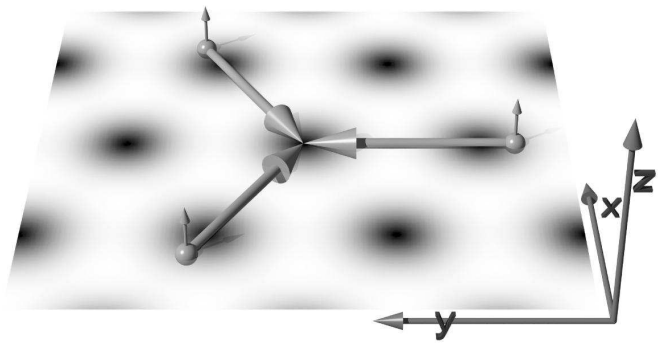

Figure 2.11: Laser-beam configuration for a two-dimensional hexagonal lattice.

2.3.3 Numerical results in two dimensions

As an example of a two-dimensional lattice, we now analyse the band structure of the hexagonal lattice shown in Fig. 2.11. If the wave vectors of the lattice laser beams are chosen as

$$\begin{aligned}\mathbf{k}_1 &= \mathbf{e}_y k_{\mathrm{ph}},\\ \mathbf{k}_2 &= -\mathbf{e}_y k_{\mathrm{ph}}/2 + \mathbf{e}_x k_{\mathrm{ph}}\sqrt{3}/2,\\ \mathbf{k}_3 &= -\mathbf{e}_y k_{\mathrm{ph}}/2 - \mathbf{e}_x k_{\mathrm{ph}}\sqrt{3}/2,\end{aligned} \tag{2.8}$$

then the reciprocal lattice is generated by the vectors $\boldsymbol{\kappa}_1 = \mathbf{e}_x k_{\mathrm{ph}}\sqrt{3}$ and $\boldsymbol{\kappa}_2 = (\sqrt{3}\mathbf{e}_x k_{\mathrm{ph}} - 3\mathbf{e}_y k_{\mathrm{ph}})/2$. These correspond to the principal lattice vectors $\mathbf{a}_1 = (\sqrt{3}\mathbf{e}_x + \mathbf{e}_y)2\pi/3k_{\mathrm{ph}}$ and $\mathbf{a}_2 = \mathbf{e}_y 4\pi/3k_{\mathrm{ph}}$. The lattice spacing is then given by $a = 2\lambda/3$, where λ is the wave length of the lattice lasers. The band structure is visualized in Fig. 2.12, in which the quasimomentum is scanned from $\mathbf{q} = \mathrm{M} \to \Gamma \to \mathrm{K} \to \mathrm{M}$, where $\Gamma = (0,0,0)$, $\mathrm{M} = (\boldsymbol{\kappa}_1 + \boldsymbol{\kappa}_2)/2$ and $\mathrm{K} = \boldsymbol{\kappa}_1$. For each $\mathbf{q}$ in the graph, we have to diagonalize the Hamiltonian on the basis

$$\{\mathbf{k}\} = \{\mathbf{k} \mid \mathbf{q} \pm n\boldsymbol{\kappa}_1 \pm m\boldsymbol{\kappa}_2 \;\forall\; n, m \in \mathbb{N}\}, \tag{2.9}$$

using the couplings $V_0 = 3\hbar\delta s/2$ and $V_{\pm\{\boldsymbol{\kappa}_i\}} = \hbar\delta s/2$, where $\{\boldsymbol{\kappa}_i\} = \boldsymbol{\kappa}_1, \boldsymbol{\kappa}_2$ and $\boldsymbol{\kappa}_1 - \boldsymbol{\kappa}_2$. The band structure in two dimensions looks very complicated compared to the one-dimensional case. However, this is mainly due to the

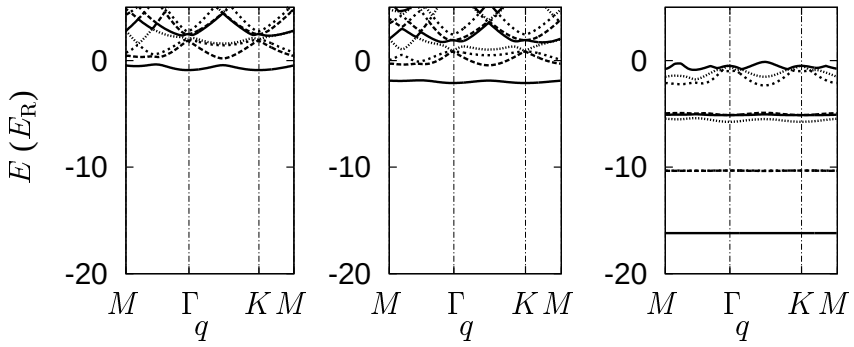

Figure 2.12: Band structure for a two-dimensional hexagonal lattice plotted along the principal directions M → Γ → K → M for Rabi frequencies of .5, 1 and $5\,E_{\mathrm{R}}/\hbar$.

fact that even the band structure of a free atom looks rather complicated when plotted along the same path through the Brillouin zone.

2.3.4 Numerical results in three dimensions

As an example of a three-dimensional lattice, we calculate the band structure of the configuration of three standing waves offset in frequency. Due to the frequency offset the problem is somewhat simplified, because absorption from one standing wave followed by stimulated emission into another standing wave is neglegible in the rotating wave approximation. This reduces the number of couplings from $n(n-1) = 30$ to 12. If the wave vectors of the laser beams are chosen as

$$\begin{aligned} \mathbf{k}_{1,2} &= \pm\mathbf{e}_x k_{\mathrm{ph}}, \\ \mathbf{k}_{3,4} &= \pm\mathbf{e}_y k_{\mathrm{ph}}, \\ \mathbf{k}_{5,6} &= \pm\mathbf{e}_z k_{\mathrm{ph}}, \end{aligned} \tag{2.10}$$

then the reciprocal lattice is generated by the vectors $\boldsymbol{\kappa}_1 = 2\mathbf{e}_x k_{\mathrm{ph}}$, $\boldsymbol{\kappa}_2 = 2\mathbf{e}_y k_{\mathrm{ph}}$ and $\boldsymbol{\kappa}_3 = 2\mathbf{e}_z k_{\mathrm{ph}}$, which means we have to diagonalize the Hamiltonian on the basis

$$\{\mathbf{k}\} = \{\mathbf{k} \mid \mathbf{q} \pm n\boldsymbol{\kappa}_1 \pm m\boldsymbol{\kappa}_2 \ \pm o\boldsymbol{\kappa}_3 \ \forall\ n, m, o \in \mathbb{N}\}, \tag{2.11}$$

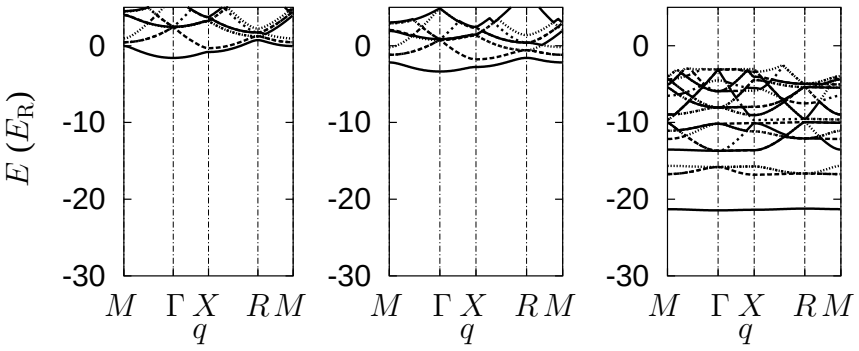

Figure 2.13: Band structure for a three-dimensional simple cubic lattice plotted along the principal directions M → Γ → X → R → M for Rabi frequencies of .5, 1 and 5 $E_{\rm R}/\hbar$.

using the couplings $V_0 = 3\hbar\delta s$ and $V_{\pm\{\boldsymbol{\kappa}_i\}} = \hbar\delta s/2$. In Fig. 2.13 the band structure is plotted along various points of symmetry in the lattice for Rabi frequencies of .5, 1 and 5 $E_{\rm R}/\hbar$. The points of symmetry are labelled $\Gamma = (0,0,0)$, $\mathrm{X} = (\pi/a, 0, 0)$, $\mathrm{R} = (\pi/a, \pi/a, \pi/a)$ and $\mathrm{M} = (\pi/a, \pi/a, 0)$. Note that there is a very interesting feature in Fig. 2.13. In the path X → R → M the energy of the lowest two bands of the free atom are degenerate. As the coupling is increased, this degeneracy is lifted. However, as can be seen in Fig. 2.13, there is band overlap between the lowest band and the band above that, for Rabi frequencies of .5 $E_{\rm R}/\hbar$ and 1 $E_{\rm R}/\hbar$. This could lead to a loss mechanism when loading the lattice, but as soon as the couplings are stronger that 2 or 3 recoil energies, the band overlap is removed.

2.4 The Bose-Hubbard Model

In the previous paragraph, the band structure of a single atom in an optical lattice was calculated for various lattice configurations. However, to describe a gas of bosonic atoms in an optical lattice, the interaction between the atoms has to be taken into account. This is achieved using the so-called Bose-Hubbard model. This model is a variation on the original Hubbard model, which describes electrons in a crystal lattice. To arrive

at the Bose-Hubbard model, we start by writing a general Hamiltonian for a gas of spinless bosons with mass m in an external potential $V^{\text{ext}}(\mathbf{x})$, a chemical potential μ and an interatomic potential $V(\mathbf{x}-\mathbf{x}')$

$$H = \int d\mathbf{x} a^\dagger(\mathbf{x}) \left\{ -\frac{\hbar^2 \nabla^2}{2m} + V^{\text{ext}}(\mathbf{x}) - \mu \right\} a(\mathbf{x}) + \frac{1}{2} \int d\mathbf{x} d\mathbf{x}' a^\dagger(\mathbf{x}) a^\dagger(\mathbf{x}') V(\mathbf{x}-\mathbf{x}') a(\mathbf{x}') a(\mathbf{x}), \tag{2.12}$$

where the field operators $a^\dagger(\mathbf{x})$ and $a(\mathbf{x})$ create and annihilate a particle at position $\mathbf{x}$, respectively. Note, that in contrast to the Hamiltonians in the previous section, Eq. (2.12) is written in second-quantized form, which means it does not operate on a single-particle wave function, but on a many-particle Fock space. In order to simplify the above Hamiltonian, the field operators are expanding in a basis that is diagonal with respect to the external potential. Because the atoms are in a lattice, our choice is to expand the field operators $a^\dagger(\mathbf{x})$ and $a(\mathbf{x})$ in terms of the Wannier states $\chi_n(\mathbf{x})$ of the lattice, which are given by $\chi_n(\mathbf{x}-\mathbf{x}_i) = \sum_{\mathbf{k}} u_{n\mathbf{k}}(\mathbf{x}) \exp(-i\mathbf{k}\cdot \mathbf{x}_i)/\sqrt{V}$, where V is the volume and $u_{n\mathbf{k}}(\mathbf{x})$ are the Bloch wave functions corresponding to the band structures presented in the previous section. The expansions of the field operators $a^\dagger(\mathbf{x})$ and $a(\mathbf{x})$ are given by

$$a^\dagger(\mathbf{x}) = \sum_{n,i} a_{ni}^\dagger \chi_n^*(\mathbf{x}-\mathbf{x}_i),\ a(\mathbf{x}) = \sum_{n,i} a_{ni} \chi_n(\mathbf{x}-\mathbf{x}_i). \tag{2.13}$$

The operators $a_{ni}^\dagger$ and a_{ni} annihilate and create an atom in the n-th trap state of site i, respectively. Next we assume the temperature is sufficiently low and the interaction energy is sufficiently small, such that all the atoms are in the lowest band of the lattice which means only the $n = 0$ terms in Eq. (2.13) have to be taken into account. If Eq. (2.13) is substituted into

Eq. (2.12), with the restriction $n = 0$, the Hamiltonian is given by

$$\begin{aligned} H &= H_0 + H_{\text{int}} \\ &= \sum_{ij} a_i^\dagger a_j \int d\mathbf{x} \chi_0^*(\mathbf{x} - \mathbf{x}_i) \left\{ -\frac{\hbar^2 \nabla^2}{2m} + V^{\text{ext}}(\mathbf{x}) - \mu \right\} \chi_0(\mathbf{x} - \mathbf{x}_j) \\ &+ \frac{1}{2} \sum_{iji'j'} a_i^\dagger a_{i'}^\dagger a_j a_{j'} \\ &\times \int d\mathbf{x} d\mathbf{x}' \chi_0^*(\mathbf{x} - \mathbf{x}_i) \chi_0^*(\mathbf{x}' - \mathbf{x}_{i'}) V(\mathbf{x} - \mathbf{x}') \chi_0(\mathbf{x}' - \mathbf{x}_j) \chi_0(\mathbf{x} - \mathbf{x}_{j'}). \end{aligned} \tag{2.14}$$

Because the wave functions $\chi_0(\mathbf{x})$ are known, the first term on the right-hand side can be written as

$$H_0 = \sum_i a_i^\dagger a_i \{\epsilon_i - \mu\} - \sum_{\langle i,j \rangle} a_i^\dagger a_j t_{ij}, \tag{2.15}$$

where the on-site energy ϵ_i corresponds to the energy of the lowest Wannier state, which is given by

$$\epsilon_i = \int d\mathbf{x} \chi_0^*(\mathbf{x} - \mathbf{x}_i) \left\{ -\frac{\hbar^2 \nabla^2}{2m} + V^{\text{ext}}(\mathbf{x}) \right\} \chi_0(\mathbf{x} - \mathbf{x}_i). \tag{2.16}$$

However, we will only describe homogeneous lattices, so we can safely treat ϵ_i as a shift in the chemical potential. Because the tunneling decays exponentially with distance we can restrict tunneling between sites to only nearest-neighbour tunneling in Eq. (2.15). From Eq. (2.14) we derive that the tunneling amplitude t_{ij} is given by

$$t_{ij} = -\int d\mathbf{x} \chi_0^*(\mathbf{x} - \mathbf{x}_i) \left\{ -\frac{\hbar^2 \nabla^2}{2m} + V^{\text{ext}}(\mathbf{x}) \right\} \chi_0(\mathbf{x} - \mathbf{x}_j), \tag{2.17}$$

which corresponds to the tight-binding approximation.

The second term in Eq. (2.14) can be treated relatively easily if the full interatomic potential is replaced by a delta-function pseudopotential

$$V(\mathbf{x} - \mathbf{x}') = \frac{4\pi a_s \hbar^2}{m} \delta(\mathbf{x} - \mathbf{x}'), \tag{2.18}$$

where a_s is the appropriate scattering length. In most cases, the range of the interaction between the atoms is much smaller than the lattice spacing, so we can restrict ourselves to on-site interactions. For small scattering lengths, the interaction energy can then to a good approximation be written as

$$\begin{aligned} H_{\text{int}} &= \frac{1}{2}\sum_{iji'j'} a_i^\dagger a_{i'}^\dagger a_j a_{j'} \\ &\times \int d\mathbf{x} d\mathbf{x}' \chi_0^*(\mathbf{x}-\mathbf{x}_i)\chi_0^*(\mathbf{x}'-\mathbf{x}_i')V(\mathbf{x}-\mathbf{x}')\chi_0(\mathbf{x}'-\mathbf{x}_j)\chi_0(\mathbf{x}-\mathbf{x}_j') \\ &\cong \frac{1}{2}\sum_i a_i^\dagger a_i^\dagger a_i a_i \frac{4\pi a_s \hbar^2}{m}\int d\mathbf{x}\,|\chi_0(\mathbf{x}-\mathbf{x}_i)|^4 \\ &\equiv \frac{1}{2}U\sum_i a_i^\dagger a_i^\dagger a_i a_i, \end{aligned} \tag{2.19}$$

where we have introduced the symbol U as the on-site interaction energy. From the above equation it can be seen that $U \propto \int d\mathbf{r}\,|\chi_0(\mathbf{x})|^4$, which is easy to understand because the on-site particle density $n(\mathbf{x})$ is given by $n(\mathbf{x}) = |\chi_0(\mathbf{x})|^2$ and the interaction energy is expected to scale with the square of the density. A more rigorous derivation of the interaction energy will be given in the following section, as well as a discussion on the range of scattering lengths for which Eq. (2.19) is valid.

Combining Eqs. (2.19) and (2.17), we arrive at our final form for the single-band Bose-Hubbard Hamiltonian

$$H = -\sum_{\langle i,j\rangle} t_{ij} a_i^\dagger a_j + \frac{1}{2}U\sum_i a_i^\dagger a_i^\dagger a_i a_i - \mu\sum_i a_i^\dagger a_i. \tag{2.20}$$

This Hamiltonian will be used throughout the remainder of this thesis. It will be shown that it contains interesting features that are experimentally accesible, because of the tunability of the parameters U and t.

2.5 Interaction energy

To better understand the interaction energy and to investigate the validity of Eq. (2.19), we perform an exact calculation of the energy of two atoms in an harmonic potential with a delta-function interaction. A similar calculation was carried out by Busch *et al.* [17]. However, these authors

did not use a true delta-function potential, but the so-called regularized delta-function pseudopotential [18]. Using a true delta function yields an expression, which has an ultra-violet (UV) divergence. Here we will show that this UV divergence can be dealt with using standard renormalization techniques.

We start by writing the Hamiltonian of two atoms in a harmonic trap as

$$H = -\frac{\hbar^2\nabla_1^2}{2m} - \frac{\hbar^2\nabla_2^2}{2m} + \frac{1}{2}kr_1^2 + \frac{1}{2}kr_2^2 + V_0\delta(\mathbf{r}_1 - \mathbf{r}_2), \tag{2.21}$$

where m is the mass of the atoms, k is the spring constant of the trap and V_0 is the strength of the delta potential. Introducing a center-of-mass coordinate $\mathbf{R} = (\mathbf{r}_1 + \mathbf{r}_2)/2$ and a relative coordinate $\mathbf{r} = \mathbf{r}_1 - \mathbf{r}_2$ we can write

$$\begin{aligned} H &= -\frac{\hbar^2\nabla_R^2}{2M} - \frac{\hbar^2\nabla_r^2}{2\mu} + kR^2 + \frac{1}{4}kr^2 + V_0\delta(\mathbf{r}) \\ &= H_{\mathrm{CM}} + H_{\mathrm{rel}}, \end{aligned} \tag{2.22}$$

where $M = 2m$ is the total mass, $\mu = m/2$ is the reduced mass and H_{CM} and H_{rel} denote the center-of-mass part and the relative part of the Hamiltonian, respectively. The relative part is relevant here, since only this part contains the interaction between the atoms. We can write $H_{\mathrm{rel}} = H_0 + V$, where

$$H_0 = -\frac{\hbar^2\nabla_r^2}{2\mu} + \frac{1}{2}\kappa r^2, \tag{2.23a}$$

$$V = V_0\delta(\mathbf{r}), \tag{2.23b}$$

and $\kappa = k/2$. The above equations are simplified by writing the Hamiltonian in units of the energy $\hbar\omega = \hbar\sqrt{\kappa/\mu}$ and the length scales in units of the harmonic oscillation length $l = (\hbar^2/\mu\kappa)^{1/4}$. The resulting dimensionless quantities are denoted by a prime, so $H_0' = -\nabla'^2/2 + r'^2/2$ and $V' = V_0'\delta(\mathbf{r}')$ with $V_0' = V_0/l^3\hbar\omega$. The scaling of the interaction strength by $1/l^3$ is necessary because $\delta(\mathbf{r})$ has the unit of $(\text{volume})^{-1}$ and $\delta(\mathbf{r}')$ does not. Only states with an angular momentum $\ell = 0$ have a nonzero value at an interatomic distance $r' = 0$. The $\ell = 0$ eigenstates and eigenvalues of

the noninteracting Hamiltonian H_0' are given by

$$\phi_n(\mathbf{r}') = \pi^{-3/4}\left[L_n^{1/2}(0)\right]^{-1/2} e^{-r'^2/2} L_n^{1/2}(r'^2), \tag{2.24a}$$

$$E_n = 2n + 3/2, \tag{2.24b}$$

where $L_n^{1/2}$ are the generalized Laguerre polynomials. Because the wave functions $\phi_n(\mathbf{r}')$ form a complete set, the solutions of the relative Hamiltonian can be written as $\psi(\mathbf{r}') = \sum_m c_m \phi_m(\mathbf{r}')$. With this expansion, the Schrödinger equation $(H_0' + V')\psi(\mathbf{r}') = E\psi(\mathbf{r}')$ reads

$$\sum_m c_m \left(E_m - E\right)\phi_m(\mathbf{r}') + V_0'\delta(\mathbf{r}')\sum_m c_m\phi_m(\mathbf{r}') = 0. \tag{2.25}$$

This equation can be simplified by multiplying by $\phi_n^*(\mathbf{r}')$ and integrating over $\mathbf{r}'$. The first term on the left-hand side then reduces to $c_n(E_n - E)$ and the second term becomes $V_0'\phi_n(\mathbf{0})\sum_m c_m\phi_m(\mathbf{0})$. However, the latter term can be shown to be divergent. To determine the exact form of the divergence, the limit $\mathbf{r}' \to 0$ is taken after the summation. We thus arrive at the following expression for the Schrödinger equation

$$\begin{aligned} 0 &= c_n\left(E_n - E\right) + V_0'\phi_n^*(\mathbf{0})\left[\sum_m c_m\phi_m(\mathbf{r}')\right]_{r'\to 0} \\ &= \phi_n^*(\mathbf{0}) + V_0'\phi_n^0(\mathbf{0})\left[\sum_m \frac{\phi_m^*(\mathbf{0})\phi_m(\mathbf{r}')}{E_m - E}\right]_{r'\to 0}, \end{aligned} \tag{2.26}$$

where we have used $c_n \propto \phi_n^*(\mathbf{0})/(E_n - E)$, with a proportionality constant that is fixed by the normalization of the wave function. Substituting the wave functions from Eq. (2.24a) into the above equation yields

$$-\frac{1}{V_0'} = \left[\sum_m \frac{\phi_m^*(\mathbf{0})\phi_m(\mathbf{r}')}{E_m - E}\right]_{r'\to 0} = \frac{1}{2\pi^{3/2}}\left[\sum_m \frac{L_m^{1/2}(\mathbf{r}'^2)}{m - \nu}\right]_{r'\to 0}, \tag{2.27}$$

where we have written $E = 2\nu + 3/2$. Note that ν is in general not an integer and can be both positive and negative. Following Busch *et al.* we find

$$\sum_m \frac{L_m^{1/2}(\mathbf{r}'^2)}{m - \nu} = \Gamma(-\nu)U(-\nu, 3/2, r'^2), \tag{2.28}$$

with $U(-\nu, 3/2, r'^2)$ a confluent hypergeometric function and $\Gamma(-\nu)$ is the complete gamma function [19]. For small $\mathbf{r}'$ this reduces to

$$\sum_m \frac{L_m^{1/2}(\mathbf{r}'^2)}{m-\nu} = -\sqrt{\pi}\left(\frac{2\Gamma(-\nu)}{\Gamma(-\nu-1/2)} - \frac{1}{r'} + \mathcal{O}(r')\right). \tag{2.29}$$

Using this result, Eq. (2.27) can be written as

$$\frac{1}{V_0'} = \frac{1}{\pi}\frac{\Gamma(-E/2\hbar\omega+3/4)}{\Gamma(-E/2\hbar\omega+1/4)} - \lim_{r'\to 0}\frac{1}{2\pi r'}. \tag{2.30}$$

By dividing both sides by $l^3\hbar\omega$ the above equation is restored to SI units, yielding

$$\begin{aligned}\frac{1}{V_0} &= \frac{1}{\pi l^3\hbar\omega}\frac{\Gamma(-E/2\hbar\omega+3/4)}{\Gamma(-E/2\hbar\omega+1/4)} - \lim_{r\to 0}\frac{1}{2\pi\hbar\omega l^2 r} \\ &= \frac{1}{\pi l^3\hbar\omega}\frac{\Gamma(-E/2\hbar\omega+3/4)}{\Gamma(-E/2\hbar\omega+1/4)} - \lim_{r\to 0}\frac{m}{4\pi\hbar^2 r},\end{aligned} \tag{2.31}$$

where we have used that the atomic mass $m = 2\mu$. This expression is indeed divergent, but this can easily be dealt with by rewriting the interaction strength V_0 in terms of the two-body transition matrix $T^{2\mathrm{B}}$, as is standard in scattering theory. This is achieved by writing the Lippman-Schwinger equation as

$$\frac{1}{T^{2\mathrm{B}}} = \frac{1}{V_0} + \int \frac{d\mathbf{k}}{(2\pi)^3}\frac{1}{2\epsilon_{\mathbf{k}}}, \tag{2.32}$$

where the dispersion $\epsilon_{\mathbf{k}}$ is given by $\epsilon_{\mathbf{k}} = \hbar^2k^2/2m$. It is immediately obvious that the above integral diverges in the case of three dimensions. To see how it diverges, we multiply the integrant by $\exp(i\mathbf{k}\cdot\mathbf{r})$ and take the limit $r \to 0$. The integral then becomes the Fourier transform of a Coulomb potential and we find

$$\frac{1}{T^{2\mathrm{B}}} = \frac{1}{V_0} + \lim_{r\to 0}\frac{m}{4\pi\hbar^2 r}, \tag{2.33}$$

which exhibits exactly the same divergence as the left-hand side of Eq. (2.31), which means we can write

$$\frac{1}{T^{2\mathrm{B}}} = \frac{1}{\pi l^3\hbar\omega}\frac{\Gamma(-E/2\hbar\omega+3/4)}{\Gamma(-E/2\hbar\omega+1/4)} \Longrightarrow \frac{l}{a_s} = \frac{2\Gamma(-E/2\hbar\omega+3/4)}{\Gamma(-E/2\hbar\omega+1/4)}, \tag{2.34}$$

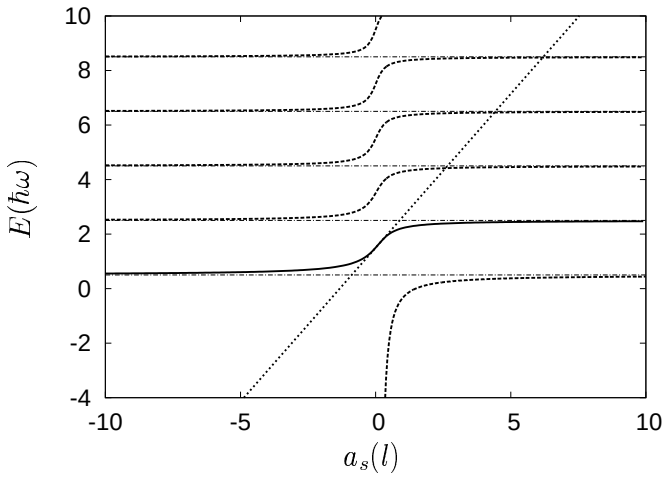

Figure 2.14: The energy levels (in units of $\hbar\omega$) of two particles in an harmonic trap in an $l = 0$ state as a function of the s-wave scattering length a_s (in units of the harmonic oscillator length l). The solid and dashed lines give the energy levels, the dash-dotted lines indicate the asymptotic solutions and the dotted line corresponds to the result using Eq. (2.19).

where we have used the well-known result $T^{2\mathrm{B}} = 4\pi\hbar^2 a_s/m$ in the last step. Note that although the solutions of the relative Hamiltonian are written as an expansion in terms of the solutions of the noninteracting Hamiltonian, the above result is exact because the summation in Eq. (2.28) is performed exactly.

To find the energy E as a function of the scattering length a_s we have to numerically solve Eq. (2.34). The result of this computation is shown in Fig. 2.14. The real ground state of the system is the state that goes to $E = 3\hbar\omega/2$ when $a = 0$. This state is indicated by the solid curve in Fig. 2.14. The shift of the ground-state energy with respect to the value $3\hbar\omega/2$ gives the interaction strength U in the Bose-Hubbard model. As a reference we have added the dotted line, which is calculated using the approximation in Eq. (2.19). The curves coincide as long as $|a_s| \lesssim l/10$. When the value of the scattering length becomes larger than this length scale, the energy shift saturates to $\pm\hbar\omega$ depending on the sign of the scattering length.

The wave functions corresponding to the energies in Fig. 2.14 can be

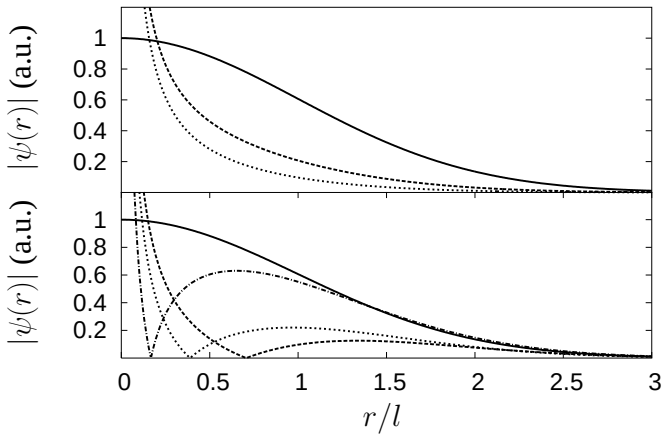

Figure 2.15: The ground-state wave function for two atom in an harmonic oscillator. The upper figure shows the wave function at energies E of $E/\hbar\omega = .5$ (dotted line), 1.0 (dashed line) and 1.5 (solid line). The lower figure shows the wave functions at energies $E/\hbar\omega = 1.5$ (solid line), 1.7 (dash-dotted line), 2.0 (dotted line) and 2.5 (dashed line).

written as

$$\psi(\mathbf{r}') \propto \frac{1}{2\pi^{3/2}} e^{-r'^2/2} \Gamma(-\nu) U(-\nu, 3/2, r'^2), \tag{2.35}$$

where $\nu = E/2\hbar\omega - 3/4$ and E is a solution of Eq. (2.34) as plotted in Fig. 2.14. The ground-state wave function is plotted in Fig. 2.15 for different values of the energy E. In the upper figure, the wave functions are plotted for energies $E < 3\hbar\omega/2$, corresponding to a negative scattering length. In the lower figure, the wave functions are plotted for energies $E > 3\hbar\omega/2$, corresponding to a positive scattering length. Note that due to the change in sign of the scattering length, the wave functions in the lower figure have one more node as compared to the upper figure. Note also that when the scattering length $a_s \neq 0$, the wave functions diverge as $1/r$ for $r \to 0$. In Fig. 2.16 the first excited-state wave functions are plotted. Again, the upper figure corresponds to negative scattering lengths and the lower figure corresponds to positive scattering lengths. Note that the dotted line in the upper figure of Fig. 2.16 corresponds to the dashed curve in the lower figure of Fig. 2.15.

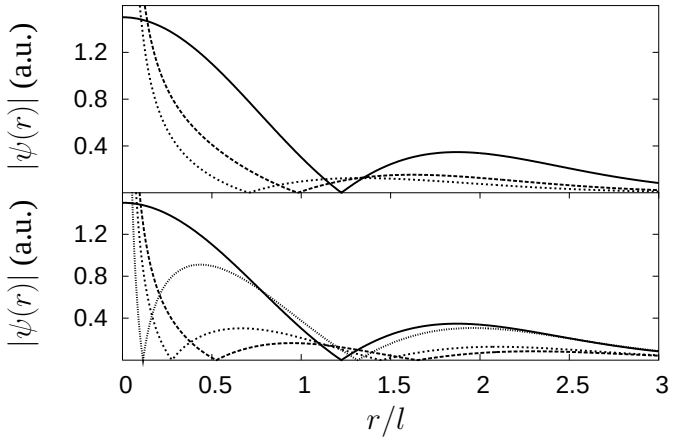

Figure 2.16: The first excited-state wave function for two atom in an harmonic oscillator. The upper figure shows the wave function at energies E of $E/\hbar\omega = 2.5$ (dotted line), 3.0 (dashed line) and 3.5 (solid line). The lower figure shows the wave functions at energies $E\hbar\omega = 3.5$ (solid line), 3.7 (dash-dotted line), 4 (dotted line) and 4.5 (dashed line).

The lowest state on the right-hand side of Fig 2.14 is suspicious. Because this state is not present for a negative scattering length, it appears that the system acquires an extra state for positive scattering length. However, this is unphysical, as the wave functions in Eq. (2.24a) form a complete set. This argument can be understood better by considering perturbation theory. In perturbation theory the corrections should always go to zero when the perturbation is taken to zero. This is illustrated by the dotted line in Fig 2.14, which is the result of perturbation theory. The energy of the lowest state on the right-hand side of Fig 2.14 goes to minus infinity as the perturbation is taken to zero. This behaviour cannot be understood in perturbation theory, so we have to take a more careful look at the state associated with this curve, which we will denote with $\psi_\infty(\mathbf{r})$. By taking the limit $E \to -\infty$ in Eq. (2.34), it can be shown that the energy E_∞ of this state is given by $E_\infty = -\hbar^2/ma^2$ in the limit $a \downarrow 0$. For small values of r, the Schrödinger equation for this state in the limit $a \downarrow 0$ is thus given

$$\left(-\frac{1}{2}\nabla'^2 + V_0'\delta(\mathbf{r}')\right)\psi_\infty(\mathbf{r}') = -\frac{l^2}{2a^2}\psi_\infty(\mathbf{r}'). \tag{2.36}$$

For $r' > 0$ this equation has the form of a Poisson equation with screening, which means that the solution has the form of a Yukawa potential, i.e., $\psi_\infty(\mathbf{r}') = l \exp(-lr'/a)/2a\sqrt{\pi}r'$. However, for $r' \to 0$ this leads to a problem, since in this limit the kinetic energy term becomes $-\nabla'^2\psi_\infty(\mathbf{r}')/2 = \sqrt{\pi}l\delta(\mathbf{r}')/a$. As a result, this delta function is not cancelled by the interaction $V_0'\delta(\mathbf{r}')$, which means that this state is indeed not a solution to the total Schrödinger equation. This is an important difference with the results of Busch *et al.*, who find that in their case, the state is a true bound state in the regularized delta-function potential.

2.6 Quantum phases

To understand the properties of the Bose-Hubbard Hamiltonian, let us first examine the limiting case of $U \to 0$. In this limit the atoms are ideal bosons, so all the atoms will Bose condense in the single-particle ground state, which in this case is the $\mathbf{k} = \mathbf{0}$ state of the lowest Bloch band of the lattice. This means that the atoms are essentialy delocalized in the lattice. This situation is illustrated on the left in Fig. 2.17. When the parameter U is slightly increased, the interaction energy can be treated in perturbation theory. As is shown in Chapter 4, this leads to a quantum depletion of the condensate. In other words, if the interaction energy becomes large, it becomes energetically favourable for the system to move part of the atoms out of the single-particle ground state into states with nonzero quasimomentum, even though the temperature is still zero. In the limiting case that the

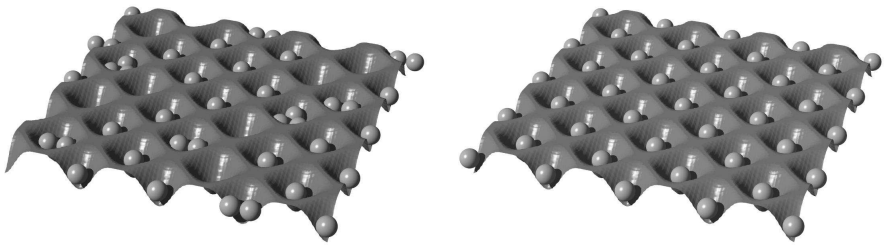

Figure 2.17: Schematic representation of the superfluid (left) and insulating (right) state in an optical lattice.

interaction $U \to \infty$, or equivalently $t \to 0$, the configuration illustrated by

the figure on the left is clearly energetically unfavourable, as there multiply occupied sites occur. It would be more favourable to distribute the atoms homogeneously with one atom at each site, as illustrated on the right in Fig. 2.17. This state is an insulator, because moving an atom from one site to the next results in a double occupation, which is energetically expensive. However, this insulator only exists when there is exactly an integer number of atoms on every site. If we add one atom to the system, this atom can be placed anywhere in the lattice, since the energy penalty on every site is equal. Fig. 2.18 shows a graphical respresentation of the momentum-space

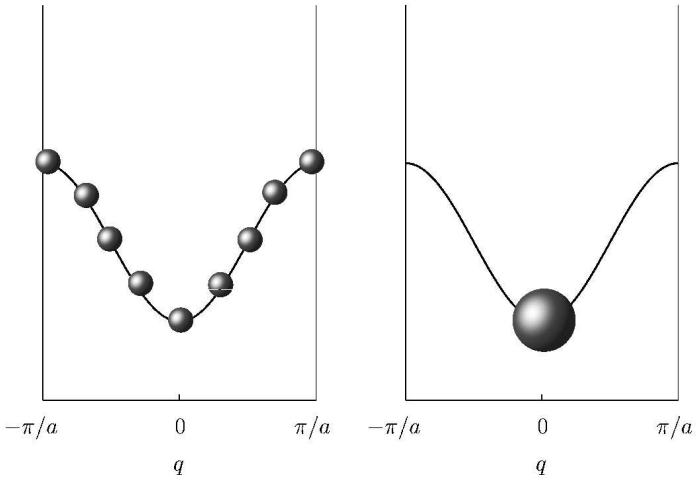

Figure 2.18: Graphical respresentation of the momentum-space distribution of the superfluid (left) and insulating (right) state in an optical lattice.

distribution of the superfluid and insulating states in an optical lattice. In the superfluid state the atoms are all Bose condensed at the minimum of the lowest Bloch band, in the center of the first Brillouin zone. Because all the atoms have quasimomentum $\mathbf{q} = 0$ the complex phase at each site is the same. Due to Heisenberg's uncertainty relation, this implies that the spatial particle-number distribution must be disordered. Conversely, in the insulating state this particle-number distribution is ordered, which means the complex phase has to be disordered. As a result of this, the atoms must all occupy a different momentum state, as represented in Fig. 2.18. This

qualitative argument shows that the system can be in two qualitatively different states. The most interesting question is *how* the system goes from one states to the other, if the parameters U and t are varied. If the system only reaches the insulating states asymptotically for $U \to \infty$, the change is called a crossover. However, if the change happens abruptly for a finite value of U, the change is called a quantum phase transition. This question is experimentally relevant, because by increasing the intensity of the laser beams, the on-site wave function gets narrower. This means that the interaction energy U goes up and the tunneling t goes down. In this way, the ratio of U/t can be tuned experimentally over a large range. In Chapter 4 it will be shown that the system indeed undergoes a quantum phase transition. This phase transition has been observed recently by Greiner *et al.* [15].

Chapter 3

The experimental setup

Abstract

We describe the experimental setup for obtaining Bose-Einstein condensation in an optical lattice. The technique of near-resonant absorption imaging is explained and used to analyse the density of atoms in the magneto-optical trap and the magnetic trap. Furthermore, a discussion about the sequencing system for the experiment is presented.

3.1 Introduction

The density required to obtain a filling fraction of unity in a three-dimensional lattice is large compared to the density of a magneto-optical trap (MOT). In a simple cubic optical lattice created by three standing waves, the density of lattice sites is equal to $(\lambda/2)^{-3}$, which in the case of the visual and near-infrared wave lengths appropriate for alkali atoms is of the order of $10^{14}\,\mathrm{cm}^{-3}$. Since the typical density reached in a MOT is on the order of $10^9 - 10^{11}\,\mathrm{cm}^{-3}$, it is clear that loading a three-dimensional optical lattice directly from a MOT does not yield a sufficiently high filling fraction. If the atoms are compressed by three orders of magnitude, the temperature rises by two orders of magnitude, since there is no way of extracting heat from the atoms at these high densities. This increase in temperature invalidates the assumptions made in the previous chapter in the derivation of the single-band Bose-Hubbard model. A more realistic approach for reaching the required conditions is to load the optical lattice from a Bose-Einstein

condensate [7, 15]. In that case the atoms from the MOT are only slightly compressed when they are transfered to the magnetic trap and the largest increase in density and decrease in temperature is subsequently reached during evaporative cooling. Therefore a setup is being developed to reach Bose-Einstein condensation of sodium in a magnetic trap.

In order to reach Bose-Einstein condensation, the magnetic trap has to be loaded with a large number of atoms ($> 10^9$) at a reasonably low temperature ($< 500\,\mu$K). If these conditions are not met, runaway evaporation is not reached. Because the magnetic trap is conservative, it cannot be loaded continously. This means that the atoms have to be collected in a MOT and then transfered to the magnetic trap. To control the experiment with the required timing accuracy, a sequencing system has been developed. This system is discussed in detail in Sec. 3.6.

To determine the temperature and density of the atoms trapped with the different techniques used in the experiment, a setup for absorption imaging was constructed. The theory of absorption imaging, the imaging setup and some result obtained using this imaging techniques are presented in Secs. 3.2 to 3.5.

First, the laser cooling and trapping stages of the experiment are introduced, but details are only given insofar as they are necessary to understand the results of the imaging experiments. All the details of the implementation and testing of the laser cooling and trapping stages will be thoroughly described in a PhD thesis that is currently under preparation [12].

3.1.1 A source of cold atoms

To achieve the necessary loading rates, a slowed and focussed beam of sodium atoms is used. Here the slowing and focussing stages are briefly sketched.

Oven

The beam of sodium atoms is created in an oven, which consists of two chambers, an aperture and a cooling screen. The first chamber is used to create a vapor from solid sodium. In order to shape the velocity distribution of the beam, the vapor is heated to a slightly higher temperature in the second chamber. This produces a well-defined thermal beam. The diameter of the nozzle of this chamber is 3 mm. The next stage is an aperture, which

is kept at an even higher temperature to prevent deposition of sodium, which could block the aperture. The diameter of this aperture is 3.5 mm. The whole oven is encased in a cooled screen, which has an aperture of 5 mm. When the beam exits the oven, it has an average velocity of about 900 m/s. Since this velocity is much to high to be trapped in a MOT, the atoms are first slowed in the Zeeman slower.

Zeeman slower

The Zeeman slower has been developed by Molenaar [20]. It features separate windings for the bias field and the profile field. The separately controllable bias field makes it possible to operate the Zeeman slower in a wide range of laser detunings. However, due to the fact that the field tends to zero rather slowly at the end of the Zeeman slower, the decoupling of atoms from the light is rather problematic compared to slowers that have a zero crossing in the middle of the solenoid. This means that the atoms still scatter photons from the slowing laser after they have left the slower, which causes significant heating. To reduce this effect a set of extraction coils is used. These coils are configured in such a way that the magnetic field is lifted to a higher value at the end of the slower and then peaks sharply, after which it drops to a negative value, as illustrated in Fig. 3.1. The cooling of the extraction coils is sufficient to run the coils continuously at 20 A, but as they are only needed during loading of the MOT, they can also be pulsed for a few seconds at 40 A.

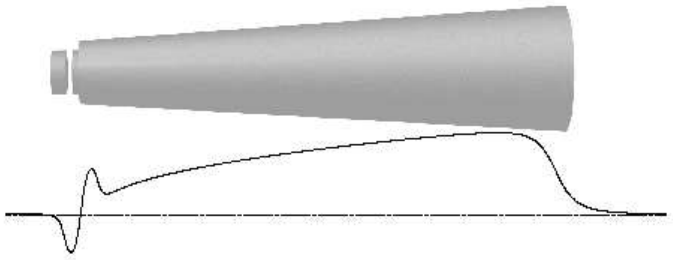

Figure 3.1: The magnetic field inside the Zeeman slower for typical settings of the currents, together with a graphical representation of the solenoid and the extraction coils.

Magneto-optical lens

Because the Zeeman slower only cools in the longitudinal direction, the atomic beam becomes very divergent as it is slowed down. To increase the flux of atoms going into the capture volume of the MOT, the beam is focussed with a magneto-optical lens. In this device, a quadrupole field is generated using a pair of anti-Helmholtz coils. In combination with laser beams from four directions perpendicular to the atomic beam, the atoms are cooled in the transverse directions, but are also focussed in a point a few centimeters behind the MOT.

3.1.2 Atom traps

In the following, a brief introduction is given to the techniques used to trap the beam of atoms. All these techniques are analysed using the imaging setup discussed lateron in this chapter.

Bright MOT

In the bright MOT, a pair of anti-Helmholtz coils is used to produce a quadrupole field in three dimensions. The gradient of the field in the center is 10 G/cm in the plane between the coils and 20 G/cm in the direction perpendicular to that plane. The trapping lasers have a detuning of -30 MHz with respect to the $F = 2 \rightarrow F' = 3$ transition, a saturation parameter of $s_0 = 3$ and a diameter of 25 mm, which is the maximum diameter allowed by the geometry of the vacuum chamber. The cooling transition is not a closed transition, because atoms can also be excited to the $F' = 2$ state, which can subsequently decay into the $F = 1$ state. Due to the fact that this state is 1772 MHz shifted with respect to the other hyperfine ground state, these atoms are effectively lost from the cooling cycle. To circumvent this, a repumping beam is spatially overlapped with the trapping beams in the direction in the plane of the coils with a saturation of a few percent and a detuning of -50 MHz with respect to the $F = 1 \rightarrow F' = 2$ transition. This light pumps the atoms back into the cooling cycle.

The problem with a bright MOT is that as the density becomes higher, the cloud of atoms becomes opaque. This limits the amount of cooling light that enters the center of the trapping region and thus impedes the cooling proces. Furthermore, the spontaneously emitted photons have a high probability of being re-absorbed by the atoms, which causes extra

heating. For this reason, the dark MOT has been invented by Ketterle *et al.* [21].

Dark MOT

In the dark MOT a dark spot of a few millimeters in diameter is placed in the center of the repumping beams, which causes a dark volume in the center of the trap. Around this dark region is a shell of repumping light, which enables efficient capture of atoms. However, as soon as the atoms are forced into the dark region by the trapping light, the atoms are no longer repumped and they decay into the $F = 1$ hyperfine state. This means that the dark region becomes transparent for the trapping light, which can thus pass unimpeded through the high-density cloud without any shadows being cast that could interfere with the capture proces. Furthermore, as the atoms are transparent for the trapping light, they also do not absorb the photons that are spontaneously emitted by the atoms that are being captured. This yields a higher density of atoms trapped in the dark MOT than the density that can be achieved using a bright MOT.

3.1.3 Magnetic trapping

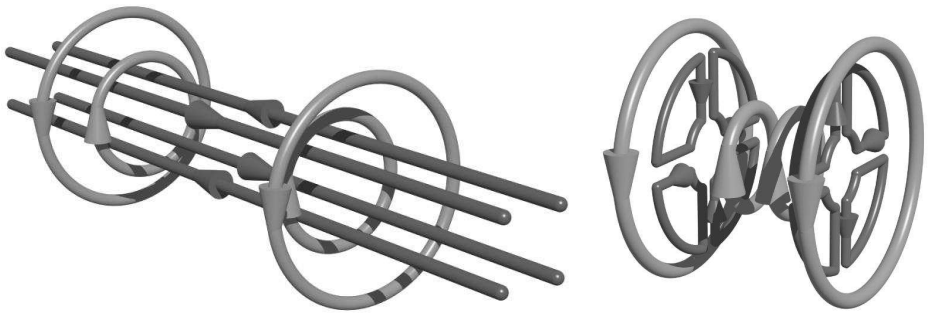

Figure 3.2: The Ioffe-Pritchard (left) and cloverleaf (right) configurations.

Optical-cooling techniques have so far failed to enable high enough phase-space density to achieve Bose-Einstein condensation. This is not just because the temperature is not low enough, but primarily because at high densities laser-cooling techniques break down. For this reason Bose-Einstein

condensates are with a few notable exceptions [22, 23] produced in magnetic traps, using evaporative cooling. Because evaporative cooling takes a long time ($>$ 30 seconds) two requirements have to be met. The vacuum has to be extremely good (10^{-11}mbar) in order to suppress losses due to collisions with background particles. Also, the magnitude of the magnetic field cannot be zero anywhere in the trap. The reason for this last requirement is that when the magnetic field is zero, the spin state of the atom has a high probability of changing to a non-trapped state. Also, these so-called Majorana losses become more probable when the velocity of the atom becomes lower. To create a magnetic field that is nonzero everywhere in the trap, a Ioffe-Pritchard trap is used, in our case in the so-called cloverleaf configuration. These traps consist of four current carrying rods that produce a quadrupole field in the plane perpedicular to the rods. The two coils that form the end-caps of the trap are run with the current in the same direction, but they are placed too close together to form a Helmholtz configuration. This produces a large curvature of the field, which results in the axial trapping. Beside these coils there is also a set of Helmholtz coils placed coaxially with the end-caps, which enable tuning of the bias field in the center of the trap. If the bias field is chosen too large, the trap becomes weaker in the radial trapping direction. However, the bias field has to be chosen large enough to prevent Majorana losses. The Ioffe-Pritchard configuration is illustrated on the left in Fig. 3.2. In the cloverleaf configuration, the four rods are cut in half and folded open into the plane of the end-caps. The wires are closed resulting in a cloverleaf-like configuration as illustrated on the right in Fig. 3.2.

3.2 Imaging system

Since atoms trapped in a magnetic trap do not fluoresce, the atoms have to be analysed using near-resonant absorption imaging. In fact, already in a MOT fluorescence induced by the trapping laser beams is not a good measure of the number of particles. As the density of atoms increases, the cloud becomes opaque and the atoms in the center of the cloud are not subjected to the same intensities as the atoms at the edge of the cloud. For this reason, the atoms in the MOT should also be measured using absorption imaging.

3.2.1 Imaging techniques

Generally speaking imaging techniques can be divided into three classes. The first class is the imaging of light sources, such as stars and fluoresence of tracer molecules in biology. Fluoresence of atoms in a MOT is also in this class of imaging techniques. The second class is absorption imaging, which is the standard way of imaging cell structures in biology and also a convenient way of imaging atoms in situations where fluoresence imaging is not applicable. The third and most complex class are phase-contrast imaging techniques. These techniques make use of the spatial variations in the refractive index that are caused by the sample. The simplest example of refractive imaging is the Schlieren method [24], which is often used to image shockwaves in wind-tunnel experiments because it is so robust that it even works with incoherent light sources such as stroboscopes and even light from the sun.

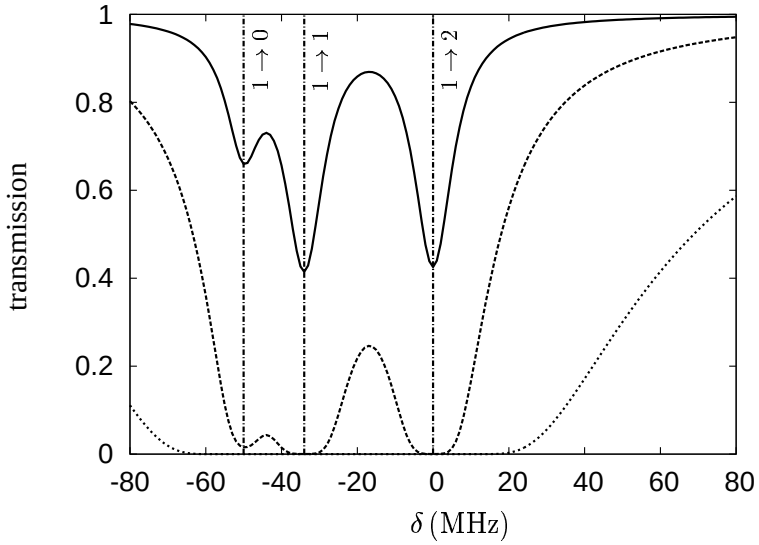

Figure 3.3: The transmission of light through the cloud of atoms as a functions of detuning with respect to the $F = 1 \rightarrow F' = 2$ transition. The three traces corresponds to average optical densities of 1 (solid line), 10 (dashed line) and 100 (dotted line).

To analyse phase and absorption imaging, both the real and the imaginary part of the refractive index n_{r} have to be considered. For a two-level

system, we write

$$n_{\mathrm{r}} = 1 + \frac{\sigma_0 n_{\mathrm{c}} \lambda}{4\pi} \left[\frac{i}{1+\delta^2} - \frac{\delta}{1+\delta^2} \right], \tag{3.1}$$

where σ_0 is the resonant scattering cross section, λ is the wave length of the light and n_{c} is the column density of the sample. The column density is defined as the density of the sample, integrated over the path of a light beam through the sample. The detuning δ is given in units of $\Gamma/2$, where Γ is the natural linewidth. For a two-level system, the cross-section is given by $\sigma_0 = 3\lambda^2/2\pi$ [25]. For a multi-level system an average has to be taken to calculate σ_0 and the expression between square brackets in the above equation has to be replaced by a sum over all the appropriate transitions. For the electric field component of the light, we can now write

$$E = E_0 e^{i(n_{\mathrm{r}}-1)/2}. \tag{3.2}$$

If the detuning δ is small the phase shift can be neglected and the above equation reduces to the Lambert-Beer equation.

In the case where a sodium atom is in the $F = 1$ hyperfine ground state, there are three transitions that have to be considered, namely to the $F' = 0$, 1 and 2 states. The resonant cross section σ_0 and the part between brackets in Eq. (3.1) is then modified to take into account the three transitions and their relative strengths. The result of this calculations is shown in Fig. 3.3. In this figure we see that if the probe laser is tuned to the $F = 1 \rightarrow F' = 0$ transition, the transmission is about 66% if the optical density is 1, and about 2% if the optical density is 10. This means that this frequency is suitable for the lower optical densities one obtains in time-of-flight images. If the atoms are measured *in-situ*, higher optical densities can be expected. In that case a larger detuning has to be chosen, because otherwise almost all the light is absorbed in the center of the image. However, if a larger detuning is chosen, the real part of the refractive index also has to be taken into account. To estimate the imaging error due to diffraction we describe the MOT as a homogeneous phase plate, with a phase step ϕ and a diameter d. In a first-order approximation such a phase plate causes a diffraction angle of $2\lambda\phi/\pi d$. This means that if the phase shift ϕ is large or the diameter d is small, the diffraction angle will be large. In that case higher diffraction orders can miss the aperture of the imaging system, which

will degrade the resolution of the image. In practice, this is only a problem when a Bose-Einstein condensate is imaged *in-situ*. When time-of-flight measurements are carried out, the size of the cloud is increased and the optical density is decreased, which reduces both the diffraction angle and the required spatial resolution.

3.2.2 Imaging setup

The imaging system used in the experiments is shown in Fig. 3.4. The light is brought close to the vacuum chamber through a single-mode polarization-maintaining fiber, collimated by a lens and sent through the cloud. The diameter of the imaging laser beam is 15 mm, to ensure that the light field is sufficiently flat at the location of the atoms. The frequency of the imaging light can be tuned to the $F = 1 \rightarrow F' = 0$ transition or to 30 MHz above the $F = 1 \rightarrow F' = 2$ transition be choosing a different diffraction order of the acousto-optical modulator (AOM). After the light has passed through the cloud, a second lens images the shadow onto a CCD camera. The focal length of this lens is 200 mm and the object distance is 300 mm, which yields a magnification of $M = 0.5$. The diameter of the imaging lens is 78 mm, which corresponds to a numerical aperture of $6.5 \cdot 10^{-2}$. The resolution is therefore limited to 5.5 μm. As this number is smaller than the pixel size of the CCD camera, the imaging system is not diffraction limited.

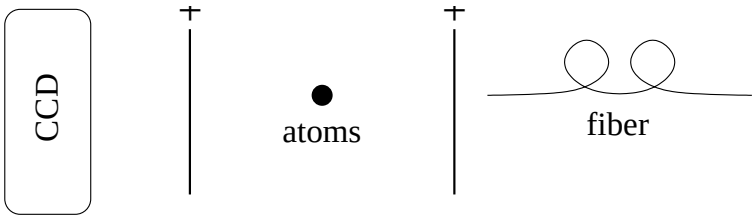

Figure 3.4: The setup for near-resonant absorption imaging. The light is brought to the chamber through a single-mode polarization-maintaining fiber. It is collimated by a lens and sent through the cloud. A second lens is used to image the shadow on a CCD camera.

3.2.3 CCD camera

The CCD camera is an Apogee AP1E, which is equiped with a Kodak KAF-0401E chip. The pixels on this chip have a full well electron depth of 100.000 electrons and a dynamic range of 14 bits. This means that one graylevel of the camera corresponds to about 6 electrons. With a quantum efficiency (QE) of 63%, 10 photons are needed to register a click, which corresponds to a fluence of $0.4\,\mathrm{pJ/cm^2}$, given the energy of a photon at 589 nm and the $9\,\mu$m pixel size. Making use if the fact that a pixel saturates at a fluence of $6.8\,\mathrm{nJ/cm^2}$, and if we assume an exposure time of 100 microseconds, we find that an intensity of $6.8 \cdot 10^{-}2\,\mathrm{mW/cm^2}$ is needed to saturate a pixel, which corresponds to 1% of the saturation intensity. This means that it is safe to neglect power broadening of the imaging transition.

The CCD camera has a mechanical shutter, which can be externally triggered. This shutter typically opens in a few milliseconds. However, the camera lacks a continuous readout mode. This means that the CCD starts accumulating dark counts as soon as it is armed. Because of the latencies of the computer that controls the camera we do not want to make any software calls during a shot of the experiment. This means that the camera has to be armed during the entire cycle of evaporative cooling, which can typically last 30 seconds. Because of this, the contribution of the dark current to the resulting image has to be analysed. The manifacturer of the chip quotes a maximum dark current of 50 electrons per pixel per second at a temperature of 25°C. Assuming the camera is armed for one minute, this leads to 3000 electrons per pixel, which corresponds to 500 graylevels. The manifacturer also quotes a dark signal doubling temperature of 7.5°C. The temperature of the camera can easily be lowered to −15°C using the onboard thermo-electric cooling, which yields a dark current of $500 \times (1/2)^{40/7.5} \approx 15$ graylevels. This corresponds to a signal to noise ratio of about .1%, which is acceptable.

Besides taking absorption images the camera can also be used to measure fluorescence. However, because the camera is not calibrated, these images cannot be used to measure the absolute density of particles. Only the width of the cloud can be determined and relative changes in intensity can be detected. Below we present results obtained by both fluorescence and absorption images and make a quantative comparison between the images.

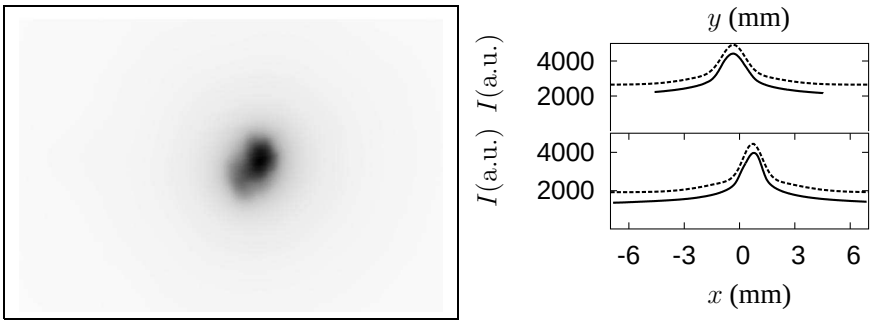

Figure 3.5: *In-situ* fluorescence image of the bright MOT measured through a neutral density filter with a 6% transmission. The figure on the right shows the projections on the x and y axis. The dotted lines show fits, which have been offset for clarity. The widths are $\Delta x = 0.72 \pm 0.003\,\mathrm{mm}$ and $\Delta y = 0.87 \pm 0.003\,\mathrm{mm}$.

3.3 Magneto-optical trapping

The first stage we analyse is the bright MOT. Our MOT is operated at a saturation parameters of $s_0 = 2 - 3$ and a detuning of 30 MHz below the $F = 2 \rightarrow F' = 3$ transition. The cooling beams are brought to the chamber through two single-mode polarization-maintaining fibers, one for the four beams in the plane between the coils and one for the two beams in the direction perpendicular to the coils. The repump light is overlapped with the light from the first fiber. Due to the large amount of fluorescence from the bright MOT, a neutral density filter has to be placed in front of the camera when the atoms are imaged *in-situ*, because otherwise the camera saturates even at the shortest setting for the shutter time. Fig. 3.5 is taken with an exposure time of 100 ms and a filter with 6% transmission. In this image it can be seen that for high densities, it is very difficult to align a bright MOT. This is due to the fact that the atoms absorb a large part of the cooling light, which causes a power imbalance in the retro-reflected beams. The figure on the right shows the projections on the x and y axis of the image. The dashed lines are fits to a distribution consisting of a wide and a narrow Gaussian profile. The wide Gaussian profile is present in all the fluoresence images presented in this chapter. The widths corresponding to this wide profile are in the order of 3 mm, independent of the condition of

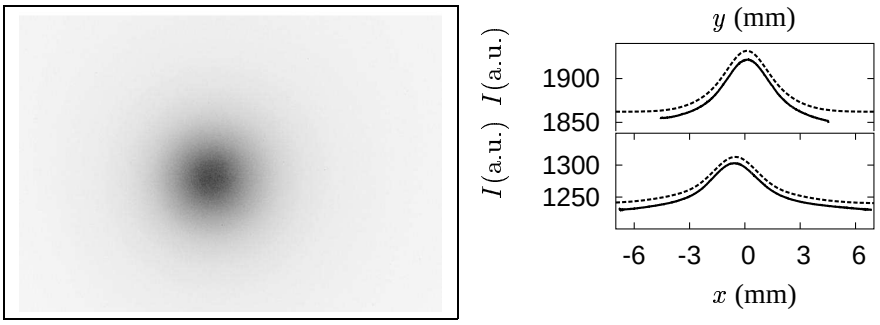

Figure 3.6: Fluorescence image of the bright MOT after 4 ms of expansion. The figure on the right shows the projections on the x and y axis. The dotted lines show fits, which have been offset for clarity. The widths are $\Delta x = 1.38 \pm 0.013$ mm and $\Delta y = 1.31 \pm 0.033$ mm.

the cloud of atoms, which indicates that this distribution is an artifact of the imaging system. The narrow distribution corresponds to the distribution of atoms.

It is also possible to make a fluorescence image of the atoms after ballistic expansion. To measure this, the MOT lasers and coils are switched off and the CCD shutter is opened. After a delay of a few milliseconds, the MOT lasers are shortly pulsed. In Fig. 3.6 the fluorescence image is shown, as well as the projections on the x and y axis.

3.4 Dark MOT

For the dark MOT, a dark spot of 3 mm in diameter is placed in the repumping beam between the fiber and the collimating lens. The dark MOT can be measured *in-situ* with absorption imaging, but also with fluorescence imaging. This is due to that fact that atoms in the dark region are repumped by spontaneously-emitted repump photons that are scattered into the region. There is also a contribution due to light scattered by the atoms outside the dark region. As in the case of the bright MOT it is not very useful to analyse the absolute signal. It is however important to mention that the atoms that contribute to the fluoresence in this image are only the atoms in the $F = 2$ ground state, which is typically in the order of 1%. The profiles in the x and y directions can again be fitted using a

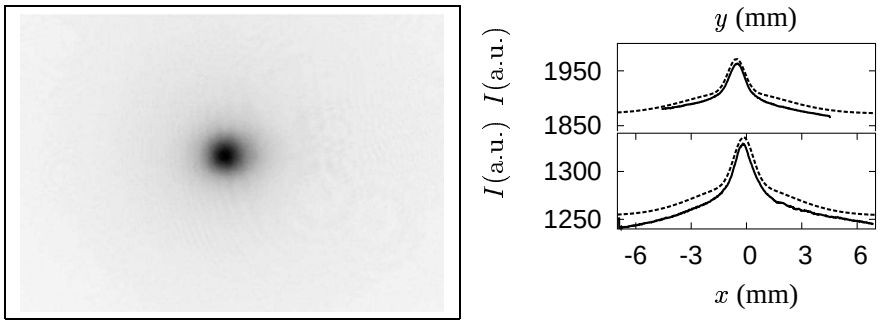

Figure 3.7: *In-situ* fluorescence image of the dark MOT. The figure on the right shows projection of the x and y axis. The dotted lines show fits, which have been offset for clarity. The widths are $\Delta x = 0.722 \pm 0.009\,\mathrm{mm}$ and $\Delta y = 0.63 \pm 0.008\,\mathrm{mm}$.

sum of two Gaussian shapes.

In order to image the atoms in the $F = 1$ state, absorption imaging is used. By substracting the fluorescence image in Fig. 3.7 from the bright-field image we can obtain a pure absorption image. The result of this procedure is shown in Fig. 3.8. The absorption image has been taken with a detuning of 30 MHz above the $F = 1 \rightarrow F' = 2$ transition instead of on resonance with the $F = 1 \rightarrow F' = 0$ transition in order not to black out the image at the higher optical densities. Note, that this image is an example of an absorption image as it appears on the camera. It has not been divided by a flat-field image and converted to optical densities. To fit this image, we assume Gaussian distribution for both the intensity of the light and the density of the atoms. We then fit to the Lambert-Beer law, which yields widths of $\Delta x = 1.63 \pm 0.02\,\mathrm{mm}$ and $\Delta y = 0.62 \pm 0.01\,\mathrm{mm}$. This result implies that the aspect ratio of the image is consistent with the gradients of the magnetic field of the MOT. The peak optical density of the cloud as determined by this method is $\mathrm{OD} = 35 \pm 5$ which corresponds to a number of trapped atoms of $N = 5 \cdot 10^8$. It is also interesting to note that the fluorescence image (Fig. 3.7) has an aspect ratio of one, which means that the shape of the $F = 2$ cloud is determined by other factors than the magnetic field.

To compare the dark MOT with the bright MOT we have taken an absorption image of the dark MOT after the same expansion time as in

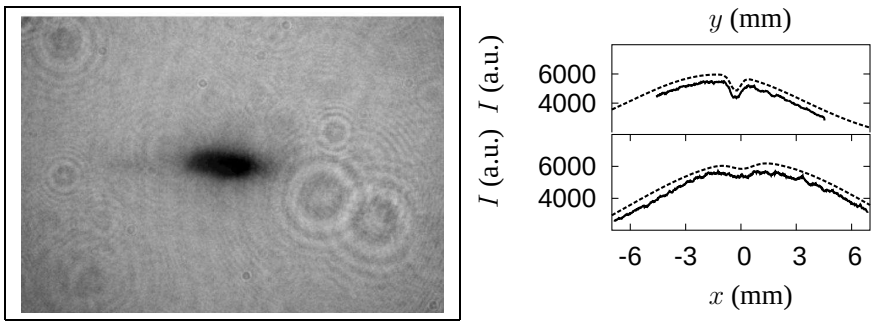

Figure 3.8: Direct *in-situ* absorption image of the dark MOT. The figure on the right shows projection of the x and y axis. This data has not been converted to optical densities. The dotted lines show fits, which have been offset for clarity. The widths are $\Delta x = 1.63 \pm 0.02\,\mathrm{mm}$ and $\Delta y = 0.62 \pm 0.01\,\mathrm{mm}$.

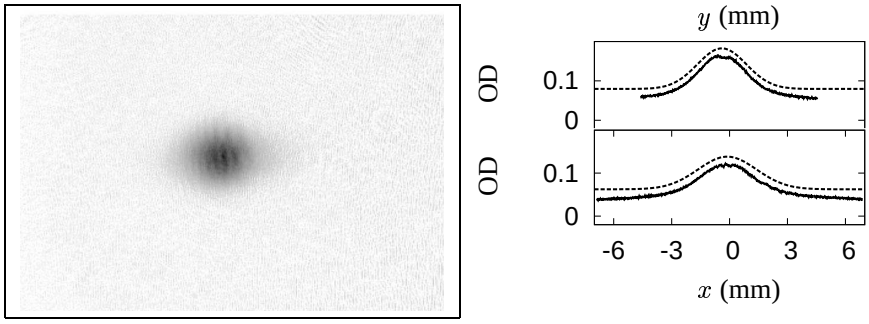

Figure 3.9: Absorption image of the dark MOT after 4 ms of expansion. The figure on the right shows projections of the x and y axis. The dotted lines shows fits, which are offset for clarity. The widths are $\Delta x = 2.15 \pm 0.01\,\mathrm{mm}$ and $\Delta y = 1.80 \pm 0.01\,\mathrm{mm}$.

Fig. 3.6. This image is shown in Fig. 3.9. The fits to this images yield widths of $\Delta x = 2.15 \pm 0.01\,\mathrm{mm}$ and $\Delta y = 1.80 \pm 0.01\,\mathrm{mm}$ and a peak optical density of $\mathrm{OD} = 0.236 \pm 0.002$, which corresponds to a central density of $n_0 = 9 \cdot 10^8\,\mathrm{cm}^{-3}$. This in turn corresponds to a total number of atoms of $N = 4 \cdot 10^7$. The aspect ratio of the cloud in this image is almost 1 due to the isotropic nature of the thermal expansion of the cloud. The widths are consistent with a temperature of $200\,\mu\mathrm{K}$. A more thorough analysis of the temperature of the atoms in the bright MOT and the dark MOT, as well as an analysis of dark polarization-gradient cooling will be given in Ref. [12].

3.5 Magnetic trapping

Atoms can be loaded into the magnetic trap by rapidly switching off the dark MOT and then switching on the currents of the magnetic trap (MT). The current in the MOT coils typically takes 3.5 ms to extinguish and the current in the MT coils take almost 10 ms to stabilize at the maximum value. Images of atoms in the magnetic trap can only be taken *in-situ* because the electronics to rapidly switch off the magnetic trap had not been installed at the time these initial measurements were performed. Also, two thirds of the atoms are lost due to the fact that in these measurements no spin-polarization stage has been employed. The maximum gradient of the magnetic field due to the cloverleaf coils is $100\,\mathrm{G/cm}$, the maximum curvature is $80\,\mathrm{G/cm}^2$ and the bias field is approximately zero. It is more convenient to write these values in units of temperature instead of magnetic field, which gives a gradient of $3.4\,\mathrm{mK/cm}$ and a curvature of $2.7\,\mathrm{mK/cm}^2$. The trapping frequency associated with the curvature is 16 Hz, but at zero bias field no frequency can be associated with the quadrupole directions, as the potential exhibits a cusp in those directions. In the following the trap was operated at 60% of the maximum currents. Note that the weak trapping direction of the magnetic trap corresponds to the strong trapping direction in the magneto-optical trap. The distribution in the radial direction is expected not to be Gaussian, but of the form $\exp(-|x|/\Delta x)$. The image in Fig. 3.10 is taken 11 ms after the MOT is turned off, which is more than sufficient to allow non-trapped atoms to escape from the view. As the image clearly shows the presence of atoms, it is safe to assume that these atoms are in fact trapped. Furthermore, the spatial distribution of

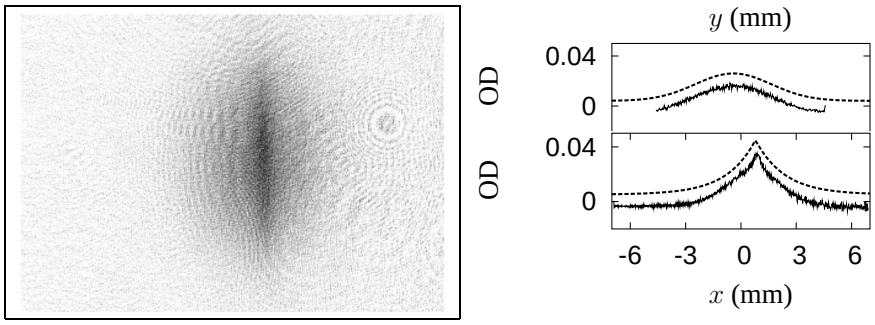

Figure 3.10: *In-situ* absorption image of atoms in the magnetic trap. The figure on the right shows the projections of the x and y axis. The fits, represented by the dotted line, have been offset for clarity. The widths are $\Delta x = 1.57 \pm 0.02\,\mathrm{mm}$ and $\Delta y = 2.92 \pm 0.03\,\mathrm{mm}$.

the atoms fits very well to the expected distribution. The width in the quadrupole direction $\Delta x = 1.57 \pm 0.02\,\mathrm{mm}$ and the width of the Gaussian in the curvature direction is given by $\Delta y = 2.92 \pm 0.03\,\mathrm{mm}$. Using the trap parameters, this yields a temperature of $T_x = 320 \pm 4\mu\,\mathrm{K}$ in the quadrupole direction and a temperature of $T_y = 138 \pm 3\mu\,\mathrm{K}$ in the curvature direction. This suggests that the atoms in the trap are not yet in thermal equilibrium. However, as these temperatures can not be verified by time-of-flight measurements at this point, this result is not conclusive. Using the peak positions, we can also obtain the peak optical density of the cloud, which equals $\mathrm{OD} = 0.061 \pm 0.001$. Extracting a density from this quantity is difficult since the relatively high temperature of the gas requires that the presence of the inhomogeneous magnetic field is taken into account. It is more convenient to measure the number of atoms in a time-of-flight experiment and calculating the peak optical density in the trap using the results of that measurement. However, as mentioned, the fast switches required to extinguish the magnetic fields are not yet installed.

3.6 Sequencer

In order to generate the complex sequence of events that is required to perform the above experiments, all of these events should be placed under computer control. The problem with modern computers is that they are

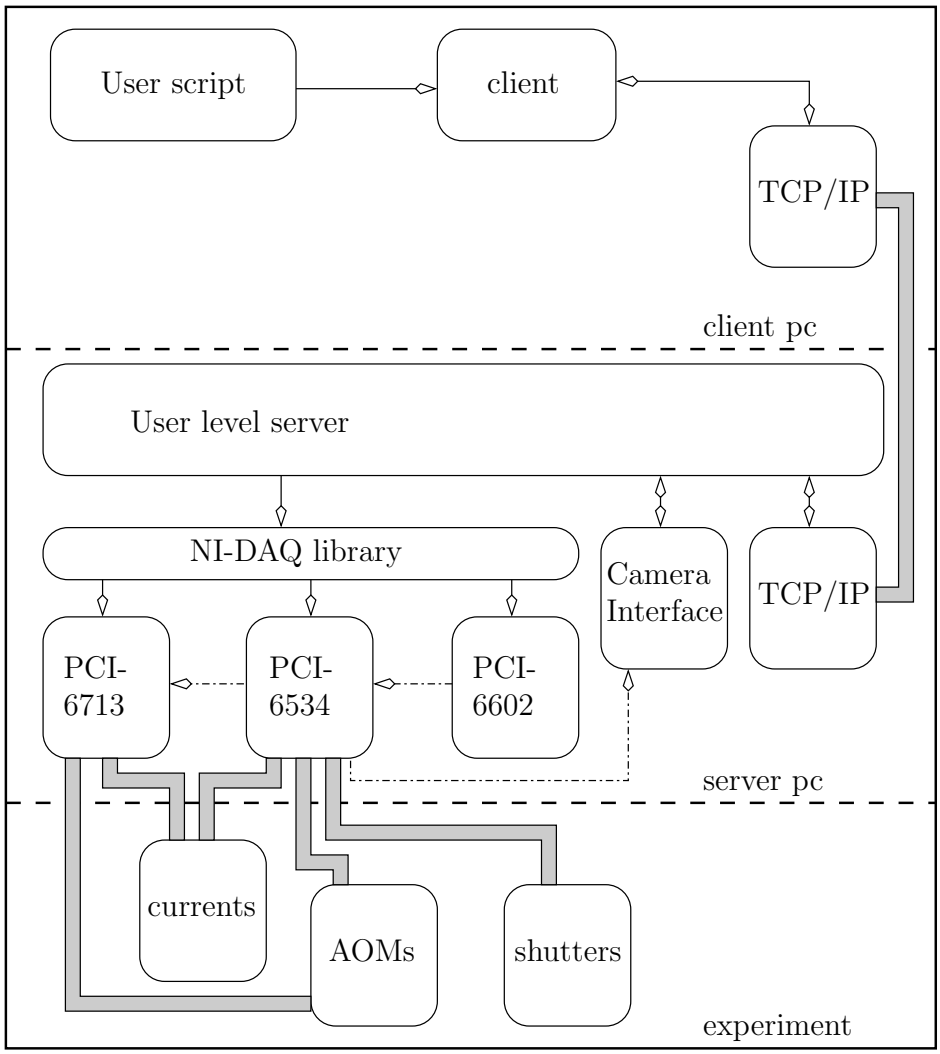

Figure 3.11: Functional diagram of the sequencing system. The upper layer and the middle layer are the client and the server, respectively. The client interacts with the user and the server interacts with the hardware. These layers are implemented on separate computers. The lower layer is the experimental apparatus. The arrows with solid lines indicate flow through software, the arrows with dash-dotted lines indicate hardware trigger lines between the cards in the server. The thick gray lines indicate twisted pair multicables that run throughout the lab.

optimized for average performance and not for absolute timing. This is achieved by delegating tasks to dedicated hardware such as direct memory access controllers. As a result of this, the programmer does not have fine-grained control over the timing on the various busses in the computer and does not have guarantees about when certain memory transfers are performed. To add to this problem modern operating systems are also optimized in the same way, giving the average user smooth performance but giving the demanding programmer no options to control the hardware directly.

To overcome these problems, the timing of the experiment is generated using dedicated hardware on PCI cards inside the computer. The computer is therefore reduced to a means of transfering data to this dedicated hardware on behalf of the user and storing the resulting measurements.

To make the sequencing system more robust, the actual sequencer and the user interface are installed on separate computers. The sequencer is implemented as a server and the user interface is a client to this server. By choosing such an architecture, the actual sequencer cannot be disrupted by bugs in the user interface. As user interfaces are generally considered to be more prone to bugs, this offers a significant improvement in stability. In short, we consider the sequencing system to consist of three layers: the client pc, the server pc and the experiment. This architecture is illustrated in Fig. 3.11. In the following, this functional diagram is used to explain the most important features of the sequencing system.

3.6.1 User interface

The upper layer in Fig. 3.11 is the user interface. The user can specify a sequence by writing a script in a language with a C-like syntaxis, that was developed especially for this experiment. The client application is used to compile the script into binary data. The compiler can be used to perform sanity checks to ensure that the script is logically consistent. After the binary data is generated, the client contacts the sequencer running on the server pc over a TCP/IP connection. Because the server and client are connected via a private local area network, this communication is fast and secure.

As the communication protocol between the server and the client is very well documented, it is relatively easy to write a completely different way of generating the binary data without having to rethink the hardware and

software of the actual sequencer.

3.6.2 Sequencer

The middle layer in Fig. 3.11 is the actual sequencer. This layer is by far the most complex as it interacts with all the hardware. After the server and the client have negotiated the transfer of data, the server interprets the data according to a strict and well-documented protocol. The experiment requires both analog and digital signals. The analog signals are generated by a National Instruments PCI-6713, which has eight output channels with 12 bit accuracy. The digital signals are generated using a National Instruments PCI-6534, which has 32 digital channels and an onboard buffer of 32 megabytes. The server extracts both the analog and digital data from the binary data and loads this data into the onboard buffers of these cards. As it is demanded that the experiment runs without operating-system intervention, the complete experimental sequence needs to fit into these onboard buffers. Since the most fine-grained parts of the experiment require at least a microsecond accuracy, the 32 megabytes of memory is not enough memory for the entire digital sequence, which can typically last up to 60 seconds. However, this accuracy is only required at the last stage of the experiment. The largest part of the experiment is spent during loading of the magneto-optical trap, the adiabatic compression of the magnetic trap and the evaporative cooling. None of these stages require more than a millisecond resolution. For that reason the experiment is split into two parts. In the first part the master clock runs with a millisecond period. After the evaporative cooling stage has finished, the clock is switched to a microsecond period for the diagnostic part of the experiment. This switching of the clock rate is achieved using a National Instruments PCI-6602, which contains eight general purpose counters. One of these counters is used to scale the onboard 180 MHz clock down to the update frequency that is required for the experiment. By programming the counter to run in frequency shift keying (FSK) mode, it is possible to choose the register from which the counter reloads after expiring, by applying a voltage to its gate. The hardware of the card allows us to connect this gate to the output of another one of the onboard counters, which we program to switch state after the appropriate number of clock pulses has been generated by the first counter. This setup results in a master clock that seamlessly switches from a low frequency to a high frequency after a time interval that can

be chosen by the user. This master clock can then be distributed among the other National Instruments cards using the real-time system interface (RTSI), thus bypassing the PCI bus.

The PCI-6713 card has an onboard buffer of 2000 analog samples per channel. The problem with this card is that the channels cannot be individualy triggered, which means that if only one channel should be ramped, all the other channels need to clock out a constant value. However, by efficiently distributing the samples among the analog events, the buffer is sufficient to prevent the requirement for memory updates during a run. The update signal for the analog card is connected to an output line of the digital card, which means the timing of the analog signals can be integrated in the timing of the digital signals.

Finally, the server also initializes the card that interfaces to the CCD camera. This card provides a rapid downloading of the image from the CCD to the computer in less then 1 second. Furthermore, it has digital input lines that, among other things, allow us to externally trigger the CCD camera to take an exposure. This line is also connected to the digital output card, thus integrating the CCD camera triggering into the rest of the digital sequencing. When an image is acquired, the server writes the image to a shared directory on the client pc.

3.6.3 Experiment

The lower layer of Fig. 3.11 represents the experimental setup. The analog signal generated by the sequencer are used to control the currents of the magnetic trap. The cloverleaf coils are powered by three Delta supplies type SM 30-100D with option P031. These supply 100 A at 30 V and are connected in parallel. The bias and pinch coils are connected in series and are powered by two of these same supplies. The current through the bias coils can be reduced by opening a high-current field-effect transistor (FET) that is connected in parallel with the bias coils. This FET is referred to as the shunt and can be controlled by applying a voltage between 0 and 5 V to the input. The currents generated by the power supplies can also be tuned from zero to full current by applying a programming voltage to the appropriate input. These programming voltages are connected to the analog output card via opto-couplers supplied by Delta as ISO AMP modules. These opto-couplers also contain a channel to route a digital signal to the power supplies, which is used to switch the supplies on and

off. These lines are connected to the digital output card.

The digital card is also used to control shutters and AOMs in the experiment. These are not opto-coupled, because the risks of ground loops and interference due to back EMF is considered negligible for these digital lines. To avoid overshoots and reflections, the signals are coupled into twisted pair cables using Schottky diodes to clamp the voltages between TTL levels and coupled out of the cable into Schmidt triggered gates to avoid false triggers due to jitter.

3.7 Conclusions and outlook

At the time of writing of the thesis, the number of atoms in the trap is not sufficient to start evaporative cooling. However, as will be discussed in Ref. [12], there are a number of steps that still require optimization. For instance, the hardware to switch the extraction coils was not available at the time the above experiments were carried out. Preliminary experiments suggest that adding this feature will yield a factor of 3 in the number of particles in the experiment. Furthermore, the magneto-optical lens has not been used in combination with the dark MOT, but measurements with the bright MOT prove that this will increase the loading rate by a factor of 3 as well. Furthermore, there were not enough AOMs available to generate a spin-polarization pulse, which means we always load only 1/3 of the atoms in the magnetic trap. This means we can expect to gain almost a factor of 30 in number of atoms once all these features have been implemented.

The most difficult step after that is the evaporative cooling. Work has started on the implemention of a synthesizer for the required rf frequencies, but coupling the rf power into the atoms will be difficult as the large amount of stainless steel might cause unpredictable behaviour of the radiation inside the vacuum chamber.

A laser system for the optical lattice is already present in the form of a 1 Watt Coherent 699 dye laser, pumped with a 5 Watt Coherent Verdi. If the power of the dye laser proves to be insufficient, the choice can also be made to make a blue-detuned lattice by using the Verdi directly.

Chapter 4

Quantum phases in an optical lattice

Abstract

We present the zero-temperature phase diagram of bosonic atoms in an optical lattice, using two different mean-field approaches. The phase diagram consists of various insulating phases and a superfluid phase. We explore the nature of the insulating phase by calculating both the quasiparticle and quasihole dispersion relation. We also determine the parameters of our single-band Bose-Hubbard model in terms of the microscopic parameters of the atoms in the optical lattice.

4.1 Introduction

Using the interference pattern of intersecting laser beams one can create a periodic potential for atoms, which is known as an optical lattice [3, 26]. Because one can confine atoms at separate lattice sites, one can accurately control the interaction between the atoms. This makes the optical lattice an important tool in spectroscopy, laser cooling [27] and quantum computing [28]. In the following we study some of the many-body aspects of such a lattice and in particular Bose-Einstein condensation of atoms in an

This chapter has been previously published as *Quantum phases in an optical lattice*, D. van Oosten, P. van der Straten, and H. T. C. Stoof, Phys. Rev. A **63**, 053601 (2001).

optical lattice. In contrast with the existing Bose-Einstein condensation experiments in an harmonic trap, the quantum depletion of the condensate in the case of Bose-Einstein condenstation in a lattice can be very large. We can therefore expect interesting features.

If we assume that the atoms are cooled to within the lowest Bloch band of the periodic potential, Jaksch *et al.* [9] have shown that we can describe the behavior of the atoms in an optical lattice with the Bose-Hubbard Hamiltonian

$$H = -t \sum_{\langle i,j \rangle} a_i^\dagger a_j + \frac{1}{2} U \sum_i a_i^\dagger a_i^\dagger a_i a_i - \mu \sum_i a_i^\dagger a_i, \tag{4.1}$$

where the sum in the first term on the right-hand side is restricted to nearest neighbours and $a_i^\dagger$ and a_i are the creation and annihilation operators of an atom at site i respectively[1]. The parameter t is the hopping parameter and U is the interaction strength, which we always assume to be positive in the following. The term involving the chemical potential μ is added because we perform our calculations in the grand-canonical ensemble.

Qualitatively we expect that when there is an integer number of particles at each site i and $t \ll U$, the interaction between the particles will make it energetically unfavourable for a particle to move from one site to another. In this situation the gas is in what is known as the Mott-insulator phase [29]. However, if we add in this phase a particle to the system, this particle will only receive a small energetic penalty when it moves, because its interaction energy is the same on each site. For this reason, a gas with a non-integer number of bosons at each site will be in a superfluid phase at zero-temperature. This expectation has been shown to be correct using Quantum Monte Carlo calculations [30] and several mean-field approaches [9, 31, 32]. In particular, Ref. [9] numerically determines interesting features of cold bosonic atoms in an inhomogeneous optical lattice. In this paper, we give a largely analytical means of understanding the results obtained by these authors.

In order to describe the zero-temperature phase transition from the superfluid to the Mott-insulating phase analytically, we need to make some appropriate mean-field approximation to the Hamiltonian in Eq. (4.1). A

[1] The operators $a_i^\dagger$ and a_i were denoted $c_i^\dagger$ and c_i, respectively, in the original publication.

more or less standard approach would be to use the Bogoliubov approximation. In Sec. 4.2 we show that this approximation does not predict the expected phase transition and we explain the absence of the phase transition. In Sec. 4.3 we analytically investigate an alternative mean-field theory, proposed by Sheshadri *et al.* [32], and compare the analytical results with exact numerical results. In Sec. 4.4 we discuss the properties of the Mott-insulating phases by calculating the quasiparticle and quasihole dispersions and finally in Sec. 4.5 we relate the parameters t and U to experimental parameters such as laser intensity and wave length.

4.2 Bogoliubov approximation

We first transform the Hamiltonian to momentum space by introducing creation and annihilation operators $a_{\mathbf{k}}^\dagger$ and $a_{\mathbf{k}}$ respectively, such that

$$a_i = \frac{1}{\sqrt{N_s}} \sum_{\mathbf{k}} a_{\mathbf{k}} e^{-i\mathbf{k}\cdot\mathbf{r}_i},\ a_i^\dagger = \frac{1}{\sqrt{N_s}} \sum_{\mathbf{k}} a_{\mathbf{k}}^\dagger e^{i\mathbf{k}\cdot\mathbf{r}_i}, \tag{4.2}$$

where N_s is the number of lattice site and $\mathbf{r}_i$ is the coordinate of site i. The wave vector $\mathbf{k}$ runs only over the first Brillouin zone. For mathematical convenience we take only a finite volume V, so that the momenta $\hbar\mathbf{k}$ are discretized, which allows us to write sums instead of integrals in Eq. (4.2). Later we will take the continuum limit $V \to \infty$. Using the fact that $\sum_i e^{-i(\mathbf{k}-\mathbf{k}')\cdot\mathbf{r}_i} = N_s \delta_{\mathbf{k},\mathbf{k}'}$, it is easily shown that the prefactor $1/\sqrt{N_s}$ ensures that the total number of particles obeys $N = \sum_i a_i^\dagger a_i = \sum_{\mathbf{k}} a_{\mathbf{k}}^\dagger a_{\mathbf{k}}$.

If we limit our description to cubic lattices with lattice distance a and substitute Eq. (4.2) into the Hamiltonian, we find

$$\begin{aligned} H = &\sum_{\mathbf{k}} (\epsilon_{\mathbf{k}} - \mu)\, a_{\mathbf{k}}^\dagger a_{\mathbf{k}} \\ &+ \frac{1}{2}\frac{U}{N_s} \sum_{\mathbf{k}} \sum_{\mathbf{k}'} \sum_{\mathbf{k}''} \sum_{\mathbf{k}'''} a_{\mathbf{k}}^\dagger a_{\mathbf{k}'}^\dagger a_{\mathbf{k}''} a_{\mathbf{k}'''} \delta_{\mathbf{k}+\mathbf{k}',\mathbf{k}''+\mathbf{k}'''}, \end{aligned} \tag{4.3}$$

where we defined $\epsilon_{\mathbf{k}} = -2t \sum_{j=1}^{d} \cos(k_j a)$, with d the number of dimensions[2]. For a Bose condensed gas the average number of condensate atoms

[2]The dispersion $\epsilon_{\mathbf{k}}$ was denoted $-\bar{\epsilon}_{\mathbf{k}}$ in the original publication.

N_c is a number much larger then one[3], which means that $N_c = \langle a_{\mathbf{0}}^\dagger a_{\mathbf{0}} \rangle \approx \langle a_{\mathbf{0}} a_{\mathbf{0}}^\dagger \rangle$ and we are allowed to take $N_c = \langle a_{\mathbf{0}}^\dagger \rangle \langle a_{\mathbf{0}} \rangle$.

Since $\langle a_{\mathbf{0}}^\dagger \rangle$ and $\langle a_{\mathbf{0}} \rangle$ are complex conjugates, we conclude that $\langle a_{\mathbf{0}}^\dagger \rangle = \langle a_{\mathbf{0}} \rangle = \sqrt{N_c}$, where we have chosen these expectation values to be real. The Bogoliubov approach consists of replacing the creation and annihilation operators by their average $\sqrt{N_c}$ plus a fluctuation

$$\begin{aligned} a_{\mathbf{0}}^\dagger &\to \sqrt{N_c} + a_{\mathbf{0}}^\dagger, \\ a_{\mathbf{0}} &\to \sqrt{N_c} + a_{\mathbf{0}}, \end{aligned} \tag{4.4}$$

and minimizing the energy of the gas with respect to the number of condensate atoms N_c. At the minimum, the part of the Hamiltonian that is linear in the fluctuations must therefore be zero. Performing the above subsitution and selecting the linear terms yields

$$H^{(1)} = (\epsilon_{\mathbf{0}} - \mu + \frac{U}{N_s} N_c) \sqrt{N_c} (a_{\mathbf{0}}^\dagger + a_{\mathbf{0}}), \tag{4.5}$$

where the superscript denotes the order in the fluctuations. Since $H^{(1)}$ must be zero for all $a_{\mathbf{0}}^\dagger$ and $a_{\mathbf{0}}$ we conclude that in the lowest order approximation

$$\mu = U n_0 - zt, \tag{4.6}$$

in terms of the condensate density $n_0 = N_c/N_s$ and the number of nearest neighbours $z = 2d$. This expression can be easily understood since the chemical potential is the energy needed to add one particle to the system. Adding one particle results in an energy increase due to the interaction with the n_0 particles already at each site, and an energy decrease due to the possible hopping to one of z nearest-neighbour sites.

Next we determine the effective Hamiltonian H^{eff}, which contains only the parts of zeroth and second order in the fluctuations. The zeroth-order term is found by subtituting all creation and annihilation operators by $\sqrt{N_c}$. To find the quadratic term, we substitute in the interaction term two creation or annihilation operators at a time by $\sqrt{N_c}$ and write down

[3]The number of condensate atoms N_c was denoted N_0 in the original publication.

all possible combinations. Performing the summation over one of the remaining momenta yields finally

$$H^{\text{eff}} = \left(-2z - \mu + \frac{1}{2}Un_0\right) N_{\text{c}} + \sum_{\mathbf{k}} \left(\epsilon_{\mathbf{k}} - \mu\right) a_{\mathbf{k}}^{\dagger} a_{\mathbf{k}} + \frac{1}{2}Un_0 \sum_{\mathbf{k}} \left(a_{\mathbf{k}} a_{-\mathbf{k}} + 4a_{\mathbf{k}}^{\dagger} a_{\mathbf{k}} + a_{-\mathbf{k}}^{\dagger} a_{\mathbf{k}}^{\dagger}\right). \tag{4.7}$$

We can simplify this expression somewhat by using the commutation relation $[a_{\mathbf{k}}, a_{\mathbf{k}}^{\dagger}] = 1$. If we also substitute Eq. (4.6) and write $\bar{\epsilon}_{\mathbf{k}} = 2zt + \epsilon_{\mathbf{k}}$, we find[4]

$$H^{\text{eff}} = -\frac{1}{2}Un_0 N_{\text{c}} - \frac{1}{2}\sum_{\mathbf{k}} \left(\bar{\epsilon}_{\mathbf{k}} + Un_0\right) + \frac{1}{2}\sum_{\mathbf{k}} \left(a_{\mathbf{k}}^{\dagger}, a_{-\mathbf{k}}\right) \begin{bmatrix} \bar{\epsilon}_{\mathbf{k}} + Un_0 & Un_0 \\ Un_0 & \bar{\epsilon}_{\mathbf{k}} + Un_0 \end{bmatrix} \begin{pmatrix} a_{\mathbf{k}} \\ a_{-\mathbf{k}}^{\dagger} \end{pmatrix}, \tag{4.8}$$

where the extra zeroth-order terms are generated by the commutation of $a_{\mathbf{k}}^{\dagger}$ and $a_{\mathbf{k}}$.

The effective Hamiltonian is diagonalized by a Bogoliubov transformation. This implies that we define new creation and annihilation operators $b_{\mathbf{k}}^{\dagger}$ and $b_{\mathbf{k}}$ for which the effective Hamiltonian is diagonal, by means of

$$\begin{pmatrix} b_{\mathbf{k}} \\ b_{-\mathbf{k}}^{\dagger} \end{pmatrix} = \begin{bmatrix} u_{\mathbf{k}} & v_{\mathbf{k}} \\ v_{\mathbf{k}}^{*} & u_{\mathbf{k}}^{*} \end{bmatrix} \begin{pmatrix} a_{\mathbf{k}} \\ a_{-\mathbf{k}}^{\dagger} \end{pmatrix} \equiv \mathbf{B} \begin{pmatrix} a_{\mathbf{k}} \\ a_{-\mathbf{k}}^{\dagger} \end{pmatrix}. \tag{4.9}$$

To ensure that the operators $b_{\mathbf{k}}^{\dagger}$ and $b_{\mathbf{k}}$ still obey the standard commutation relations for bosonic creation and annihilation operators, we have to demand that the coefficients of matrix $\mathbf{B}$ obey

$$|u_{\mathbf{k}}|^2 - |v_{\mathbf{k}}|^2 = 1. \tag{4.10}$$

If we now substitute Eq. (4.9) into Eq. (4.8) and demand that the result reduces to the diagonal Hamiltonian

$$H^{\text{eff}} = -\frac{1}{2}Un_0 N_{\text{c}} + \frac{1}{2}\sum_{\mathbf{k}} \left[\hbar\omega_{\mathbf{k}} - \left(\bar{\epsilon}_{\mathbf{k}} + Un_0\right)\right] + \sum_{\mathbf{k}} \hbar\omega_{\mathbf{k}} b_{\mathbf{k}}^{\dagger} b_{\mathbf{k}}, \tag{4.11}$$

[4]The dispersion $\bar{\epsilon}_{\mathbf{k}}$ was denoted $\epsilon_{\mathbf{k}}$ in the original publication.

we find that $u_{\mathbf{k}}$ and $v_{\mathbf{k}}$ must be solutions of the following two equations:

$$\begin{aligned}\left((u_{\mathbf{k}})^2+(v_{\mathbf{k}})^2\right)Un_0-2u_{\mathbf{k}}v_{\mathbf{k}}(\bar{\epsilon}_{\mathbf{k}}+Un_0)=0,\\ \left(|u_{\mathbf{k}}|^2+|v_{\mathbf{k}}|\right)^2(\bar{\epsilon}_{\mathbf{k}}+Un_0)-(u_{\mathbf{k}}^*v_{\mathbf{k}}+u_{\mathbf{k}}v_{\mathbf{k}}^*)Un_0=\hbar\omega_{\mathbf{k}}.\end{aligned} \tag{4.12}$$

Using the normalization in Eq. (4.10), we can easily find the solution

$$\hbar\omega_{\mathbf{k}}=\sqrt{\bar{\epsilon}_{\mathbf{k}}^2+2Un_0\bar{\epsilon}_{\mathbf{k}}}, \tag{4.13}$$

$$|v_{\mathbf{k}}|^2=|u_{\mathbf{k}}|^2-1=\frac{1}{2}\left(\frac{\bar{\epsilon}_{\mathbf{k}}+Un_0}{\hbar\omega_{\mathbf{k}}}-1\right). \tag{4.14}$$

To also obtain the condensate density n_0, which until now has been arbitrary, we now need to calculate the total density n as given by our effective Hamiltonian. The total density is thus given by

$$n=\frac{1}{N_s}\sum_{\mathbf{k}}\langle a_{\mathbf{k}}^\dagger a_{\mathbf{k}}\rangle_{H^{\text{eff}}}, \tag{4.15}$$

where the brackets $\langle\rangle_{H^{\text{eff}}}$ denote the expectation value as calculated with the effective Hamiltonian H^{eff}. For a Bose condensed gas, this density consists of two parts: the density associated with the macroscopic occupation of the one-particle ground-state, i.e., the condensate, and the density due to the occupation of the higher lying one-particle states. In this case, the condensate density equals the parameter n_0 and the density of the non-condensate part is determined by an average over the quadratic fluctuations, which will be a function of n_0. Calculating the average over the quadratic fluctuations by means of Eq. (4.9) yields first of all

$$n=n_0+\frac{1}{N_s}\sum_{\mathbf{k}\neq 0}\left[\left(|u_{\mathbf{k}}|^2+|v_{\mathbf{k}}|^2\right)\langle b_{\mathbf{k}}^\dagger b_{\mathbf{k}}\rangle_{H^{\text{eff}}}+|v_{\mathbf{k}}|^2\right]. \tag{4.16}$$

If we then use Eq. (4.14) and substitute the Bose distribution evaluated at $\hbar\omega_{\mathbf{k}}$ for $\langle b_{\mathbf{k}}^\dagger b_{\mathbf{k}}\rangle_{H^{\text{eff}}}$ we find that

$$n=n_0+\frac{1}{N_s}\sum_{\mathbf{k}\neq 0}\left(\frac{\bar{\epsilon}_{\mathbf{k}}+Un_0}{\hbar\omega_{\mathbf{k}}}\frac{1}{e^{\beta\hbar\omega_{\mathbf{k}}}-1}+\frac{\bar{\epsilon}_{\mathbf{k}}+Un_0-\hbar\omega_{\mathbf{k}}}{2\hbar\omega_{\mathbf{k}}}\right). \tag{4.17}$$

In the zero-temperature limit, $\beta\to\infty$, the first term in the summant is zero. Taking the continuum limit by using $\sum_{\mathbf{k}}\to V\int_{-\pi/a}^{\pi/a}d\mathbf{k}/(2\pi)^d$,

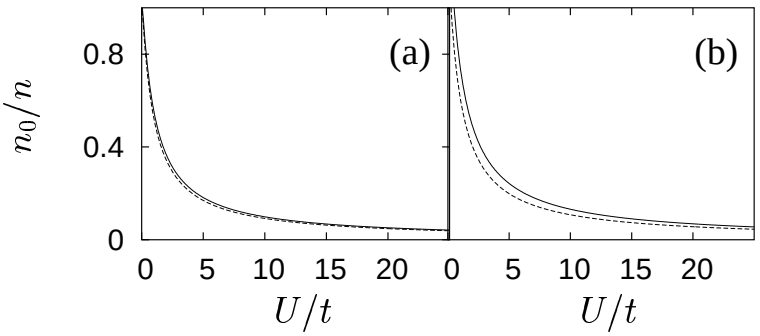

Figure 4.1: The condensate fraction n_0/n (a) in a two-dimensional optical lattice and (b) a three-dimensional optical lattice, both as a function of U/t for $n = 0.5$ (dashed line) and $n = 1.0$ (dotted line).

changing from momenta $\mathbf{k}$ to $\mathbf{k}' = 2\pi\mathbf{k}/a$, and realizing that $N_s = V/a^d$, we arrive at the expression

$$n = n_0 + \frac{1}{2}\int_{-1/2}^{1/2} d\mathbf{k}' \left(\frac{\bar{\epsilon}'_{\mathbf{k}} + Un_0}{\hbar\bar{\omega}'_{\mathbf{k}}} - 1 \right), \tag{4.18}$$

with $\bar{\epsilon}'_{\mathbf{k}} = 2t\sum_{j=1}^{d}[1-\cos(2\pi k'_j)]$ and $\hbar\bar{\omega}' = (\bar{\epsilon}'^2_{\mathbf{k}} + 2Un_0\bar{\epsilon}'_{\mathbf{k}})^{1/2}$. We can now obtain the condensate density by solving Eq. (4.18) for n_0 for a fixed value of n. We expect that at integer n, for a fixed value of U/t there will be no superfluid solution and this will mark the phase transition to the insulating phase as predicted by [9, 30, 31, 32].

4.2.1 Numerical results

In Fig. 4.1(a) we plotted the result of this calculation for a two dimensional lattice. We see from this figure, that there is only a marginal difference between the case that $n = 0.5$ and $n = 1.0$. In Fig. 4.1(b) we plotted the result for a three dimensional lattice. In this case the difference between half filling and integer filling is somewhat larger, but there is clearly no critical value of U/t for which the condensate density goes to zero.

These results lead to the suspicion that the phase transition to the insulating phase is not present in this approximation. To verify this, we investigate the limit of $U/t \to \infty$ in some detail.

4.2.2 Asymptotic behavior

When $U/t \to \infty$ we intuitively expect the system to become an insulator, because it effectively means that the hopping parameter goes to zero. We therefore expect that there are no superfluid solutions as $U/t \to \infty$. We can see that in this limit the integrand in the right hand side of Eq. (4.18) behaves as $(Un_0/2\bar{\epsilon}'_{\mathbf{k}})^{1/2}$. One can also prove that $\bar{\epsilon}'_{\mathbf{k}} \leq 4\pi^2|\mathbf{k}'|^2 t$. This means that

$$\int_{-1/2}^{1/2} d\mathbf{k}' \frac{\bar{\epsilon}'_{\mathbf{k}} + Un_0}{\sqrt{\bar{\epsilon}'^2_{\mathbf{k}} + 2U\bar{\epsilon}'_{\mathbf{k}} n_0}} \geq \frac{1}{2\pi}\sqrt{\frac{Un_0}{2t}} \int_{-1/2}^{1/2} \frac{d\mathbf{k}'}{|\mathbf{k}'|}. \tag{4.19}$$

The integral at the right hand side of Eq. (4.19) can be done analytically in two dimensions and numerically in three dimensions. When we call the result of the integration in d dimensions I_d, we see that Eq. (4.18), for $U/t \to \infty$, reduces to

$$n \approx n_0 + \frac{1}{4\pi}\sqrt{\frac{Un_0}{2t}} I_d - \frac{1}{2}, \tag{4.20}$$

where $I_2 = 2.22322$ and $I_3 = 2.38008$. This is a quadratic equation in $\sqrt{n_0}$ which always yields a positive solution for n_0 given by

$$n_0 = \left(\frac{1}{2}\sqrt{\frac{{I_d}^2}{16\pi^2}\frac{U}{2t} + 4n + 2} - \frac{I_d}{8\pi}\sqrt{\frac{U}{2t}} \right)^2. \tag{4.21}$$

We can correct for the error we made in Eq. (4.19) by using a higher value for I_d, but while this may change the value of n_0, it will still yield a positive solution. We see from Eq. (4.21) that $\lim_{U/t\to\infty} n_0 = 0$ as expected, so we can conclude that the Bogoliubov approximation as described above does not predict the phase transition to the Mott-insulator phase in two and three dimensions. The reason for this is that the Bogoliubov approach only approximately treats the interactions. As a result, the Bogoliubov approach cannot describe large depletions of the condensate.

We also see from Eq. (4.19) that in one dimension I_1 diverges. Substituting this in Eq. (4.20), we see that there are no Bose-condensed solutions, i.e., solutions with $n_0 \neq 0$, in one dimension. This is in accordance with the Mermin-Wagner-Hohenberg theorem [33, 34, 35].

As the Bogoliubov approximation fails to predict the phase transition to the Mott-insulator phase, we now consider a different mean-field theory that treats the interactions exactly and approximates the kinetic energy of the atoms in the optical lattice.

4.3 Decoupling approximation

To arrive at a mean-field approach that is capable of describing the Mott-insulating phase, we start again from Eq. (4.1). Analogous to the Bogoliubov approach, we introduce the superfluid order parameter $\psi = \sqrt{n_i} = \langle a_i^\dagger \rangle = \langle a_i \rangle$, where n_i is the expectation value of the number of particles on site i. Note that we take the expectation values to be real, as before. We now, however, construct a consistent mean-field theory by substituting

$$\begin{aligned} a_i^\dagger a_j &= \langle a_i^\dagger \rangle a_j + a_i^\dagger \langle a_j \rangle - \langle a_i^\dagger \rangle \langle a_j \rangle \\ &= \psi \left(a_i^\dagger + a_j \right) - \psi^2, \end{aligned} \tag{4.22}$$

into Eq. (4.1). Performing the substitution yields

$$\begin{aligned} H^{\text{eff}} = &-zt\psi \sum_i \left(a_i^\dagger + a_i \right) + zt\psi^2 N_s \\ &+ \frac{1}{2} U \sum_i a_i^\dagger a_i^\dagger a_i a_i - \mu \sum_i a_i^\dagger a_i, \end{aligned} \tag{4.23}$$

where $z = 2d$ is again the number of nearest-neighbour sites and N_s is the total number of lattice sites, as before. This Hamiltonian is diagonal with respect to the site index i, so we can use an effective onsite Hamiltonian. If we introduce $\bar{U} = U/zt$, $\bar{\mu} = \mu/zt$ and the number operator $n_i = a_i^\dagger a_i$, we find

$$H_i^{\text{eff}} = \frac{1}{2} \bar{U} n_i \left(n_i - 1 \right) - \bar{\mu} n_i - \psi \left(a_i^\dagger + a_i \right) + \psi^2, \tag{4.24}$$

which is valid on each site i. We will therefore drop the subscript i in the following. Note that we scaled all the energies by a factor $1/zt$, making this Hamiltonian a dimensionless operator.

After writing Eq. (4.24) in matrix form with respect to an occupation number basis, we can solve the problem numerically by explicitely diagonalizing the part of the matrix with occupation number below a certain

maximum value [32]. Later we also follow this procedure, but we first determine the phase diagram analytically using second-order perturbation theory.

4.3.1 Second-order perturbation theory

When we write $H^{\text{eff}} = H^{(0)} + \psi V$, with

$$\begin{aligned} H^{(0)} &= \frac{1}{2}\bar{U}n\,(n-1) - \bar{\mu}n + \psi^2, \\ V &= -\left(a^\dagger + a\right), \end{aligned} \tag{4.25}$$

we see that in an occupation number basis the odd powers of the expansion of the energy in ψ will always be zero. If we denote the unperturbed energy of the state with exactly n particles by $E_n^{(0)}$, we find that the unperturbed ground-state energy is given by

$$E_{N_0}^{(0)} = \left\{ E_n^{(0)} | n = 0, 1, 2, ... \right\}_{\min}.$$

Comparing $E_n^{(0)}$ and $E_{n+1}^{(0)}$ yields

$$E_{N_0}^{(0)} = \begin{cases} 0 & \text{if } \bar{\mu} < 0, \\ \frac{1}{2}\bar{U}N_0(N_0-1) - \bar{\mu}N_0 & \text{if } \bar{U}(N_0-1) < \bar{\mu} < \bar{U}N_0. \end{cases} \tag{4.26}$$

Next, we calculate the second-order correction to the energy with the well-known expression

$$E_{N_0}^{(2)} = \psi^2 \sum_{n \neq N_0} \frac{|\langle N_0|V|n\rangle|^2}{E_{N_0}^{(0)} - E_n^{(0)}}, \tag{4.27}$$

where $|n\rangle$ denotes the unperturbed wave function with n particles, of which the state with $n = N_0$ particles is the ground state[5]. Since the interaction V couples only to states with one more or one less atom than in the ground-state, we find

$$E_{N_0}^{(2)} = \frac{N_0}{\bar{U}(N_0-1) - \bar{\mu}} + \frac{N_0+1}{\bar{\mu} - \bar{U}N_0}. \tag{4.28}$$

[5]The filling factor N_0 was denoted g in the original publication

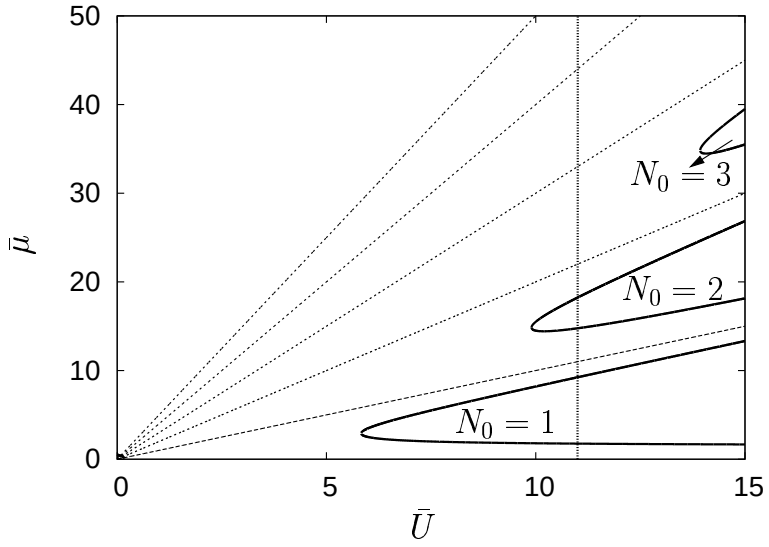

Figure 4.2: Phase diagram of the Bose-Hubbard Hamiltonian as obtained from second-order perturbation theory (solid lines). The dotted lines indicate the zeroth-order phase diagram. Later on, Fig. 4.5 is taken along the dashed line in this figure.

If we now follow the usual Landau procedure for second-order phase transitions by writing the ground-state energy as an expansion in ψ

$$E_{N_0}(\psi) = a_0(N_0, \bar{U}, \bar{\mu}) + a_2(N_0, \bar{U}, \bar{\mu})\psi^2 + \mathcal{O}(\psi^4), \tag{4.29}$$

and minimize it as a function of the superfluid order parameter ψ, we find that $\psi = 0$ when $a_2(N_0, \bar{U}, \bar{\mu}) > 0$ and that $\psi \neq 0$ when $a_2(N_0, \bar{U}, \bar{\mu}) < 0$. This means that $a_2(N_0, \bar{U}, \bar{\mu}) = 0$ signifies the boundary between the superfluid and the insulator phases. Solving

$$a_2(N_0, \bar{U}, \bar{\mu}) = \frac{N_0}{\bar{U}(N_0 - 1) - \bar{\mu}} + \frac{N_0 + 1}{\bar{\mu} - \bar{U}N_0} + 1 = 0,$$

yields

$$\bar{\mu}_\pm = \frac{1}{2}\left(\bar{U}(2N_0 - 1) - 1\right) \pm \frac{1}{2}\sqrt{\bar{U}^2 - 2\bar{U}(2N_0 + 1) + 1}, \tag{4.30}$$

where the subscript $\pm$ denotes the upper and lower halves of the Mott insulating regions of phase space. Note that this result is exact within our mean-field theory. Fig. 4.2 shows a plot of Eq. (4.30) for $N_0 = 1, 2, 3$. By equating $\bar{\mu}_+$ and $\bar{\mu}_-$ we can find the point of smallest $\bar{U}$ for each lobe. Denoting this critical value of $\bar{U}$ by $\bar{U}_c$ we have

$$\bar{U}_c = 2N_0 + 1 + \sqrt{(2N_0+1)^2 - 1}. \tag{4.31}$$

which yields $\bar{U}_c \approx 5.83$ for the $N_0 = 1$ insulator, a value also found by [32].

4.3.2 Fourth-order perturbation theory

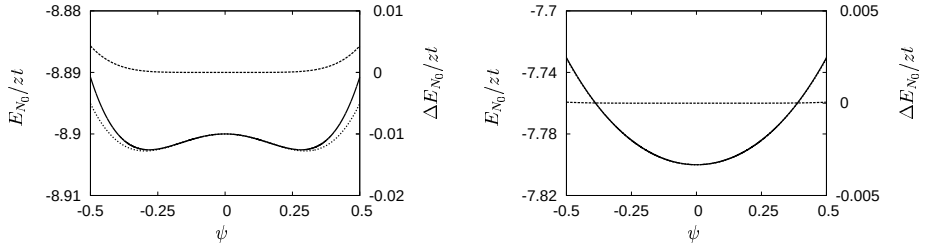

Figure 4.3: Ground-state energy as a function of ψ for (a) $\bar{U} = 11$ and $\bar{\mu} = 8.9$ and for (b) $\bar{U} = 11$ and $\bar{\mu} = 7.8$. The solid line represents fourth-order perturbation theory whereas the dotted line represents a numerical diagonalization of the effective Hamiltonian. The dashed line is the difference between the two (scale on the right).

To find out more about the phase transition, we now carry out fourth-order perturbation theory to find the rate with which the particle density increases as a function of $\bar{\mu}$. In Sec. 4.A, we present a way to calculate the higher-order terms in the perturbation series. Using this procedure we can write the ground-state energy as

$$E_{N_0}(\psi) = a_0(N_0, \bar{U}, \bar{\mu}) + a_2(N_0, \bar{U}, \bar{\mu})\psi^2 + a_4(N_0, \bar{U}, \bar{\mu})\psi^4, \tag{4.32}$$

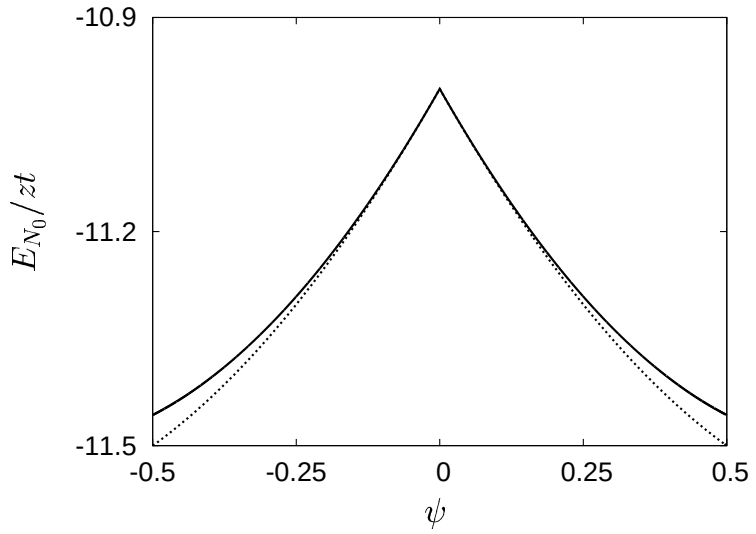

Figure 4.4: Ground-state energy as a function of ψ for $\bar{U} = \bar{\mu} = 11$, as obtained from first-order perturbation theory (solid line) and from numerical diagonalization of the effective Hamiltonian (dotted line).

with

$$\begin{aligned} a_4(N_0, \bar{U}, \bar{\mu}) = & \frac{N_0(N_0-1)}{\left(\bar{U}(N_0-1)-\bar{\mu}\right)^2\left(\bar{U}(2N_0-3)-2\bar{\mu}\right)} \\ & + \frac{(N_0+1)(N_0+2)}{\left(\bar{\mu}-\bar{U}N_0\right)^2\left(2\bar{\mu}-\bar{U}(2N_0+1)\right)} \\ & - \left(\frac{N_0}{\bar{U}(N_0-1)-\bar{\mu}} + \frac{N_0+1}{\bar{\mu}-\bar{U}N_0}\right) \\ & \times \left(\frac{N_0}{\left(\bar{U}(N_0-1)-\bar{\mu}\right)^2} + \frac{N_0+1}{\left(\bar{\mu}-\bar{U}N_0\right)^2}\right). \end{aligned} \tag{4.33}$$

In Figs. 4.3(a) and (b) we show plots of Eq. (4.32) together with the result of an exact numerical diagonalization of the effective Hamiltonian. As can be seen, the overlap is very good near the boundary given by Eq. (4.30). In Fig. 4.4 it can be seen that the numerical result exhibits a cusp when $\bar{U} = \bar{\mu}$, which is not predicted by Eq. (4.32). This is due to the fact that

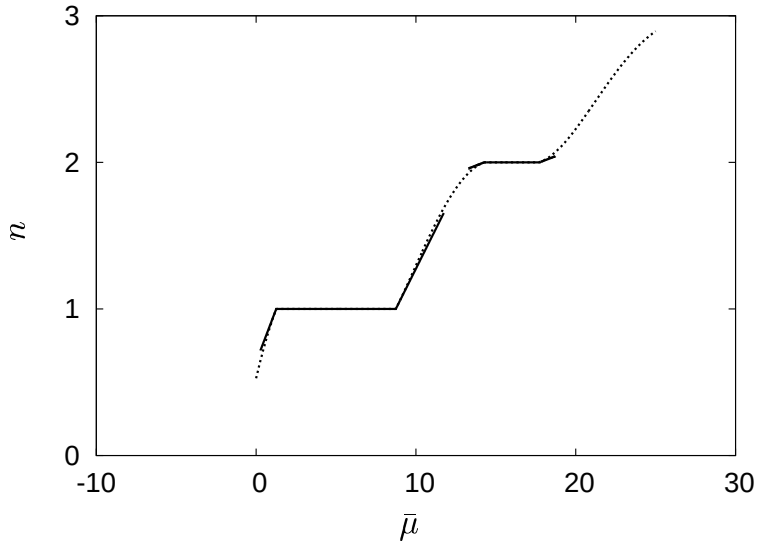

Figure 4.5: The density as a function of chemical potential $\bar{\mu} = \mu/zt$ for an interaction strength of $\bar{U} = U/zt = 11$, i.e., along the dashed line in Fig. 4.2.

in this particular case we need to use first-order degenerate perturbation theory, because at $\bar{\mu} = n\bar{U}$ the states with $n-1$ and n particles per site form a doubly degenerate ground-state. The resulting expression for the ground state energy is now nonanalytic and given by

$$E_{N_0}(\psi)|_{\bar{\mu}=n\bar{U}} = -\frac{1}{2}\bar{U}n(n+1) + \psi^2 - |\psi|\sqrt{n+1}, \tag{4.34}$$

which is the solid line in Fig. 4.4. Note that the occurence of a cusp is analogous to the well-known Jahn-Teller effect in solid-state physics [36].

We now continue by calculating the average number of particles per site in the grand-canonical ensemble by

$$\begin{aligned} n &= -\frac{\partial\langle H^{\text{eff}}\rangle}{\partial\mu} = -\frac{\partial E_{N_0}(\psi=\psi_{\min})}{\partial\bar{\mu}} \\ &= N_0 - \frac{\partial}{\partial\bar{\mu}}\left(\frac{a_2(N_0,\bar{U},\bar{\mu})^2}{4a_4(N_0,\bar{U},\bar{\mu})}\right), \end{aligned} \tag{4.35}$$

where $\psi_{\min} = [-a_2(N_0,\bar{U},\bar{\mu})/2a_4(N_0,\bar{U},\bar{\mu})]^{1/2}$ is the minimum of Eq. (4.32). Making use of the previous results, we can now plot the density as a func-

tion of $\bar{\mu}$ for a fixed value of $\bar{U}$. Between the edges $\bar{\mu}_{\pm}$, the density will remain constant because $\psi_{\min} = 0$ and the second term in the right-hand side of Eq. (4.35) does not contribute. Outside that region, the density will start to change with a nonzero slope. In Fig. 4.5 this is plotted for $\bar{U} = 11$. The solid line shows the result of the calculation described above and the dash-dotted line is a numerical result obtained by exact diagonalization. As can be seen, the analytical results are in good agreement with the numerical calculation. We can now also qualitatively understand the solution found numerically by Jaksch *et al.* [9] for an optical lattice in an external harmonic trap. In a first approximation, we can describe the effect of a slowly varying trapping potential by substituting $\bar{\mu}$ in Eq. (4.35) by $\bar{\mu}' = \bar{\mu} + V(\mathbf{r})$, where $V(\mathbf{r})$ is the external trapping potential. Combining this with Fig. 4.5 yields the density profile found in [9].

4.4 Dispersion relation

An important property of the Mott-insulating phase is that the fluctuation in the average number of particles per site goes to zero at zero temperature. Since these fluctuations can be described as quasiparticle and quasihole excitations, we will study these now. We calculate the quasiparticle and quasihole dispersions using a functional-integral formalism. We start by deriving an expression for the effective action. Readers unfamiliar with functional integrals may want to skip to subsection 4.4.2, where we discuss the results of the calculation.

4.4.1 The effective action

We define complex functions $a_i^*(\tau)$ and $a_i(\tau)$, respectively, and write the grand-canonical partition function as

$$Z = \mathrm{Tr} e^{-\beta H} = \int \mathcal{D}a^* \mathcal{D}a \exp\{-S[a^*, a]/\hbar\}, \tag{4.36}$$

where the action $S[a^*, a]$ is given by

$$S[a^*, a] = \int_0^{\hbar\beta} d\tau \left[\sum_i a_i^* \left(\hbar \frac{\partial}{\partial \tau} - \mu \right) a_i - \sum_{ij} t_{ij} a_i^* a_j + \frac{1}{2} U \sum_i a_i^* a_i^* a_i a_i \right], \tag{4.37}$$

with $\beta = 1/k_B T$, k_B Boltzmann's constant and T the temperature. To decouple the hopping term, we perform a Hubbard-Stratonovich transformation by adding a complete square to the action, which then becomes

$$S[a^*, a, \psi^*, \psi] = S[a^*, a] + \int_0^{\hbar\beta} d\tau \sum_{ij} (\psi_i^* - a_i^*)\, t_{ij}\, (\psi_j - a_j)\,. \tag{4.38}$$

Here ψ^* and ψ are the order parameter fields. To obtain an effective action as a function of these fields, we rewrite Eq. (4.38) as

$$\begin{aligned} S[a^*, a, \psi^*, \psi] = \int_0^{\hbar\beta} d\tau \Bigg[& \sum_i a_i^* \left(\hbar \frac{\partial}{\partial \tau} - \mu \right) a_i \\ & + \frac{1}{2} U \sum_i a_i^* a_i^* a_i a_i - \sum_{ij} t_{ij}\, (a_i^* \psi_j + \psi_i^* a_j) + \sum_{ij} t_{ij} \psi_i^* \psi_j \Bigg]\,, \end{aligned} \tag{4.39}$$

and integrate over the original fields a_i^* and a_i. If we denote by $S^{(0)}[a^*, a]$ the action for $t_{ij} = 0$, we have explicitely that

$$\begin{aligned} & \exp\left(-S^{\text{eff}}[\psi^*, \psi]/\hbar \right) \equiv \exp\left(-\frac{1}{\hbar} \int_0^{\hbar\beta} d\tau \sum_{ij} t_{ij} \psi_i^* \psi_j \right) \\ & \times \int \mathcal{D}a^* \mathcal{D}a \exp\left\{ -S^{(0)}[a^*, a]/\hbar \right\} \\ & \times \exp\left[-\frac{1}{\hbar} \int_0^{\hbar\beta} d\tau \left(-\sum_{ij} t_{ij}\, (a_i^* \psi_j + \psi_i^* a_j) \right) \right]. \end{aligned} \tag{4.40}$$

We can now calculate S^{eff} perturbatively by Taylor expanding the exponent in the integrant of Eq. (4.40) and evaluating the various correlation functions of the field theory given by $S^{(0)}$. This yields for the quadratic

part of the effective action

$$
\begin{aligned}
&S^{(2)}[\psi^*,\psi] \\
&= -\frac{1}{2\hbar}\left\langle\left(\int_0^{\hbar\beta} d\tau \sum_{ij} t_{ij}\left(a_i^*\psi_j + \psi_i^* a_j\right)\right)^2\right\rangle_{S^{(0)}} + \int_0^{\hbar\beta} d\tau \sum_{ij} t_{ij}\psi_i^*\psi_j \\
&= -\frac{1}{2\hbar}\left\langle\int_0^{\hbar\beta}\int_0^{\hbar\beta} d\tau d\tau' \sum_{iji'j'} t_{ij}t_{i'j'}\left(a_i^*\psi_j + \psi_i^* a_j\right)\left(a_{i'}^*\psi_{j'} + \psi_{i'}^* a_{j'}\right)\right\rangle_{S^{(0)}} \\
&+ \int_0^{\hbar\beta} d\tau \sum_{ij} t_{ij}\psi_i^*\psi_j. \qquad (4.41)
\end{aligned}
$$

If we perform the multiplication in the first term in the right-hand side and use the information we have about the correlations in the unperturbed system, i.e.,

$$
\left\langle a_i^* a_j^*\right\rangle_{S^{(0)}} = \left\langle a_i a_j\right\rangle_{S^{(0)}} = 0,\ \left\langle a_i^* a_j\right\rangle_{S^{(0)}} = \left\langle a_i a_j^*\right\rangle_{S^{(0)}} = \left\langle a_i a_i^*\right\rangle_{S^{(0)}}\delta_{i,j}, \qquad (4.42)
$$

we obtain in first instance

$$
\begin{aligned}
S^{(2)}[\psi^*,\psi] = \int_0^{\hbar\beta} d\tau \Bigg\{ &\sum_{ij} t_{ij}\psi_i^*(\tau)\psi_j(\tau) \qquad (4.43) \\
&- \frac{1}{\hbar}\int_0^{\hbar\beta} d\tau' \sum_{iji'j'} t_{ij}t_{i'j'}\psi_j^*(\tau)\left\langle a_i(\tau)a_{i'}^*(\tau')\right\rangle_{S^{(0)}}\psi_{j'}(\tau')\Bigg\},
\end{aligned}
$$

where we have now shown the τ dependence of the fields explicitely for clarity reasons. Because we will only consider nearest-neighbour hopping, we write

$$
t_{ij} = t_{ji} = \begin{cases} t & \text{for nearest neighbours} \\ 0 & \text{otherwise.} \end{cases} \qquad (4.44)
$$

First we treat the part of Eq. (4.43) that is linear in t_{ij}. We have

$$
\sum_{ij} t_{ij}\psi_i^*(\tau)\psi_j(\tau) = \sum_i t\psi_i^*(\tau)\psi_{i\pm\{1\}}(\tau), \qquad (4.45)
$$

where $\pm\{1\}$ denotes all possible jumps to nearest neighbours. In the case of one dimension this would simply be ± 1. If we call the lattice spacing

a and introduce Cartesian momentum components k_i with $i = 1, \cdots, d$, where d is again the number of dimensions, we find

$$\sum_{ij} t_{ij}\psi_i^*(\tau)\psi_j(\tau) = \sum_{\mathbf{k}} 2t\psi_{\mathbf{k}}(\tau)\psi_{\mathbf{k}}^*(\tau)\sum_{j=1}^{d}\cos(k_j a). \tag{4.46}$$

Next we calculate the part that is quadratic in t_{ij}. We can treat this part by looking at double jumps. The expectation value of $\langle a_i a_{i'}^* \rangle_{S^{(0)}}$ is proportional $\delta_{i,i'}$ and independent of the site i, according to Eq. (4.42). This means that we find, with similar notation as before,

$$\begin{aligned}
&\sum_{ji'j'} t_{ij}t_{i'j'}\psi_j^*(\tau)\left\langle a_i(\tau)a_{i'}^*(\tau')\right\rangle_{S^{(0)}}\psi_{j'}(\tau') \\
&= \left\langle a_i(\tau)a_i^*(\tau')\right\rangle_{S^{(0)}}\sum_{jj'} t_{ij}t_{ij'}\psi_j^*(\tau)\psi_{j'}(\tau') \\
&= t^2\left\langle a_i(\tau)a_i^*(\tau')\right\rangle_{S^{(0)}}\sum_{j}\Big\{z\psi_j^*(\tau)\psi_j(\tau') \\
&+ \psi_j^*(\tau)\psi_{j\pm\{2\}}(\tau') + \psi_j^*(\tau)\psi_{j\pm\{\sqrt{2}\}}(\tau')\Big\},
\end{aligned} \tag{4.47}$$

with z again the number of nearest neighbours. The first term in the summant is a jump in each direction, followed by a jump back. The second term indicates two jumps in the same direction and the third term is a jump in each direction followed by a jump in a perpendicular direction. Note that the third term is absent in one dimension. It can be shown that the complete double-jump term reduces to

$$\begin{aligned}
&\sum_{ji'j'} t_{ij}t_{i'j'}\psi_j^*(\tau)\left\langle a_i(\tau)a_{i'}^*(\tau')\right\rangle_{S^{(0)}}\psi_{j'}(\tau') \\
&= \left\langle a_i(\tau)a_i^*(\tau')\right\rangle_{S^{(0)}}\sum_{\mathbf{k}}\psi_{\mathbf{k}}^*(\tau)\psi_{\mathbf{k}}(\tau')(\epsilon_{\mathbf{k}})^2,
\end{aligned} \tag{4.48}$$

where we again used $\epsilon_{\mathbf{k}} = -2t\sum_{j=1}^{d}\cos(k_j a)$. To also treat the time dependence of the fields, we introduce Matsubara frequencies $\hbar\omega_n = \pi(2n)/\hbar\beta$ by

$$\psi_{\mathbf{k}}(\tau) = \sum_n \frac{1}{\sqrt{\hbar\beta}}\psi_{\mathbf{k}n}e^{-i\omega_n\tau},\ \psi_{\mathbf{k}}^*(\tau) = \sum_n \frac{1}{\sqrt{\hbar\beta}}\psi_{\mathbf{k}n}^*e^{+i\omega_n\tau}. \tag{4.49}$$

To translate the expectation value of the fields into the expectation value of operators, we introduce an (imaginary) time-ordering operator T. As a result

$$\left\langle a_i(\tau)a_{i'}^*(\tau')\right\rangle_{S^{(0)}} = \left\langle \mathrm{T}\left[a_i(\tau)a_{i'}^\dagger(\tau')\right]\right\rangle_{S^{(0)}}. \tag{4.50}$$

The time ordering can easily be expressed in Heavyside functions as

$$\begin{aligned}\left\langle \mathrm{T}\left[a_i(\tau)a_{i'}^\dagger(\tau')\right]\right\rangle_{S^{(0)}} &= \theta(\tau-\tau')\left\langle a_i(\tau)a_{i'}^\dagger(\tau')\right\rangle_{S^{(0)}} \\ &\quad + \theta(\tau'-\tau)\left\langle a_{i'}^\dagger(\tau')a_i(\tau)\right\rangle_{S^{(0)}}.\end{aligned} \tag{4.51}$$

If we use the unperturbed energies as given by (4.26), we thus find

$$\begin{aligned}\left\langle a_i(\tau)a_{i'}^*(\tau')\right\rangle_{S^{(0)}} &= \theta(\tau-\tau')(1+N_0)\exp\left\{-\left(E_{N_0+1}^{(0)}-E_{N_0}^{(0)}\right)(\tau-\tau')/\hbar\right\} \\ &\quad + \theta(\tau'-\tau)N_0\exp\left\{\left(E_{N_0-1}^{(0)}-E_{N_0}^{(0)}\right)(\tau-\tau')/\hbar\right\}.\end{aligned} \tag{4.52}$$

Because N_0 minimizes $E_{N_0}^{(0)}$ we know that

$$\begin{aligned}E_{N_0+1}^{(0)}-E_{N_0}^{(0)} &= -\mu+N_0U>0, \\ E_{N_0}^{(0)}-E_{N_0-1}^{(0)} &= -\mu+(N_0-1)U<0.\end{aligned} \tag{4.53}$$

Note that we use parameters μ and U instead of $\bar{\mu}$ and $\bar{U}$, because we have not yet divided out the factor zt. Combining the above with Eq. (4.43) we find

$$\begin{aligned}S^{(2)}[\psi^*,\psi] = &-\sum_n\sum_{\mathbf{k}}|\psi_{\mathbf{k}n}|^2\epsilon_{\mathbf{k}} \\ &\times\left(1+\frac{\epsilon_{\mathbf{k}}}{\hbar}\int_{-\infty}^0 d\tau'(1+N_0)\exp\left\{\left(-i\hbar\omega_n-\mu+N_0U\right)\tau'/\hbar\right\}\right. \\ &\left.+\frac{\epsilon_{\mathbf{k}}}{\hbar}\int_0^\infty d\tau' N_0\exp\left\{-\left(i\hbar\omega_n+\mu-(N_0-1)U\right)\tau'/\hbar\right\}\right).\end{aligned} \tag{4.54}$$

Performing the τ' integration we then easily obtain

$$\begin{aligned}S^{(2)}[\psi^*,\psi] = &-\sum_n\sum_{\mathbf{k}}|\psi_{\mathbf{k}n}|^2\epsilon_{\mathbf{k}} \\ &\times\left[1+\epsilon_{\mathbf{k}}\left(\frac{N_0+1}{-i\hbar\omega_n-\mu+N_0U}+\frac{N_0}{i\hbar\omega_n+\mu-(N_0-1)U}\right)\right].\end{aligned} \tag{4.55}$$

Note that this result is exact within our mean-field theory. It contains all powers of the frequencies and momenta and no gradient expansion has been applied. This is important because the elementary excitation are gapped as we will show in the next section.

We can find an equation for real energies $\hbar\omega$ by subtituting $i\omega_n \to \omega$ and equating the remaining factor to zero. This gives

$$0 = \left[1 + \epsilon_{\mathbf{k}} \left(\frac{N_0 + 1}{-\hbar\omega - \mu + N_0 U} + \frac{N_0}{\hbar\omega + \mu - (N_0 - 1)U} \right) \right]. \tag{4.56}$$

Ultimately this yields the result Eq. (4.57) given below in subsection 4.4.2.

4.4.2 Results

Now we will explore the results of the calculation presented in the previous subsection. The quasiparticle and quasihole dispersions are given by[6]

$$\epsilon_{\mathbf{k}}^{\mathrm{qp,qh}} = -\mu + \frac{U}{2}(2N_0 - 1) + \frac{\epsilon_{\mathbf{k}}}{2} \pm \frac{1}{2}\sqrt{\epsilon_{\mathbf{k}}^2 + (4N_0 + 2)U\epsilon_{\mathbf{k}} + U^2}. \tag{4.57}$$

In Fig. 4.6(a) we show for $\mathbf{k} = 0$ a plot of the above equations. The dotted lines indicate the asymptotes of Eq. (4.57), which are given by

$$\begin{aligned} \lim_{U\to\infty} \epsilon_{\mathbf{0}}^{\mathrm{qp}} &= -\mu + N_0 U + (N_0 + 1)\epsilon_{\mathbf{0}} = E_{N_0+1}^{(0)} - E_{N_0}^{(0)} - (N_0 + 1)zt, \\ \lim_{U\to\infty} \epsilon_{\mathbf{0}}^{\mathrm{qh}} &= -\mu + (N_0 - 1)U - N_0\epsilon_{\mathbf{0}} = E_{N_0}^{(0)} - E_{N_0-1}^{(0)} + N_0 zt, \end{aligned} \tag{4.58}$$

with $E_{N_0+1}^{(0)} - E_{N_0}^{(0)}$ and $E_{N_0}^{(0)} - E_{N_0-1}^{(0)}$ given by Eq. (4.53). The difference between Eq. (4.58) and Eq. (4.53) is caused by the fact that Eq. (4.53) is calculated for $t = 0$. It can easily be understood that for $t \neq 0$, the first-order correction is due to the hopping terms $a_j^\dagger a_i t$, where site j is one of the nearest neighbours of site i. When we have N_0 particles in all lattice sites and we add one particle to site i, we have $\langle a_j^\dagger a_i \rangle = N_0 + 1$, so the effective hopping parameter for a particle is $(N_0 + 1)t$. However, when we remove a particle from site i, we have $\langle a_i^\dagger a_j \rangle = N_0$, which represents a particle hopping to site i from one of its nearest neighbours. The effective hopping parameter for a hole is therefore only $N_0 t$. In combination, we see that in the limit of $U \to \infty$, Eq. (4.57) indeed reduces to a physically intuitive result.

[6] The dispersion $\epsilon_{\mathbf{k}}^{\mathrm{qp,qh}}$ was denoted $\hbar\omega_{\mathrm{qp,qh}}$ in the original publication.

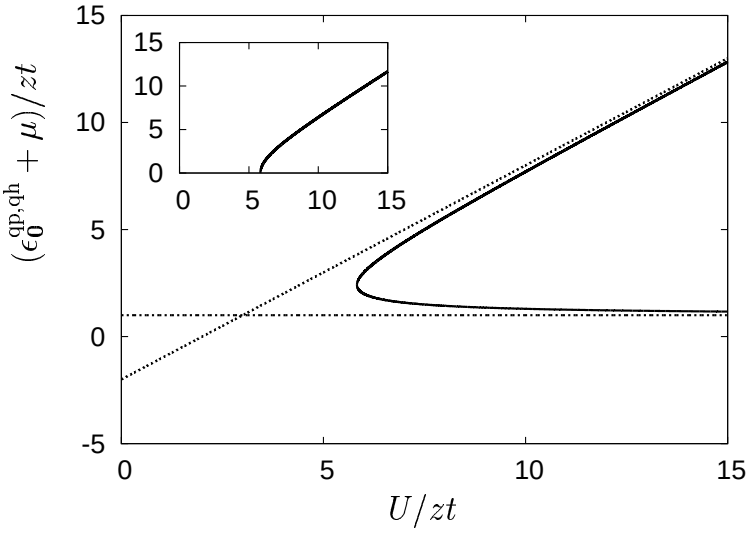

Figure 4.6: The quasiparticle and the quasihole energy for $\mathbf{k} = 0$ in the $N_0 = 1$ insulator lobe. The dotted lines are the asymptotes of the curves. The inset shows the resulting first-order approximation to the dispersion of the density fluctuations.

As shown above, the slopes of the asymptotes differ exactly by U, so in the limit of $U/zt \to \infty$ the gap for the creation of a quasiparticle-quasihole pair is equal to U. We can find a first approximation for the dispersion of the density fluctuations by substracting the two solutions, which yields[7]

$$\hbar\omega_{\mathbf{k}} = \epsilon_{\mathbf{k}}^{\mathrm{qp}} - \epsilon_{\mathbf{k}}^{\mathrm{qh}} = \sqrt{\epsilon_{\mathbf{k}}^2 + (4N_0 + 2)U\epsilon_{\mathbf{k}} + U^2}. \tag{4.59}$$

In Fig. 4.6(b) we show again for $\mathbf{k} = 0$ a plot of the above equation as a function of $\bar{U} = U/zt$ for $N_0 = 1$. We can see that there is a band gap, which proves that the MI phase is indeed an insulator and we also see that the band gap disappears as we approach the critical value $\bar{U}_c = U_c/zt \approx 5.83$ that was found earlier. For smaller values of $\bar{U}$ we are in the superfluid phase, which according to the Hugenholtz-Pines theorem is expected to always have gapless density fluctuations.

[7]The quantity $\hbar\omega_{\mathbf{k}}$ was denoted $\epsilon_{\mathbf{k}}$ in the original publication

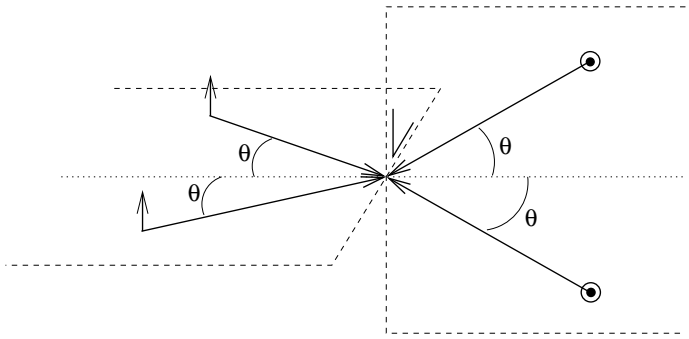

Figure 4.7: Laser beam configuration for a three-dimensional optical lattice.

4.5 Microscopic parameters

To estimate the experimental feasibility of observing the described phase transition, we now relate the parameters t and U to the microscopic parameters. Because we have an experimental interest in sodium, we will calculate these parameters for sodium atoms trapped in a lattice constructed with four laser beams. To calculate the hopping parameter t, we calculate the overlap between single-particle ground-state wave functions in neighboring sites. To calculate the interaction strength U, we use the pseudopotential method.

First we calculate the optical potential experienced by the atoms, following the approach of Petsas *et al.* [16]. We describe a $J = 1/2 \rightarrow J = 3/2$ transition and choose a laser-beam configuration with two pairs of laser beams. Each pair lies in a plane and the planes are perpendicular to each other. All beams have the same angle θ with respect to the intersection of the two planes. We choose the quantization axis along the intersection and label it as the z-axis. Furthermore, we choose the polarization of the laser beams linear and perpendicular to the plane spanned by the pairs of beams. The configuration is illustrated in Fig. 4.7. It should be noted that it is also possible to simply superimpose d standing waves to obtain a d dimensional lattice, but this requires stabilization of the relative phases of the laser beams. We define I_b as the sum of the intensity of the beams and if k is the

magnitude of the **k**-vector, we define $k_\perp = k\sin\theta$ and $k_\parallel = k\cos\theta$. If we add the electric field components and express them in spherical components

$$\begin{aligned} E_+ &= \frac{1}{\sqrt{2}}(E_x + iE_y), \\ E_- &= \frac{1}{\sqrt{2}}(E_x - iE_y), \\ E_0 &= E_z, \end{aligned} \tag{4.60}$$

we find that the spatial dependence of the intensity of the resulting light field is given by

$$\begin{aligned} I_\pm/I_b &= \frac{1}{2}\left(\cos^2(k_\perp x) + \cos^2(k_\perp y) \pm 2\cos(k_\perp x)\cos(k_\perp y)\cos(2k_{//}z)\right), \\ I_0/I_b &= 0. \end{aligned} \tag{4.61}$$

Note that at the minima of $I_\pm$ the polarization is purely $\sigma^\pm$. Also note that since the linear component is always zero, the two ground-state levels are not coupled.

Following Nienhuis *et al.* [37] we can now calculated the optical potential. Because of the fact that the ground-states are not coupled, we can treat them seperately. With δ the detuning, Γ the rate of spontaneous decay and $\Omega_\pm$ the Rabi frequencies for the $\sigma^\pm$ components of the light field, we can write the potential for the $m_j = \pm 1/2$ level in the limit of low saturation as:

$$V_\pm = \frac{1}{2}\frac{\hbar\delta}{1+4(\delta/\Gamma)^2}\left[\frac{2|\Omega_\pm|^2}{\Gamma^2} + \frac{1}{3}\frac{2|\Omega_\mp|^2}{\Gamma^2}\right], \tag{4.62}$$

where the factor 1/3 arises because of the Clebsch-Gordan coefficients for $J = 1/2 \rightarrow J = 3/2$ transitions.

Now we define a convenient prefactor:

$$V_b = \frac{1}{2}\frac{\hbar\delta s_0}{1+4(\delta/\Gamma)^2} = \frac{\hbar\delta s}{2}, \tag{4.63}$$

where $s = s_0/\left(1+4(\delta/\Gamma)^2\right)$ is the off-resonance saturation parameter and $s_0 = 2|\Omega|^2/\Gamma^2$ is the on-resonance saturation parameter, which is usually written as $s_0 = I/I_s$. The saturation intensity I_s is a constant for a given

transition. If we substitute Eq. (4.63) in Eq. (4.62), we find

$$\begin{aligned} V_{\pm} &= V_b \left(\frac{I_{\pm}}{I_b} + \frac{1}{3} \frac{I_{\mp}}{I_b} \right) \\ &= \frac{2}{3} V_b \left(\cos^2 (k_{\perp} x) + \cos^2 (k_{\perp} y) \pm \cos (k_{\perp} x) \cos (k_{\perp} y) \cos (2k_{//} z) \right). \end{aligned} \tag{4.64}$$

We now write the Hamiltonian of a particle in the potential as:

$$H_{\text{opt}} = \frac{p^2}{2m} + V_{\pm}, \tag{4.65}$$

and solve the time-independent Schrödinger equation variationally by assuming an isotropic Gaussian wave function and minimizing the energy as a function of width of the Gaussian. If we call l the width of the wave function, we can write the normalized wave function as

$$\Psi(\mathbf{r}) = \langle \mathbf{r} | \Psi \rangle = \left(\frac{1}{\pi l^2} \right)^{3/4} e^{-|\mathbf{r}|^2 / 2l^2}. \tag{4.66}$$

We assume we have a spin polarized sample of atoms, so we can use either the V_+ or the V_- potential.

For simplicity we now calculate the parameters for a one-dimensional lattice. For the lattice configuration in Fig. 4.7 this gives approximate results, but for a phase-stabilized superposition of three standing waves, the results are immediately applicable. In this case, the potential reduces to $V_{\pm} = 2V_b[2 \pm \cos(2kz)]/3 + \kappa_{\perp}(x^2+y^2)/2$, where the transverse potential is caused by the fact that the laser beam has a finite width. If we assume the wave function is tightly localized in the center of the local potential well, we can approximate the potential as an harmonic potential $V_+ = 2V_b + \kappa \mathbf{r}^2/2$ with $\kappa = -8V_b k^2/3$, where we assume we can adjust the width of the laser such that $\kappa_{\perp} \approx \kappa$. These approximations yield the well-known equations for the width and the level splitting in the potential

$$l = \left(\frac{\hbar^2}{m\kappa} \right)^{1/4}, \; \omega = \sqrt{\kappa/m}. \tag{4.67}$$

Using the above width[8] l we calculate the value of the interaction strength U with the pseudopotential method. According to [38] this is valid for

[8] The length l was denoted β in the original publication.

sodium even if the width of the trapping volume is of the order of the scattering length. In general the interaction strength between two atoms in the same one particle wave function is given by

$$U = \int d\mathbf{r} \int d\mathbf{r}' \Psi^*(\mathbf{r})\Psi^*(\mathbf{r}')V_{\rm int}(\mathbf{r}-\mathbf{r}')\Psi(\mathbf{r})\Psi(\mathbf{r}'), \tag{4.68}$$

where $V_{\rm int}(\mathbf{r}-\mathbf{r}')$ is the interaction potential. If we approximate the potential as

$$V_{\rm int}(\mathbf{r}-\mathbf{r}') = \frac{4\pi a_s \hbar^2}{m}\delta(\mathbf{r}-\mathbf{r}'), \tag{4.69}$$

we can write Eq. (4.68) as:

$$\begin{aligned} U &= \frac{4\pi a_s \hbar^2}{m}\int d\mathbf{r}\Psi^*(\mathbf{r})\Psi^*(\mathbf{r})\Psi(\mathbf{r})\Psi(\mathbf{r}) \\ &= \frac{4\pi a_s \hbar^2}{m}\int d\mathbf{r}|\Psi(\mathbf{r})|^4 = \frac{4\pi a_s \hbar^2}{m l^3 \pi^{3/2}} = \frac{2\hbar\omega}{\sqrt{2\pi}}\left(\frac{a_s}{l}\right), \end{aligned} \tag{4.70}$$

where a_s is the triplet s-wave scattering length. According to [39] the value of the scattering length for a spin-polarized sodium-sodium collision is $a_s = (85 \pm 3)a_0$. Note that the use of a one-band model is justified when $U \ll \hbar\omega$, or $l \gg 2a_s/(2\pi)^{1/2} \approx 3.5$nm.

Next we calculate the value of the hopping parameter t. In the tight-binding limit t is given by

$$t = -\int d\mathbf{r}\Psi^*(\mathbf{r})\left(\frac{p^2}{2m} + V_\pm\right)\Psi(\mathbf{r}+a\mathbf{e}_j), \tag{4.71}$$

where $\mathbf{e_j}$ is an axis vector along a lattice direction, so that when $\Psi(\mathbf{r})$ is the ground-state wave function, $\Psi(\mathbf{r}+a\mathbf{e}_j)$ is the ground-state wave function of an atom at a neighboring site. One can show that product of two wave functions at neighbouring sites is a Gaussian function centered around $\mathbf{r} + a\hat{e}_j/2$. We can therefore approximate the potential around the maximum of the barrier by $V_\pm = 2V_b/3 \mp \kappa\mathbf{r}^2/2$. Substituting this into Eq. (4.71) ultimately yields

$$t = \frac{\hbar\omega}{8}\left[1 - \left(\frac{2}{\pi}\right)^2\right]\left(\frac{a}{l}\right)^2 e^{-\frac{1}{4}(a/l)^2} \tag{4.72}$$

Figs. 4.8(a) and (b) show plots of $U/E_{\rm R}$ and $t/E_{\rm R}$ respectively, with $E_{\rm R} = \hbar^2k^2/2m$ the recoil energy. Both are plotted as a function of the trap depth

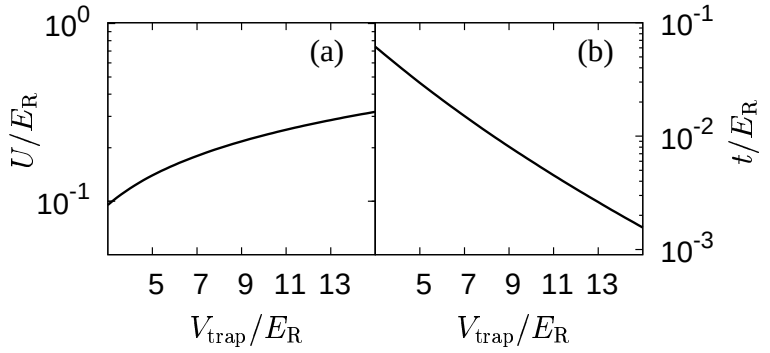

Figure 4.8: Plot of (a) U and (b) t as a function of the trap depth. All quantities are in units of the recoil energy E_R.

$V_{trap} = -4V_b/3$. The values were calculated for a laser wave length of 600 nm. The saturation parameter needed to reach these trap depths is in the order of 10^5, which is not unrealistic experimentally.
Fig. 4.9 shows also U/zt as a function of the trap depth, for a wave length of 600 nm, in one, two and three dimensions. Again, the saturation parameter is in the order of 10^5. As can been seen, the desired critical value is reached in all three dimensions. The value of the width l lies between 12% and 8% of the wave length in the range considered in the above plots. This implies that both the harmonic approximation and the use of the one-band model are justified.

4.6 Conclusion

Due to the absence of the superfluid-insulator phase transition in the Bogoliubov approach, we conclude that the interaction is the dominant component in this phase transition. When the interaction energy is treated exactly, the theory indeed predicts a phase transition. The mean-field theory predicts a phase transition even in one dimension, which we expect to survive as a Kosterlitz-Thouless transition when fluctuations are incorperated. However a definite prove of this requires further study.

We analytically calculated the phase diagram and the particle and hole dispersion relations in the insulator phase. A first-order approximation to the dispersion of the density fluctuations shows that the system indeed goes from a gapped to a gapless phase. A calculation of this dispersion below the

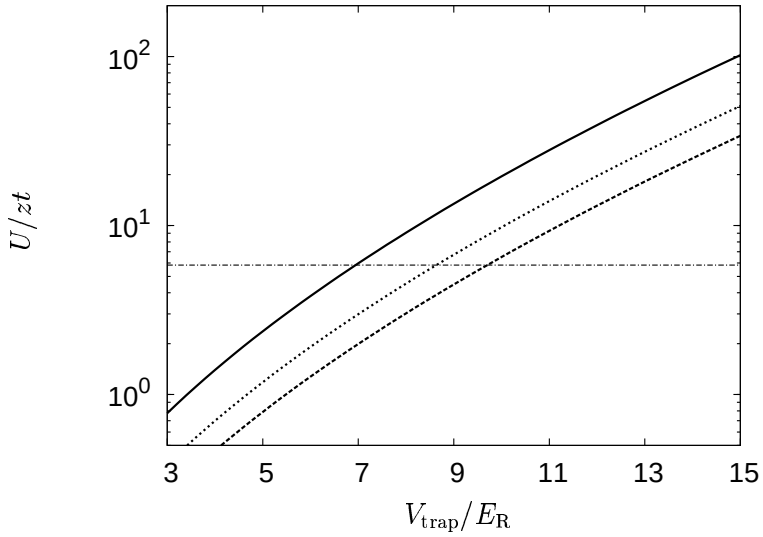

Figure 4.9: The dimensionless parameter U/zt plotted as a function of the trap depth for 1 (solid line), 2 (dotted line) and 3 dimensions (dashed line). The dash-dotted line is the critical value $\bar{U} = 5.83$.

critical value for U/zt will have to be done in order to check the presence of linear dispersion that would verify the assumption that the phase with $\psi \neq 0$ is indeed superfluid. The one-band model we used to calculate the parameters for sodium gives optimistic results for future experiments, within the range of parameters it allows.

4.A The perturbation series

A powerful approach to calculating higher-order terms in the perturbation series is derived in [40]. Here we only give the result of that derivation. If we denote by $|n\rangle$ the unperturbed wave functions and $E_n^{(0)}$ the unperturbed energies, we can define an operator

$$S_a^k = \begin{cases} -|a\rangle\langle a| & \text{if } k = 0 \\ \sum_{n\neq a} \frac{|n\rangle\langle n|}{\left(E_a^{(0)} - E_n^{(0)}\right)^{k+1}} & \text{if } k > 0 \end{cases} , \tag{4.73}$$

and one can prove that the n-th order correction on the energy $E_a^{(0)}$ is given by

$$E_a^{(n)} = \mathrm{Tr}\left[\sum_{\{n-1\}} S_a^{k_0}\hat{V}...\hat{V}S_a^{k_n}\right], \tag{4.74}$$

where $\{n\} = \{k_0, ..., k_n | k_0 + ... + k_n = n\}$. In the case of $n = 2$, this quickly gives the well-known result

$$\begin{aligned} E_a^{(2)} &= \mathrm{Tr}\left[\sum_{\{1\}} S_a^{k_0}\hat{V}S_a^{k_1}\hat{V}S_a^{k_2}\right] = \langle a|\hat{V}S_a^1\hat{V}|a\rangle, \\ &= \sum_{n\neq a} \frac{\left|\langle n|\hat{V}|a\rangle\right|^2}{\left(E_a^{(0)} - E_n^{(0)}\right)}. \end{aligned} \tag{4.75}$$

The same can be done for $E_a^{(1)}$, $E_a^{(3)}$ and $E_a^{(4)}$. The first two can be shown to involve only terms proportional to odd orders of V and with $V \propto (a^\dagger + a)$ these are of course zero. The fourth-order term is in general given by

$$\begin{aligned} E_a^{(4)} &= \mathrm{Tr}\left[\sum_{\{3\}} S_a^{k_0}\hat{V}S_a^{k_1}\hat{V}S_a^{k_2}\hat{V}S_a^{k_3}\hat{V}S_a^{k_4}\right] \\ &= \langle a|\hat{V}S_a^1\hat{V}S_a^1\hat{V}S_a^1\hat{V}|a\rangle - \langle a|\hat{V}S_a^1\hat{V}|a\rangle\langle a|\hat{V}S_a^2\hat{V}|a\rangle \\ &- 2\langle a|\hat{V}|a\rangle\langle a|\hat{V}S_a^1\hat{V}S_a^2\hat{V}|a\rangle + \langle a|\hat{V}|a\rangle^2\langle a|\hat{V}S_a^3\hat{V}|a\rangle. \end{aligned} \tag{4.76}$$

If we drop the terms containing expectation values of odd powers of V and substitute Eq. (4.73), we find

$$\begin{aligned} E_a^{(4)} &= \langle a|\hat{V}S_a^1\hat{V}S_a^1\hat{V}S_a^1\hat{V}|a\rangle - \langle a|\hat{V}S_a^1\hat{V}|a\rangle\langle a|\hat{V}S_a^2\hat{V}|a\rangle \\ &= \sum_{n,p,q\neq a} \langle a|\hat{V}|n\rangle \left(-E_a^{(2)} \frac{\langle n|\hat{V}|a\rangle}{\left(E_a^{(0)} - E_n^{(0)}\right)^2} \right. \\ &\left. + \frac{\langle n|\hat{V}|p\rangle}{\left(E_a^{(0)} - E_n^{(0)}\right)} \frac{\langle p|\hat{V}|q\rangle}{\left(E_a^{(0)} - E_p^{(0)}\right)} \frac{\langle q|\hat{V}|a\rangle}{\left(E_a^{(0)} - E_q^{(0)}\right)} \right), \end{aligned} \tag{4.77}$$

which we have used to derive Eq. (4.33).

Chapter 5

Mott insulators in an optical lattice with high filling factors

Abstract

We discuss the superfluid to Mott insulator transition of an atomic Bose gas in an optical lattice with high filling factors. We show that in this multi-band situation, the long-wavelength physics is described by a single-band Bose-Hubbard model. We determine the many-body renormalization of the tunneling and interaction parameters in the effective Bose-Hubbard Hamiltonian, and consider the resulting model at nonzero temperatures. We show that in particular for a one or two-dimensional optical lattice, the Mott-insulator phase is more difficult to realize than anticipated previously.

5.1 Introduction

The behaviour of trapped Bose-Einstein condensates offers a large amount of interesting features. Specifically, the phase coherence of a condensate creates the prospect of various interference experiments, as shown for the

This chapter has been previously published as *Mott insulators in an optical lattice with high filling factors*, D. van Oosten, P. van der Straten, and H. T. C. Stoof, Phys. Rev. A **67**, 033606 (2003)

first time in an experiment performed by Andrews *et al.* [41]. In another experiment a large number of condensates trapped in a periodic lattice potential have been made to interfere [42]. Having shown experimentally that in general condensates are phase coherent and thus show off-diagonal long-range order, the question arises if this long-range order can also be destroyed in a controllable way. This was only very recently achieved in a beautiful experiment by Greiner *et al.* [15].

In this last experiment, a trapped Bose-Einstein condensate is put into a three-dimensional optical lattice. The number of atoms in the condensate is sufficiently large to obtain a filling factor of almost two atoms per site. By increasing the intensity of the lattice light, a quantum phase transition from a superfluid state to a Mott-insulating state is achieved. In the insulating phase all phase coherence is lost due to quantum fluctuations. The transition was predicted to occur in this system by Jaksch *et al.* [9], and the observed critical conditions for the transition are in good agreement with the results of an on-site mean-field theory [43]. This indicates that the single-band Bose-Hubbard model used in Refs. [9, 43] can accurately describe a gas of ultracold bosonic atoms in an optical lattice when the filling factor of the lattice is of the order of one.

However, this model is no longer valid in the case of higher filling factors such as described in the experiments of [7, 44]. The theories mentioned above use single-particle wave functions corresponding to the lowest band of the lattice to calculate the microscopic parameters of the single-band Bose-Hubbard model as a function of the lattice parameters. In the case of high filling factors more than one band is generally populated, leading to a multi-band Bose-Hubbard model. The interaction effects that occur under these circumstances have not been considered previously. Furthermore, the effects of thermal fluctuations are also not understood, even in the single-band Bose-Hubbard model. There are studies that describe number squeezing in an optical lattice at nonzero temperature [45, 46], but they are not in the strongly-interacting limit that is relevant for the Mott insulator. Our main objective here is to develop an effective theory that can deal with these issues.

5.2 Solving the multi-band Bose-Hubbard model

To solve the problems associated with high filling factors, we have to deal with the many-body physics at every site. Since the high filling factors of interest are experimentally most relevant in low-dimensional lattices [7, 44], we discuss the energy scales involved in those systems. In a low-dimensional lattice, we can approximate the on-site trapping potential by an anisotropic harmonic potential. The oscillator frequencies $\omega_{\parallel}$ and $\omega_{\perp}$ correspond to the trapping frequencies in the directions parallel and perpendicular to the periodicity of the lattice, respectively. Because the typical size of a lattice well in the parallel direction(s) is much smaller than in the perpendicular direction(s), we immediately have that $\hbar\omega_{\perp} \ll \hbar\omega_{\parallel}$. Furthermore, for the experimental conditions of interest [7, 44], the temperature is in between the two trapping frequencies, *i.e.*, $\hbar\omega_{\perp} \ll k_B T \ll \hbar\omega_{\parallel}$. This implies that in every site the gas is in the parallel direction(s) in the ground state of the potential, but that it occupies many states in the perpendicular direction(s). In particular, this holds for the thermal cloud of the gas. As a consequence, the effective dimensionality of the gas at every site is reduced and the thermal excitations are only present in the perpendicular direction(s). It is under these conditions that we are able to solve the relevant multi-band Bose-Hubbard model by using the following two-step procedure.

First, we solve the many-body physics at every site. Due to the famous infrared problems of a one or two-dimensional Bose gas this is not an easy task, and an accurate equation of state for these gases was developed only very recently in the weakly-interacting limit [47]. This equation of state is found by treating phase fluctuations in the (quasi)condensate exactly and we can in particular use it to determine at every temperature the number of atoms in the (quasi)condensate $N_0(T)$. Furthermore, it is shown in Ref. [47] that even in the presence of phase fluctuations, the Gross-Pitaevskii equation can still be used to calculate the density profile of the (quasi)condensate.

Secondly, we consider the coupling between the sites. Since we have a (quasi)condensate at every site, the coupling between sites will be dominated by tunneling from (quasi)condensate to (quasi)condensate as opposed to (quasi)condensate to thermal cloud. This means that we can describe the coupling between sites by a single-band Bose-Hubbard model. The important parameters in the Bose-Hubbard model are the on-site interaction energy U and the energy t associated with the tunneling of atoms between

nearest-neighbor sites. Both energies can be calculated from the knowledge of the (quasi)condensate wave function $\psi_0(\mathbf{x}) = \sqrt{n_0(\mathbf{x})}e^{i\vartheta}$, where $n_0(\mathbf{x})$ is the density profile and ϑ is the global phase of the (quasi)condensate. The interaction energy U is proportional to $\int d\mathbf{x}|\psi_0(\mathbf{x})|^4$, whereas the tunneling energy t requires the evaluation of an overlap integral between the (quasi)condensate wave functions of two neighboring sites in the parallel direction(s).

To describe the effect of the interatomic interaction, we thus need to determine how the (quasi)condensate wave function changes as a result of the on-site interactions. Since the mean-field interaction obeys $\hbar\omega_\perp \ll N_0 U \ll \hbar\omega_\parallel$ under the experimental conditions of interest, we can write the three-dimensional wave function of the condensate as a product of a single-particle ground-state wave function in the parallel direction(s) and the (quasi)condensate wave function in the perpendicular direction(s). If we substitute this product wave function into the Gross-Pitaevskii equation and integrate out the parallel direction(s), we arrive at an effective equation for the (quasi)condensate wave function. Because of the above mentioned inequality, we can subsequently solve this equation using the Thomas-Fermi or local-density approximation [48]. To quantify the differences between the (quasi)condensate wave function and the single-particle ground-state wave function, we define a dimensionless coupling constant g both in the noninteracting and in the interacting case. The first parameter we call the bare coupling constant $g_{\mathrm{B}} = U_{\mathrm{B}}/t_{\mathrm{B}}$ and it is calculated with the single-particle ground-state wave function in every site. The second parameter we call the renormalized coupling constant $g_{\mathrm{R}} = U_{\mathrm{R}}/t_{\mathrm{R}}$ and it is calculated using the single-particle ground state in the parallel direction(s) and a Thomas-Fermi density profile in the perpendicular direction(s). Because we have already included the on-site interaction effects in this coupling constant, we can now write down a renormalized single-band Bose-Hubbard model for the total optical lattice, where the creation and annihilation operators $a_i^\dagger$, and a_i, respectively, and the number operator n_i are not associated with the Wannier states of atoms in the lattice, but with the macroscopic wave function of the (quasi)condensate in each site. In particular, we have

$$H = -t_{\mathrm{R}} \sum_{\langle i,j \rangle} a_i^\dagger a_j + \frac{U_{\mathrm{R}}}{2} \sum_i n_i \left(n_i - 1\right) - \mu_{\mathrm{R}} \sum_i n_i, \tag{5.1}$$

where μ_{R} is the effective chemical potential. The interaction parameter

is given by $U_{\rm R} = \partial^2 F^{\rm os}/\partial N^2\big|_{N=N_0} \equiv \partial\mu^{\rm os}/\partial N|_{N=N_0}$, where $F^{\rm os}$ is the on-site free energy and $\mu^{\rm os}$ is the on-site chemical potential. Formally, the effective chemical potential is given by $\mu_{\rm R} = \mu - \mu^{\rm os} - U_{\rm R}/2$, where the last term is substracted from the interaction energy to make the analogy to the single-band Bose-Hubbard model of Refs. [9, 43] complete.

It is important to understand that the hopping term only describes hopping between the (quasi)condensates in neighbouring sites. While it is clear that this is a very good approximation in the case of neighbouring condensates, it may not be immediately obvious in the case of neighbouring quasicondensates. However, it should be noted that the effect of the hopping is only large when the system is in the superfluid phase, in which case all the sites couple to form a true three-dimensional condensate. The tunneling strength can be calculated in the tight-binding limit and depends only on the overlap in the parallel direction(s). As a result the bare and renormalized values of t are equal. However, the interaction energy is strongly reduced due to the repulsive on-site interactions which spread-out the (quasi)condensate wave function considerably. We find for a two-dimensional gas that

$$g_{\rm R} = g_{\rm B}\left(\frac{\pi}{2}\right)^{1/4}\left(\frac{\ell_\parallel}{N_0 a}\right)^{1/2} \propto g_{\rm B}\left(\frac{\ell_\perp}{R_{\rm TF}}\right)^2, \tag{5.2}$$

and for a one-dimensional gas that

$$g_{\rm R} = g_{\rm B}\left(\frac{\pi}{2}\right)^{1/2}\left(\frac{\ell_\parallel^2}{3N_0 a \ell_\perp}\right)^{1/3} \propto g_{\rm B}\left(\frac{\ell_\perp}{R_{\rm TF}}\right). \tag{5.3}$$

Here a is the positive s-wave scattering length of the atoms, $\ell_\parallel = \sqrt{\hbar/m\omega_\parallel}$ and $\ell_\perp = \sqrt{\hbar/m\omega_\perp}$ are the harmonic oscillator lengths in the parallel and perpendicular directions, respectively, and $R_{\rm TF}$ is the Thomas-Fermi radius of the (quasi)condensate. The physical interpretation of Eqs. (5.2) and (5.3) is that as a result of the repulsive interatomic interactions, the (quasi)condensate reduces its total energy by increasing its size in the perpendicular direction(s). This can be seen from the fact that the decrease of the coupling constant is inversely proportional to the increase in the surface or length of the two or one-dimensional gas, respectively. Note that this reduction is particularly important for the critical conditions, which can be written as $g_{\rm R} > 4zN_0$ for large N_0 [43]. In order to verify the consistency of

our two-step approach, we explicitly check the relevant energy scales using our results of Eqs.(5.2) and (5.3). First, we assumed that the mean-field interaction energy $N_0 U_{\rm R}$ is much smaller than the trapping frequency in the parallel direction(s) $\hbar\omega_{\|}$. This requires that for a one-dimensional lattice

$$N_0 \ll \left(\frac{\hbar\omega_{\|}}{\hbar\omega_{\perp}}\right)^2 \sqrt{2\pi}\frac{\ell_{\|}}{a}. \tag{5.4}$$

Second, we also assumed that the crossover temperature for the formation of a (quasi)condensate in two dimensions is much lower than $\hbar\omega_{\|}$. This results in

$$\hbar\omega_{\perp}\left(\frac{N}{\zeta(2)}\right)^{1/2} \ll \hbar\omega_{\|}, \tag{5.5}$$

where N is the total number of atoms at every site. For typical numbers used in the experiments by Orzel *et al.* [7], we find the condition $N_0 \leq N \ll 10^5$, which means that our assumptions are valid for even the largest filling factor reported. For the case of the two-dimensional lattice of Greiner *et al.* [44], a similar inequality can be derived. It is found that this experiment is also in the regime where our assumptions are valid. Note that the use of the Thomas-Fermi approximation also imposes a lower limit on the filling factor, namely, $N_0 a \gg l_{\perp}$. However, when the filling factor is below this limit, we are in the regime where we can safely use the bare coupling constant. We thus conclude that depending on the filling factor, either our renormalized or the bare theory is applicable to these experiments.

5.3 Thermal effects

Besides the effect of thermal fluctuations on the number of (quasi)condensate atoms per site $N_0(T)$, which is accounted for by the equation of state of the low-dimensional Bose gas [47], there is also the effect of thermal fluctuations on the renormalized single-band Bose-Hubbard model itself. These thermal fluctuations are also present in a lattice with low filling factor. To study these thermal fluctuations, we use an on-site mean-field Hamiltonian that we can derive from Eq. (5.1), using the approach presented in Ref. [43]. We decouple the tunneling term, by introducing a complex mean

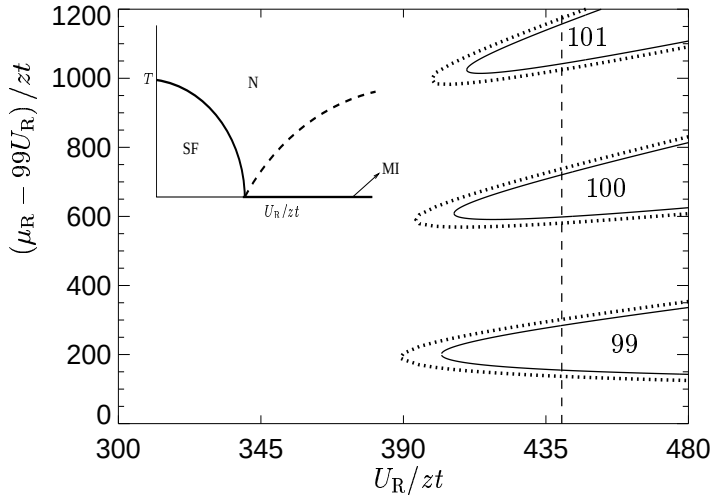

Figure 5.1: Phase diagram of the Bose-Hubbard model in terms of the chemical potential μ_R/zt and the coupling constant U_R/zt. The solid and dotted lines correspond to $T = 0$ and $T = 0.1U_c$ (where U_c is the critical U_R for the $N_0 = 100$ lobe), respectively. The inset shows a qualitative phase diagram in terms of the temperature T and the coupling constant g. N, SF and MI indicate the normal gas phase, the superfluid and the Mott-insulating phase, respectively.

field parameter ψ as follows $a_i^\dagger a_j = \psi a_j + a_i^\dagger \psi^* - |\psi|^2$. Physically, ψ is the superfluid order parameter which we choose to be real in the following. Performing the above substitution, we find

$$H(\psi) = -zt\psi(a^\dagger + a) + \frac{U_R}{2} n(n-1) - \mu_R n + zt\psi^2, \tag{5.6}$$

with z the coordination number. Since this is an on-site Hamiltonian, we have dropped the site indices for simplicity. Moreover, we assumed that the chemical potential is chosen such that the expectation value of the number operator n is equal to the number of quasi(condensate) particles $N_0(T)$ in every site.

The zero-temperature phase diagram of this mean-field theory can be solved exactly [43, 11] and is shown in Fig. 5.1, where the Mott-insulator

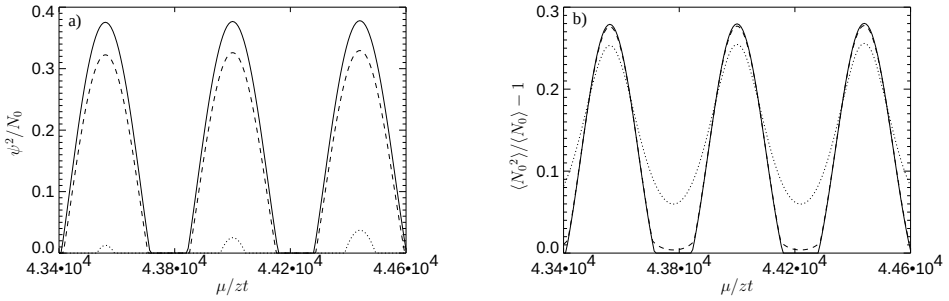

Figure 5.2: Condensate fraction (a) and particle number fluctuations (b) as a function of the coupling constant, for $k_BT = 0, 0.08U$ and $0.145U$ (solid, dashed and dotted lines respectively) . The coupling constant $U_{\rm R}/zt = 440$ (the dashed line in Fig 5.1).

phases correspond to the various lobes. For nonzero temperatures the model can no longer be solved analytically and we have to resort to numerical methods. If we put $\psi = 0$, we find that the eigenstates of Eq. (5.6) are given by number states. Using a basis consisting of these number states, running from a certain minimum filling factor $N_{\rm min}$ to a certain maximum $N_{\rm max}$, we can calculate the grand-canonical partition function $Z(\psi) = {\rm Tr}[e^{-H(\psi)/k_BT}]$ by diagonalizing the mean-field Hamiltonian given in Eq. (5.6). Next we determine the thermodynamic potential $\Omega(\psi) = -k_{\rm B}T \ln Z(\psi)$ as a function of the order parameter ψ. For zero temperature the calculation converges when $N_{\rm max} \simeq N_0 + 4$ and $N_{\rm min} \simeq N_0 - 4$, where N_0 is the filling factor of the relevant Mott-insulator lobe. For nonzero temperatures, more states must be included.

To obtain the relevant thermodynamic quantities, we minimize the grand potential $\Omega(\psi)$ and the value of ψ at the minimum of $\Omega(\psi)$ corresponds physically to the square root of the number of atoms that is superfluid in the direction(s) parallel to the periodicity of the lattice. In the Mott insulator the gas is only insulating in the direction(s) parallel to the periodicity of the optical lattice, whereas it is always a superfluid in the perpendicular direction(s). The other quantity of interest is the value of the number fluctuations. This number is important because in the Mott-insulator phase the number fluctuations are exactly zero.

The final results of the calculations are shown in Fig. 5.2. In these figures, the longitudional superfluid fraction and the number fluctuations are plotted along the dashed line in Fig. 5.1 for different temperatures. It can clearly be seen from Fig. 5.2(a) that the superfluid part of the phase diagram decreases with increasing temperature. In addition Fig. 5.2(b) shows that at zero temperature the density fluctuations drop exactly to zero in the Mott-insulating regions, but that this does not happen at nonzero temperature. This is a result of the fact that the superfluid to Mott-insulator transition is a quantum phase transition. The reason that there is still a reduction in particle-number fluctuations at nonzero temperature is that the excitation spectrum of a fluctuation is gapped in this region [43], which means that the fluctuations are exponentially suppressed. Due to this strong suppression of the number fluctuations, one will be able to observe a phase which is formally not a Mott insulator, but experimentally has very similar features. Another feature we can clearly see in Fig. 5.2(b) is that part of the phase diagram where the number fluctuations are suppressed also decreases with increasing temperature, and shrinks in the opposite direction of that of the superfluid part.

On the basis of the above calculations, we can draw the nonzero temperature phase diagram shown in Fig. 5.1. In this figure, the solid lines indicate the superfluid to Mott insulator transition at zero temperature and the dotted lines indicate the superfluid to normal transition at nonzero temperature. The inset shows the phase diagram in terms of the temperature and the coupling constant. This diagram agrees very well with the general description given by Sachdev [11].

5.4 Conclusion

We have shown that for low-dimensional lattices, which generally have a filling factor much larger than one, we should in principle solve a many-band Bose-Hubbard model. This can be achieved by first solving the on-site many-body problem, and then deriving an effective theory that describes the coupling between the sites in the optical lattice in terms of a renormalized single-band Hubbard model. We have calculated the effects of thermal excitations in this renormalized model and we have shown that the number fluctuations in the above model can only drop to zero in the absence of thermal fluctuations. However, if the temperature is sufficiently low, the

number fluctuations are exponentially suppressed. This means that at a certain nonzero temperature, the crossover to the Mott-insulator phase can still be observed if the coupling constant is increased to a value larger than the zero-temperature critical value (cf. Fig. 5.1). It is important to realize that to experimentally obtain the Mott insulator with a large filling factor N_0, the coupling constant $g_{\mathrm{R}} = U_{\mathrm{R}}/t$ must be larger than $4zN_0$. However, Eqs. (5.2) and (5.3) show that the renormalized coupling constant is much smaller than the bare coupling constant for a low-dimensional optical lattice. We therefore conclude that in terms of the bare coupling constant, which is the experimentally relevant control parameter, the Mott-insulator phase is much more difficult to obtain than is naively anticipated on the basis of a purely single-band Bose-Hubbard model.

Chapter 6

Inelastic light scattering from a Mott insulator

Abstract

We propose to use Bragg spectroscopy to measure the excitation spectrum of the Mott-insulator state of an atomic Bose gas in an optical lattice. We calculate the structure factor of the Mott insulator taking into account both the self-energy corrections of the atoms and the corresponding dressing of the atom-photon interaction. We determine the scattering rate of photons in the stimulated Raman transition and show that by measuring this scattering rate in an experiment, in particular the excitation gap of the Mott insulator can be determined.

6.1 Introduction

A Bose-Einstein condensate in an optical lattice is a powerful new tool to investigate strongly-correlated Bose gases [49, 50]. In particular, the experiment by Greiner *et al.* [15] has shown that it is possible to achieve a quantum phase transition from a superfluid to a Mott-insulating phase by starting from an atomic Bose-Einstein condensate and loading this system into an optical lattice. This phase transition was predicted to occur in

This chapter has been submitted for publication in Phys. Rev. Lett. as *Inelastic light scattering from a Mott insulator*, D. van Oosten, D. B. M. Dickerscheid, B. Farid, P. van der Straten, and H. T. C. Stoof.

the Bose-Hubbard model by Fisher *et al.* [10], and Jaksch *et al.* [9] were the first to make the crucial observation that the Bose-Hubbard model can be applied to bosonic atoms in an optical lattice. The mean-field phase diagram at zero temperature was calculated by several authors [28, 31, 32], however, the Bogoliubov-like theory for the excitations in both the superfluid and the Mott-insulator phases of the gas was developed more recently by van Oosten *et al.* [43]

An important advantage of using atoms in an optical lattice to study the Bose-Hubbard model, is that the system is free from disorder, which makes it possible to make very accurate predictions and measurements. A good example of such a high-precision measurement is Bragg spectroscopy. This technique has already been used to coherently split a Bose-Einstein condensate into two momentum components [51], to measure the excitation spectrum of a trapped Bose-Einstein condensate [52], and to measure the light-shifted energy levels of an atom in an optical lattice [53]. Here we propose to use Bragg spectroscopy to measure the excitation spectrum of the Mott-insulator state. In particular, one can in this way determine the value of the particle-hole gap in the excitation spectrum and study the behaviour of this gap as the system approaches the quantum critical point. Note that the excitation spectrum as obtained by using Bragg spectroscopy does not yield what is generally referred to as the Mott gap, because this gap is associated with single-particle excitations. The value of the particle-hole gap can be obtained though and is a particularly interesting quantity in the study of quantum critical phenomena. In addition, this gap is also very important for the practical application of these systems to quantum information processing, since the gap determines the fidelity of the Mott state. It is important to realize that the system of a Bose-Einstein condensate in an optical lattice is more complicated than the above-mentioned systems where Bragg spectroscopy has already been applied, because in this case many-body effects and strong correlations have to be taken into account.

In a Bragg-spectroscopy experiment, two laser beams are used to make excitations in the system, as shown in Fig. 6.1(a). The two lasers both have a large detuning with respect to an optical transition in the atoms so that spontaneous emission is suppressed. However, the relative detuning can be very small. When an atom absorbs a photon from beam two and is stimulated to emit a photon into beam one, the atom undergoes a change of momentum $\hbar\mathbf{q} = \hbar\mathbf{k}_2 - \hbar\mathbf{k}_1$ and a change of energy $\hbar\omega = \hbar\omega_2 - \hbar\omega_1$.

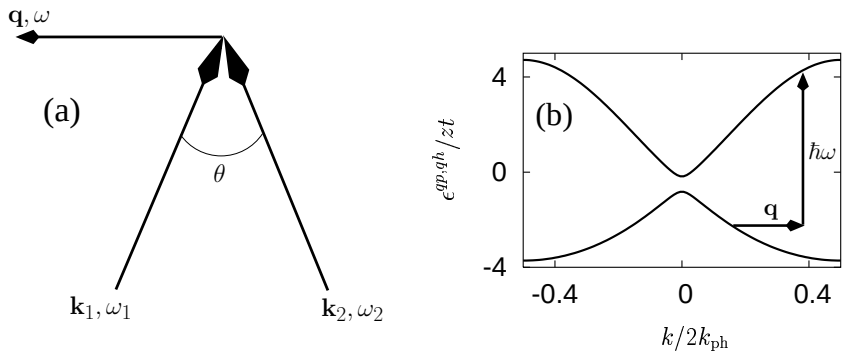

Figure 6.1: (a) Setup for the proposed experiment. (b) Particle and hole dispersions in units of the tunneling parameter in a one-dimensional lattice, for $U/zt = 6$. The horizontal arrow indicates absorption of momentum, the vertical arrow absorption of energy.

In principle any optical transition could be used, but here we use the same transition that is employed to create the lattice potential. This means that the magnitude of the momentum is given by $\hbar q = 2\hbar k_{\rm ph} \sin(\theta/2)$, where to a good approximation $\hbar k_{\rm ph} = 2\pi\hbar/\lambda$ is the photon momentum of both the lasers, λ is equal to the wavelength of the lattice laser light and θ is the angle between the two laser beams. By varying the angle between the two laser beams, any momentum between zero and $2\hbar k_{\rm ph}$ can be transferred and by varying the relative detuning between the beams, the amount of energy that is transferred to the system can be controlled. Note that in experiments, there is always additional harmonic confinement present, which causes a shell of superfluid atoms around a Mott-insulating core [9]. This means that the momentum $\hbar q$ has to be chosen such that the corresponding wave length is smaller than the size of the core.

Calculating the scattering rate for a given momentum $\hbar\mathbf{q}$ and energy $\hbar\omega$ roughly speaking involves counting the number of ways in which the requirements of momentum and energy conservation can be met. To illustrate this process, we draw in Fig. 6.1(b) the quasiparticle and quasihole dispersions in the Mott insulator [43], as is common in solid-state physics. The horizontal and vertical arrows in the figure indicate the transfer of momentum and energy respectively. Since energy is deposited in the system, this scattering rate can be measured in a traploss experiment, or by

determining the increase in temperature of the atoms.

6.2 The scattering rate

To calculate the desired two-photon scattering rate we use Fermi's Golden Rule. In linear response, this can be expressed as

$$I(\mathbf{q},\omega) = -2\mathrm{Im}\left[\Pi(\mathbf{q},\omega)\right]/\hbar,$$

where $\Pi(\mathbf{q},\omega)$ is the polarizibility of the medium. The polarizibility can be written as $\Pi(\mathbf{q},\omega) = (\hbar\Omega/2)^2\,\chi(\mathbf{q},\omega)$, with Ω the effective Rabi frequency for the two-photon process and χ the susceptibility. The retarded susceptibility is given by

$$\chi(\mathbf{q},\omega) = -\frac{V}{\hbar}\int d\mathbf{x}\int_0^\infty dt' e^{-i(\mathbf{q}\cdot\mathbf{x}-\omega t')}\langle\left[a^\dagger(\mathbf{x},t')a(\mathbf{x},t'),a^\dagger(\mathbf{0},0)a(\mathbf{0},0)\right]\rangle, \tag{6.1}$$

with V the volume and $a^\dagger(\mathbf{x},t')$ and $a(\mathbf{x},t')$ creation and annihilation operators of the atoms. Because the atoms are in an optical lattice, we can expand the field operators in terms of the Wannier states of the lattice, which yields an expression in terms of creation and annihilation operators for every lattice site. As mentioned previously, the Hamiltonian of the system then equals the Bose-Hubbard Hamiltonian with a tunneling amplitude t, an on-site interaction energy U and a chemical potential μ. Using the decoupling approach described in Ref. [43], we can write the atomic propagator in the Mott-insulator phase as

$$-\frac{1}{\hbar}G(\mathbf{k},\omega) = \frac{Z(\mathbf{k})}{-\hbar\omega^+ + \epsilon^{\mathrm{qp}}(\mathbf{k})} + \frac{1-Z(\mathbf{k})}{-\hbar\omega^+ + \epsilon^{\mathrm{qh}}(\mathbf{k})}, \tag{6.2}$$

where the probabilities $Z(\mathbf{k})$ and $1-Z(\mathbf{k})$ account for the fact that an atomic excitation contains both quasiparticle and quasihole contributions. The notation $\hbar\omega^+$ is shorthand for $\hbar\omega + i\xi$ with $\xi \downarrow 0$. The dispersions for the quasiparticle and quasihole excitations are given by:

$$\epsilon^{\mathrm{qp,qh}}(\mathbf{k}) = -\mu + \frac{U}{2}(2N_0 - 1) + \frac{1}{2}\left(\epsilon(\mathbf{k}) \pm \hbar\omega(\mathbf{k})\right), \tag{6.3}$$

where N_0 is the filling fraction of the lattice and the function $\epsilon(\mathbf{k}) = -t\sum_{j=1}^{d}\cos 2\pi k_j$ corresponds to the lattice dispersion in the experimentally relevant case of a regular square lattice. The momentum $\hbar\mathbf{k}$ is here

and from now on always written in units of $2\hbar k_{\rm ph}$, which means that the first Brillioun zone runs from $k_j = -1/2$ to $1/2$. The energy $\hbar\omega(\mathbf{k})$ is given by $\hbar\omega(\mathbf{k}) = \sqrt{U^2 + (4N_0+2)U\epsilon(\mathbf{k}) + \epsilon(\mathbf{k})^2}$ and the probability $Z(\mathbf{k})$ is given by $Z(\mathbf{k}) = (U(2N_0+1) + \epsilon(\mathbf{k}) + \hbar\omega(\mathbf{k}))/2\hbar\omega(\mathbf{k})$. Using the Greens function in Eq. (6.2), we find in first approximation $\chi(\mathbf{q},\omega) = t(\mathbf{q})\chi^0(\mathbf{q},\omega) = t(\mathbf{q})\left(\chi^0_+(\mathbf{q},\omega) - \chi^0_+(-\mathbf{q},-\omega)\right)$, where $t(\mathbf{q})$ is a geometric factor that involves the appropriate overlap integral of the relevant Wannier functions. (This will be discussed in the next chapter.) Denoting integration over the first Brillouin zone as $\int_{\rm 1BZ}$, the contribution due to the creation of a particle-hole pair is given by

$$\chi^0_+(\mathbf{q},\omega) = \frac{1}{2}\int_{\rm 1BZ} d\mathbf{k} \frac{P(\mathbf{k},\mathbf{k}+\mathbf{q},\omega)}{-\hbar\omega^+ + \epsilon^{\rm qp}(\mathbf{k}+\mathbf{q}) - \epsilon^{\rm qh}(\mathbf{k})}, \tag{6.4}$$

and the time-reverse process can be written as $\chi^0_-(\mathbf{q},\omega) = \chi^0_+(-\mathbf{q},-\omega)$. Note that when evaluating the above integral, Umklapp processes have to be taken into account. This equation contains the probability $P(\mathbf{k},\mathbf{k}+\mathbf{q},\omega) = (1-Z(\mathbf{k}))\,Z(\mathbf{k}+\mathbf{q})$ for the creation of a hole with momentum $\mathbf{k}$ and a particle with momentum $\mathbf{k}+\mathbf{q}$, and an energy denominator that is associated with the energy cost $\epsilon^{\rm qp}(\mathbf{k}+\mathbf{q}) - \epsilon^{\rm qh}(\mathbf{k})$ of that process. This can readily be verified by taking the imaginary part of the susceptibility, which is proportional to $\int_{\rm 1BZ} d\mathbf{k} P(\mathbf{k},\mathbf{k}+\mathbf{q},\omega)\delta(\hbar\omega - \epsilon^{\rm qp}(\mathbf{k}+\mathbf{q}) + \epsilon^{\rm qh}(\mathbf{k}))$ and can be understood as Fermi's Golden Rule. The actual computation of the above integral is too complicated to do analytically, so that we have resorted to numerical methods. We have achieved this by calculating the imaginary part of Eq. (6.4), which roughly corresponds to integrating over the surface in the Brillouin zone where the energy denominator vanishes. In practice, this amounts to numerically finding the poles of the expression and determining their residue. The real part is calculated from the imaginary part using a Kramers-Kronig relation.

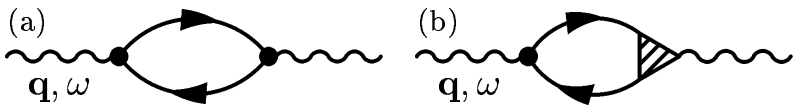

Figure 6.2: Schematic representation of (a) Eq. (6.4) and (b) Eq. (6.6)

However, the results that one would obtain in this manner do not obey particle conservation. Physically, a Raman process with momentum $\mathbf{q}$ cou-

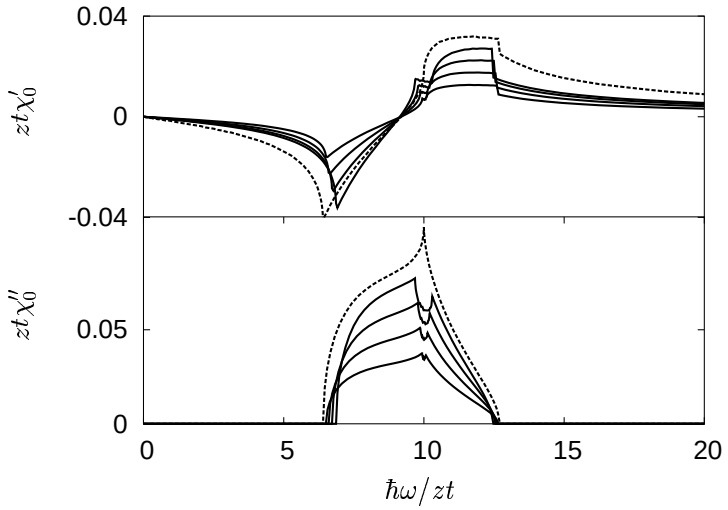

Figure 6.3: Real (χ_0') and imaginary (χ_0'') parts of the susceptibility for $U/zt = 10$ and $\mathbf{q} = 0.10, 0.14, 0.18, 0.20$ along a lattice direction, in two dimensions. The dotted line in the bottom figure is the result for $\mathbf{q} = 0.001$ multiplied by 250 to show the behaviour for small q.

ples to a density fluctuation $\rho(\mathbf{q})$. For zero-momentum transfer, $\rho(\mathbf{0})$ corresponds to the total number of particles and fluctuations are impossible due to particle-number conservation. If we compute the imaginary part of Eq. (6.4) for $\mathbf{q} = 0$ we find however a nonzero spectrum, which means that this approach is not sufficiently accurate. The problem is due to the fact that in Eq. (6.2) not the bare atomic propagator is used, but a dressed propagator which contains a large self-energy correction given by

$$\hbar\Sigma(\mathbf{k}, \omega) = 2N_0U + \frac{N_0(N_0+1)U^2}{\hbar\omega + U + \mu}. \tag{6.5}$$

The first term on the right-hand side is the Hartree-Fock contribution, which is also present in a Bose-Einstein condensate. The second contribution is due to the correlations in the Mott insulator. Essentially this means that an atom moving through the Mott-insulating background is dressed by all the other atoms. As is known from quantum field theory [54], one has to be careful when applying self-energy corrections to the calculation of the

susceptibility, because in general these corrections do not obey the required conservation laws (in this case particle-number conservation). Using field-theoretical methods, we can derive so-called Ward identities, that show that every self-energy correction requires a corresponding vertex correction in order to restore the conservation laws. Physically this means, that if the atom is dressed, we also have to dress the atom-photon coupling. Diagrammatically this is illustrated in Fig. 6.2. This situation is analogous to the situation in a superconductor, where the naive BCS calculation of the electro-magnetic response is not gauge invariant and a more involved approach is needed [55]. Using the relevant Ward identity we can derive that the intuitive probability function given above, has to be replaced by

$$P(\mathbf{k}, \mathbf{k}+\mathbf{q}, \omega) = \frac{2\hbar\omega - \epsilon^{\mathrm{qp}}(\mathbf{k}+\mathbf{q}) + \epsilon^{\mathrm{qh}}(\mathbf{k})}{\hbar\omega(\mathbf{k}+\mathbf{q}) + \hbar\omega(\mathbf{k})} \times \left(Z(\mathbf{k}+\mathbf{q}) - Z(\mathbf{k})\right). \quad (6.6)$$

Note that the probability now vanishes when $\mathbf{q} \to 0$, so that particle conservation is indeed no longer violated. In fact, we can show that for small $\mathbf{q}$ and $\hbar\omega$ just above threshold $P \propto q^2/\Delta_0^2$, where Δ_0 is the gap for particle-hole excitations.

6.3 Results

In Figs. 6.3 and 6.4 the result of a numerical integration is shown in two and three dimensions, respectively. Both calculations have been carried out for a regular square lattice and the momentum $\mathbf{q}$ is chosen along a principal lattice direction. All energies in the following figures are given in units of zt, where z is the coordination number of the lattice.

The imaginary part of Fig. 6.3 clearly shows singularities around $\hbar\omega = U$. These singularities are due to the fact that there are saddle points in the dispersion and that a saddle point in the dispersion causes an integrable singularity in the density of states. These are so-called van Hove singularities [56]. It is interesting to see, that the van Hove singularities split up as the momentum is increased, which is caused by the fact that the saddle-point energy in the direction of $\mathbf{q}$ and the saddle-point energy in the orthogonal direction(s) are shifted by different amounts. This is also visible in Fig. 6.4. However, it is less clear in this case, because the van Hove singularities are more smeared out in three dimensions. Also, the opening of the threshold for the two-photon absorption in the three-dimensional case is

far less steep than in the two-dimensional case. Note that when additional harmonic confinement is present, some background signal is expected due to the superfluid shell around the Mott insulator. To investigate possible

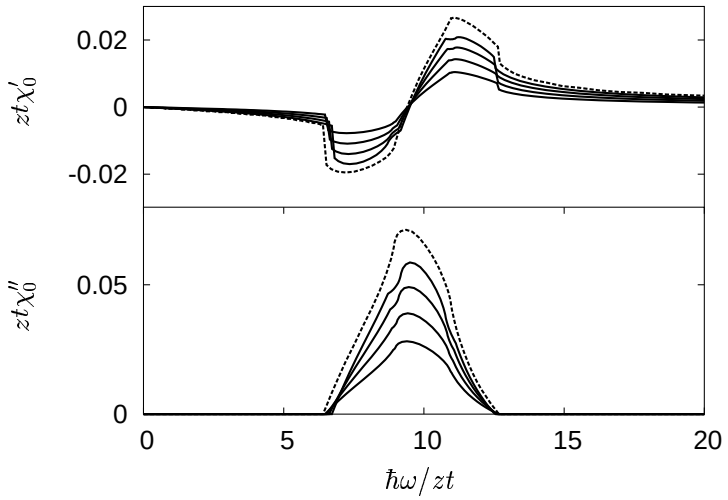

Figure 6.4: Real and imaginary parts of the susceptibility for $U/zt = 10$ and $\mathbf{q} = 0.10, 0.14, 0.18, 0.20$ along a lattice direction, in three dimensions. The dotted line in the bottom figure is the result for $\mathbf{q} = 0.001$ multiplied by 250 to show the behaviour for small q.

collective modes in this system, we determined higher-order corrections in the random-phase approximation (RPA). It can be shown that in RPA the susceptibility is given by $\chi(\mathbf{q},\omega) = t(\mathbf{q})\chi^0(\mathbf{q},\omega)/(1 - 2U\chi^0(\mathbf{q},\omega)))$. This means that there is a resonance in the scattering rate when the real part of $\chi^0(\mathbf{q},\omega)$ is equal to $1/U$. However, as can be seen from Figs. 6.3 and 6.4, the real parts in both cases are rather small compared to $1/U$ for experimentally relevant values of U, which are typical on the order of $U/zt \approx 10$ [15]. Therefore, including the RPA denominator does not qualitatively change our previous results. Of course, for much larger values of U the RPA denominator always becomes important. In Fig. 6.5 we plot the imaginary part of χ_0, for a range of values for the coupling constant U/zt, and for a fixed momentum $\mathbf{q} = 0.10$. We see, that the threshold behaviour becomes

steeper as we approach the critical value of $U_c/zt \approx 5.83$. This steepening is caused by the fact that close to the quantum critical point, the dispersion stiffens and becomes almost linear, as illustrated in Fig. 6.1(b). We also see that there remains a nonzero gap when $U = U_c$. This is due to the fact that we are not considering a zero-momentum excitation, due to the reasons given above. In the inset of Fig. 6.5, we plot this gap Δ_q as a function of U/zt. For large U the gap grows linearly with U and for U close to U_c, the gap closes more rapidly. In the case of $\mathbf{q} = \mathbf{0}$ the gap would in our mean-field approximation close as $\sqrt{U - U_c}$ when $U \downarrow U_c$, but for small nonzero $\mathbf{q}$ it closes as $\sqrt{U - U_c + \eta q^4}$, where the factor η is a positive function of U_c and t.

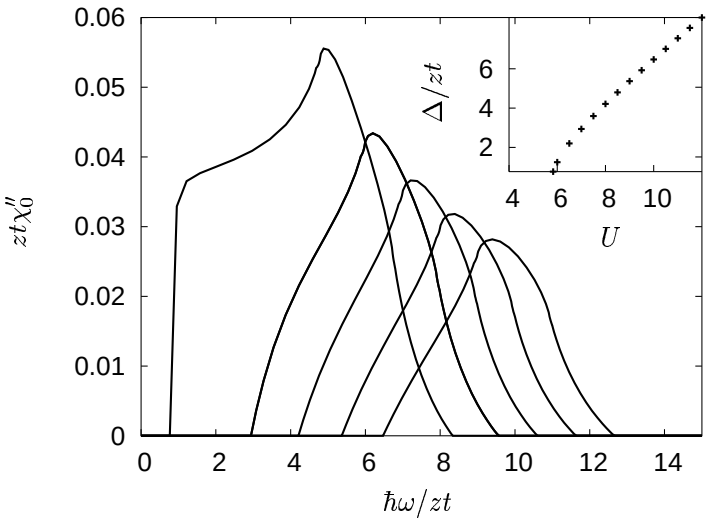

Figure 6.5: Imaginary part of the susceptibility in a three dimensional lattice for $\mathbf{q} = 0.10$ along a lattice direction and $U/zt = 5.83, 7, 8, 9, 10$

6.4 Discussion

In summary, we have proposed a means of studying Mott insulators in optical lattices, using the relatively well-known technique of Bragg spectroscopy. We have presented spectra that can be measured directly by trap

loss or heating measurements. In a recent experiment by Stöferle *et al.* [57] the authors use a setup where the laser beams are perfectly counter-propagating, which corresponds to a quasi-momentum transfer of zero. As we have argued above, there should be no scattering in that case and the signal can only be due to nonlinear response or due to the fact that the system is inhomogeneous and of finite size. We have found that by measuring the threshold behaviour of the two-photon scattering rate at various quasimomenta, it is possible to determine the gap by extrapolation. We have shown that for a theoretical description of Bragg spectroscopy on the Mott insulator it is absolutely essential to dress the photon-atom coupling, which is unexpected, as the same corrections are absent in the case of an harmonically trapped gas. As a result it turns out that although it is common to use the language of solid-state physics to describe these systems, the physics is quantitatively and even qualitatively very different due to the many-body effects.

Chapter 7

Bragg spectroscopy and atom-number conservation

Abstract

We calculate the structure factor of the Mott insulator. We show that both self-energy corrections of the atoms and corrections to the atom-photon coupling have to be taken into account. We derive the relevant Ward identity to calculate the vertex corrections corresponding to the self-energy corrections.

7.1 Introduction

In the previous chapter, a calculation was presented of the two-photon scattering rate in an optical Bragg-spectroscopy experiment. It was shown that such an experiment can be used to measure the particle-hole excitation spectrum of the Mott-insulating state of atoms in an optical lattice. By studying this excitation spectrum as a function of the critical parameter U/t, where U is the interaction strength and t is the tunneling parameter, insight is gained on the behaviour of the particle-hole gap as the system approaches the quantum-critical point. An important conclusion of the previous chapter is that it is vital to include vertex corrections to the calculation of the two-photon scattering rate, in order to obtain the correct results. In this chapter, a more thorough discussion of the technical parts of that chapter is given.

7.2 Inelastic light scattering

The quantity that is calculated in the previous chapter is the retarded susceptibility $\chi(\mathbf{q},\omega)$, where $\hbar\mathbf{q}$ and $\hbar\omega$ are the momentum and energy transfered in the two-photon process, respectively. In the Heisenberg representation, this susceptibility is given by

$$\chi(\mathbf{q},\omega) = -\frac{V}{\hbar}\int d\mathbf{x}\int_0^\infty dt' e^{-i(\mathbf{q}\cdot\mathbf{x}-\omega t')}\langle[a^\dagger(\mathbf{x},t')a(\mathbf{x},t'),a^\dagger(\mathbf{0},0)a(\mathbf{0},0)]\rangle, \tag{7.1}$$

with V the volume and $a^\dagger(\mathbf{x},t')$ and $a(\mathbf{x},t')$ creation and annihilation operators of the atoms. The polarizibility $\Pi(\mathbf{q},\omega)$ of the atoms can be written as $\Pi(\mathbf{q},\omega) = (\hbar\Omega/2)^2\chi(\mathbf{q},\omega)$ and the scattering rate as $I(\mathbf{q},\omega) = -2\mathrm{Im}\left[\Pi(\mathbf{q},\omega)\right]/\hbar$. When expanding the above equation in terms of the Wannier states of the lattice we have to be careful, since the light acts in a simple manner on the momentum states of the atoms but not on the Wannier states. We can see more this clearly when we write down the Hamiltonian for the light-scattering process H_{coup} in the Schödinger representation:

$$\begin{aligned} H_{\mathrm{coup}} &= \frac{\hbar\Omega}{2}e^{i\omega t'}\int d\mathbf{x}e^{-i\mathbf{q}\cdot\mathbf{x}}a^\dagger(\mathbf{x})a(\mathbf{x}) \\ &= \frac{\hbar\Omega}{2}e^{i\omega t'}\sum_{ij}a_i^\dagger a_j\int d\mathbf{x}e^{-i\mathbf{q}\cdot\mathbf{x}}\chi_0^*(\mathbf{x}-\mathbf{x}_i)\chi_0(\mathbf{x}-\mathbf{x}_j), \end{aligned} \tag{7.2}$$

where $\mathbf{x}_i$ is the position corresponding to site i and $\chi_0(\mathbf{x})$ is the lowest Wannier state of the lattice. The operator $a_i^\dagger$ and a_i create and annihilate a particle in the i-th site, respectively. For typical experimental parameters the Wannier states can to a very good approximation be taken as Gaussian functions. For the experimentally relevant case of a regular square or cubic lattice with a lattice spacing of $a = \lambda/2$ we find

$$H_{\mathrm{coup}} = \frac{\hbar\Omega}{2}e^{i\omega t'}\sum_{ij}a_i^\dagger a_j e^{-i\mathbf{q}\cdot\mathbf{x}_i/2}e^{-i\mathbf{q}\cdot\mathbf{x}_j/2}e^{-q^2l^2/4}e^{-|\mathbf{x}_j-\mathbf{x}_i|^2/4l^2}, \tag{7.3}$$

where l is the width of the Gaussian wave function. Since the factor $\exp\left(-|\mathbf{x}_j-\mathbf{x}_i|^2/4l^2\right)$ drops rapidly with distance, the summation can be

restricted to nearest neighbours. In that case the coupling Hamiltonian reads

$$H_{\text{coup}} = \frac{\hbar\Omega}{2} e^{i\omega t'} \sum_{\mathbf{k}} a^{\dagger}_{\mathbf{k}+\mathbf{q}} a_{\mathbf{k}} f(\mathbf{q}), \tag{7.4}$$

where the geometric overlap function $f(\mathbf{q})$ is given by

$$f(\mathbf{q}) = 8e^{-q^2 l^2/4} e^{-a^2/4l^2} \prod_{j=1}^{d} \cos(aq_j), \tag{7.5}$$

where there summation variable j runs over all cartesian directions in d dimensions. Note, that this function is similar to the function $\epsilon(\mathbf{k})$ as used in Chapters 4 and 6. If Eq. (7.1) is written on a Wannier basis by following the above procedure, we find that without vertex corrections $\chi(\mathbf{q},\omega)/t(\mathbf{q})$ equals

$$\chi_0(\mathbf{q},\omega) = -\frac{1}{\hbar} \frac{1}{N_s \hbar\beta} \sum_{n\mathbf{k}} G(\mathbf{k},\omega_n) G(\mathbf{k}+\mathbf{q},\omega_n+\omega), \tag{7.6}$$

where N_s is the number of sites in the lattice, ω_n are the Matsubara frequencies given by $\hbar\omega_n = \pi(2n)/\hbar\beta$ and $t(\mathbf{q}) = |f(\mathbf{q})|^2$. The atomic propagator $G(\mathbf{k},\omega_n)$ is an analytical continuation of the propagator presented in the previous chapter. Because the atomic propagator contains both particle and hole contributions, the above equation contains a contribution due to the creation of a hole with momentum $\hbar\mathbf{k}$ and a particle with momentum $\hbar\mathbf{k} + \hbar\mathbf{q}$, but also due to the reverse process. We therefore write

$$\chi_0(\mathbf{q},\omega) = (\chi_0^{+}(\mathbf{q},\omega) + \chi_0^{-}(\mathbf{q},\omega))$$

However it can easily be shown that the second contribution is equal to $\chi_0^{-}(\mathbf{q},\omega)) = -\chi_0^{+}(-\mathbf{q},-\omega)$. We therefore only have to evaluate $\chi_0^{+}(\mathbf{q},\omega)$, which is given by the following expression

$$\chi_0^{+}(\mathbf{q},\omega) = \frac{1}{2} \int_{1\text{BZ}} d\mathbf{k} \frac{P(\mathbf{k},\mathbf{k}+\mathbf{q},\omega)}{-\hbar\omega^{+} + \epsilon^{\text{qp}}(\mathbf{k}+\mathbf{q}) - \epsilon^{\text{qh}}(\mathbf{k})}. \tag{7.7}$$

The momentum $\hbar\mathbf{k}$ is here and from now on always written in units of $2\hbar k_{\text{ph}}$, which means that the first Brillioun zone runs from $k_j = -1/2$ to $1/2$. The scattering rate of the two-photon process can be calculated by taking the

imaginairy part of this expression. By calculating the scattering rate as a function of frequency ω for a given momentum $\hbar\mathbf{q}$, a spectrum can be obtained. As described in the previous chapter, numerically evaluating this integral for $\mathbf{q} \to \mathbf{0}$ yields a nonzero spectrum. In the next section we argue why this physically cannot be correct. After that we present a derivation of the vertex corrections that are needed to solve this problem.

7.3 Sum rules

To understand why the two-photon spectrum should go to zero when the momentum goes to zero, we now derive the relevant sum rule. The operators in Eq. (7.1) are expanded into plane waves as

$$\begin{aligned} a(\mathbf{x},t') &= \frac{1}{\sqrt{\hbar\beta V}} \sum_{n\mathbf{k}} a_{\mathbf{k}}(\omega_n) e^{i(\mathbf{k}\cdot\mathbf{x}-\omega_n t')}, \\ a^\dagger(\mathbf{x},t') &= \frac{1}{\sqrt{\hbar\beta V}} \sum_{n\mathbf{k}} a^\dagger_{\mathbf{k}}(\omega_n) e^{-i(\mathbf{k}\cdot\mathbf{x}-\omega_n t')}. \end{aligned} \tag{7.8}$$

The density operator is given by $\rho(\mathbf{x},t') = a^\dagger(\mathbf{x},t')a(\mathbf{x},t')$. The Fourier transform of this operator can be written in terms of the above operators $a^\dagger_{\mathbf{k}}$ and $a_{\mathbf{k}}$ as

$$\rho_{\mathbf{q}}(\omega) = (\hbar\beta V)^{-1/2} \sum_{n\mathbf{k}} a^\dagger_{\mathbf{k}+\mathbf{q}}(\omega_n+\omega) a_{\mathbf{k}}(\omega_n). \tag{7.9}$$

Using this definition, Eq. (7.1) can be written as

$$\chi(\mathbf{q},\omega) = \frac{V}{\hbar} \left\langle \left[\rho^\dagger_{\mathbf{q}}(\omega), \rho_{\mathbf{q}}(\omega) \right] \right\rangle. \tag{7.10}$$

We now calculate the total energy absorption, which is defined as $E = \int d\omega I(\mathbf{q},\omega)\hbar\omega$. As $I(\mathbf{q},\omega)$ is proportional to the imaginary part of $\chi(\mathbf{q},\omega)$, we can write $E = V\left(\hbar\Omega/2\right)^2 \int d\omega \mathrm{Im}\left[\left\langle\left[\omega\rho^\dagger_{\mathbf{q}}(\omega),\ \rho_{\mathbf{q}}(\omega)\right]\right\rangle\right]$. Since $\rho^\dagger_{\mathbf{q}}(\omega)$ is defined by a Fourier expansion, the frequency ω can be replaced by a time derivative $-i\partial/\partial t$. Because ρ is a density, it has to obey the continuity equation, which means that $\partial\rho^\dagger_{\mathbf{q}}(\omega)/\partial t = \nabla\cdot\mathbf{J}_{\mathbf{q}}(\omega)$, where $\mathbf{J}_{\mathbf{q}}(\omega)$ is the current density. Using this result we find

$$E = V\left(\frac{\hbar\Omega}{2}\right)^2 \int d\omega \mathrm{Im}\left[\mathbf{q}\cdot\langle[\mathbf{J}_{\mathbf{q}}(\omega),\rho_{\mathbf{q}}(\omega)]\rangle\right]. \tag{7.11}$$

The expectation value $\langle[\mathbf{J_q}(\omega), \rho_\mathbf{q}(\omega)]\rangle$ is a vector, which is a function of $\mathbf{q}$ only. In the simplest case, the expectation value is therefore proportional to $\mathbf{q}$, which means $E \propto q^2$. This shows that the spectrum vanishes when $\mathbf{q} \to 0$. This result can in fact be easily understood. As shown in Eq. (7.10), a two-photon transition with an effective wave number of $\mathbf{q}$ couples to density fluctuations with that same wave number. If the wave number $\mathbf{q}$ is zero, the light couples to fluctuations in $\rho_\mathbf{0}(\omega)$, which corresponds to fluctuations in the total number of particles in the system. Since the total number of particles in the system is conserved, these fluctuations can obviously not occur.

7.4 Gauge invariance

As argued in the previous section, Eq. (7.6) violates particle-number conservation. From a fundamental point of view this conservation law is due to a so-called global U(1) symmetry. To explore the consequences of this global symmetry we first increase the global symmetry to a local symmetry, i.e., we make the theory locally invariant under a U(1) gauge symmetry. From this gauge invariance we can then derive certain relations that have to be fullfilled by the density-density correlation function of interest to us. Finally, we take the appropriate limit to recover the corrections to the absorption spectrum that are required by the global symmetry of our original problem.

As a first step, the consequences of gauge invariance will be determined for a very general partition function of the form

$$Z[\eta, \eta^*, J^\mu] = \int d[a^*]d[a]d[A_\mu] \exp\left\{\frac{i}{\hbar}S[a^*, a, A_\mu] + i\int dtd\mathbf{x}\,(a^*(\mathbf{x},t)\eta(\mathbf{x},t) + a(\mathbf{x},t)\eta^*(\mathbf{x},t) + J^\mu(\mathbf{x},t)A_\mu(\mathbf{x},t))\right\}, \tag{7.12}$$

were a^* and a are the atomic fields and A_μ is the electro-magnetic field. Note, that for the greek indices the Einstein summation convention applies. The purpose of the source terms η, η^* and J^μ becomes apparent later on.

The action $S[a^*, a, A_\mu]$ is general, except that minimal coupling is assumed

$$\begin{aligned} i\hbar\frac{\partial}{\partial t} &\rightarrow i\hbar\frac{\partial}{\partial t} + \phi(\mathbf{x}, t) \\ -i\hbar\frac{\partial}{\partial \mathbf{x}} &\rightarrow -i\hbar\frac{\partial}{\partial \mathbf{x}} + \mathbf{A}(\mathbf{x}, t), \end{aligned} \tag{7.13}$$

where ϕ is the electric potential and $\mathbf{A}$ is the vector potential. In four-vector notation the vector potential is written as $A_\mu = (-\phi/c, \mathbf{A})$ and the position is written as $x_\mu = (-ct, \mathbf{x})$. Using this notation we have $i\hbar\partial_\mu \rightarrow i\hbar\partial_\mu + A_\mu(x)$. Here c is the speed of light. It is clear that if we replace in Eq. (7.12) all the instances of a^*, a and A_μ by dummy variables a'^*, a' and A'_μ, the value of the integral should not change. We then apply the gauge transformations

$$\begin{aligned} a'(x) &\rightarrow e^{i\theta(x)}a(x) \\ A'_\mu(x) &\rightarrow A_\mu(x) + \hbar\partial_\mu\theta(x), \end{aligned} \tag{7.14}$$

to these dummy integration variables and use the fact that the action is gauge invariant. If the resulting expression is linearized with respect to θ, we find $Z' = Z + \delta Z$, with

$$\begin{aligned} \delta Z[\eta, \eta^*, J^\mu] = \int d[a^*]d[a]d[A_\mu]\,(-i\theta a^*\eta + i\theta a\eta^* + \hbar\partial_\mu\theta J^\mu) \\ \times \exp\left\{\frac{i}{\hbar}S[a^*, a, A_\mu] + i\int dx\,(a^*\eta + a\eta^* + J^\mu A_\mu)\right\}, \end{aligned} \tag{7.15}$$

where we have dropped the argument x to simplify notation. The gauge invariance of the system is now reflected in the fact that $\delta Z = 0\ \forall\ \theta(\mathbf{x}, t)$. By applying a partial integration to the current terms, we find

$$\delta Z[\eta, \eta^*, J^\mu] = \left\{-\eta\frac{\delta}{\delta\eta} + \eta^*\frac{\delta}{\delta\eta^*} - \hbar\partial_\mu J^\mu\right\} Z[\eta, \eta^*, J^\mu] = 0. \tag{7.16}$$

Behind this seemingly mathematical exercise hides a very important physical conclusion. Any action that contains only minimal coupling to the electro-magnetic fields has to satisfy Eq. (7.16) in order to obey gauge invariance. Since the partition function Z in principle contains all the possible scattering processes, this result can be used to determine the consequences of gauge invariance for all these processes. More specifically, we use it to calculate corrections to Eq. (7.7).

The next step is to write $Z[\eta, \eta^*, J^\mu] \equiv \exp\{iW[\eta, \eta^*, J^\mu]\}$. The reason behind this substitution is that Z is the generating function of all Greens functions and W is the generating function of only the connected contributions. By differentiating Eq. (7.12) with respect to the source terms η, η^* and J^μ and using the above definition for $W[\eta, \eta^*, J^\mu]$ we find

$$\frac{\delta W}{\delta \eta} = \langle a^* \rangle \equiv \phi^*, \; \frac{\delta W}{\delta \eta^*} = \langle a \rangle \equiv \phi, \; \frac{\delta W}{\delta J^\mu} = A_\mu. \tag{7.17}$$

Note that for simplicity we have denoted the average $\langle A_\mu \rangle$ by A_μ again. We now define the functional $\Gamma[\phi^*, \phi, A_\mu]$ by introducing the following Legendre transformation

$$\Gamma[\phi^*, \phi, A_\mu] = \int dx \, (\phi^* \eta + \eta^* \phi + J^\mu A_\mu) - W[\eta, \eta^*, J^\mu]. \tag{7.18}$$

This equation is important, as $\Gamma[\phi^*, \phi, A_\mu]$ corresponds to the exact effective action of the system in terms of the expectation values ϕ and ϕ^*, through

$$S^{\text{eff}}[\phi^*, \phi, A_\mu] = -\hbar \Gamma[\phi^*, \phi, A_\mu]. \tag{7.19}$$

As we have already derived an expression for the effective action of the atoms, we want to write Eq. (7.16) in terms of $\Gamma[\phi^*, \phi, A_\mu]$. In order to achieve this, we substitute $Z[\eta, \eta^*, J^\mu] = \exp\{iW[\eta, \eta^*, J^\mu]\}$ into Eq. (7.16), which yields

$$\left(-\eta \frac{\delta}{\delta \eta} + \eta^* \frac{\delta}{\delta \eta^*} \right) W = \frac{\hbar}{i} \partial_\mu J^\mu. \tag{7.20}$$

From the Legendre transformation in Eq. (7.18) we find that

$$\frac{\delta \Gamma}{\delta \phi} = \eta, \; \frac{\delta \Gamma}{\delta \phi^*} = \eta^*, \; \frac{\delta \Gamma}{\delta A_\mu} = J^\mu, \tag{7.21}$$

which allows us to rewrite Eq. (7.20) as

$$\left(-\phi^* \frac{\delta}{\delta \phi^*} + \phi \frac{\delta}{\delta \phi} \right) \Gamma = \frac{\hbar}{i} \partial_\mu \frac{\delta \Gamma}{\delta A_\mu}. \tag{7.22}$$

Physically this equation has the same interpretation as Eq. (7.16) except that it contains only the one-particle irreducible Greens functions. In the next section, the importance of this equation is made apparent.

7.5 The Ward identity

As mentioned above, $\Gamma[\phi^*, \phi, A_\mu]$ is proportional to the exact effective action. In the case of atoms in an electromagnetic field, the simplest form for $\Gamma[\phi^*, \phi, A_\mu]$ can therefore be written as

$$\Gamma[\phi^*, \phi, A_\mu] = -\phi^* G^{-1} \phi + \phi^* \phi \Gamma^\mu A_\mu, \tag{7.23}$$

where G is the exact propagator of the atoms and Γ^μ is the exact three-point interaction vertex between the atoms and the photons. This means that if we have an expression for $\Gamma[\phi^*, \phi, A_\mu]$, we can write

$$G^{-1}(x, x') = -\frac{\delta^2 \Gamma}{\delta\phi^*(x)\delta\phi(x')}, \tag{7.24a}$$

$$\Gamma^\mu(x, x', x'') = -\frac{\delta^3 \Gamma}{\delta\phi^*(x)\delta\phi(x')\delta A_\mu(x'')}, \tag{7.24b}$$

where we have shown the explicit position and time dependence of the fields for clarity reasons. Applying $\delta^2/\delta\phi^*\delta\phi$ to Eq. (7.22) and using Eqs (7.24a) and (7.24b), yields

$$\delta(x - x'')G^{-1}(x'' - x') - \delta(x' - x'')G^{-1}(x - x'') = -i\hbar\partial_\mu \Gamma^\mu(x, x', x''). \tag{7.25}$$

Performing a Fourier transformation on the above equation, we find

$$\hbar q_\mu \Gamma^\mu(k + q, k) = G^{-1}(k) - G^{-1}(k + q), \tag{7.26}$$

where k is the momentum of the incoming atom and q is the momentum of the photon. To find the vertex correction we write $\Gamma^\mu = \gamma^\mu + \Delta\Gamma^\mu$, where γ_μ is the bare vertex. We can then obtain from the Dyson equation $G^{-1} = G_0^{-1} + \hbar\Sigma$ that

$$\hbar q_\mu \gamma^\mu = G_0^{-1}(k) - G_0^{-1}(k + q), \tag{7.27a}$$

$$\hbar q_\mu \Delta\Gamma^\mu = \hbar\Sigma(k) - \hbar\Sigma(k + q), \tag{7.27b}$$

where G_0 is the bare propagator of the atom and $\hbar\Sigma$ is the self energy. The above equation is the simplest Ward identity. By taking higher-order derivatives, corrections to higher-order vertices can be derived. For our purposes, the simplest case suffices.

7.6 Vertex correction to the susceptibility

To determine the scattering rate of the two-photon proces, we have to calculate the diagram in Fig. 7.1(b). The graph of the left shows the calculation without vertex corrections. In order to calculate the vextex correction $\Delta\Gamma^{\mu}$

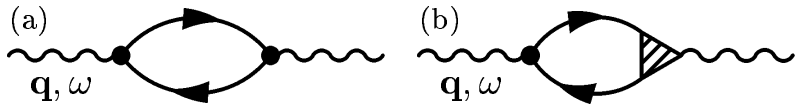

Figure 7.1: Schematic representation of the light scattering proces with a bare vertex (a) and with a dressed vertex (b).

we first have to determine the self-energy correction $\hbar\Sigma$. From Eq. 6.2 we have

$$\begin{aligned} -\frac{1}{\hbar}G(\mathbf{k},\omega) &= \frac{Z(\mathbf{k})}{-\hbar\omega+\epsilon^{\mathrm{qp}}(\mathbf{k})} + \frac{1-Z(\mathbf{k})}{-\hbar\omega+\epsilon^{\mathrm{qh}}(\mathbf{k})} \\ &\equiv \frac{1}{-\hbar\omega-\epsilon_{\mathbf{k}}+\hbar\Sigma(\mathbf{k},\omega)-\mu}, \end{aligned} \tag{7.28}$$

from which we can determine that the self energy is given by

$$\hbar\Sigma(\mathbf{k},\omega) = 2N_0U + \frac{N_0(N_0+1)U^2}{\hbar\omega+U+\mu}. \tag{7.29}$$

Here N_0 is the filling fraction, U is the on-site interaction strength and μ is the chemical potential. Because the self energy does not depend on momentum $\Delta\Gamma^i = 0$ and we can use only the zeroth component of Eq. (7.27b). We have explicitely that

$$\begin{aligned} -\hbar\omega\Delta\Gamma^0 &= \hbar\Sigma(\mathbf{k},\omega_0) - \hbar\Sigma(\mathbf{k}+\mathbf{q},\omega_0+\omega) \\ &= \frac{N_0(N_0+1)U^2}{\hbar\omega_0+U+\mu} - \frac{N_0(N_0+1)U^2}{\hbar\omega_0+\hbar\omega+U+\mu} \\ &= \frac{N_0(N_0+1)U^2\hbar\omega}{(\hbar\omega_0+U+\mu)(\hbar\omega_0+\hbar\omega+U+\mu)}. \end{aligned} \tag{7.30}$$

To arrive at a correct expression for the susceptibility, the summant of Eq. (7.6) is multiplied by $(1+\Delta\Gamma^0)$. After performing the Matsubara

summation in Eq. (7.6), we find that the corrected expression has exactly the same form as Eq. (7.7), only the probability $P(\mathbf{k}, \mathbf{k}+\mathbf{q}, \omega)$ is replaced by

$$P(\mathbf{k}, \mathbf{k}+\mathbf{q}, \omega) = \frac{2\hbar\omega - \epsilon^{\mathrm{qp}}(\mathbf{k}+\mathbf{q}) + \epsilon^{\mathrm{qh}}(\mathbf{k})}{\hbar\omega(\mathbf{k}+\mathbf{q}) + \hbar\omega(\mathbf{k})} \left(Z(\mathbf{k}+\mathbf{q}) - Z(\mathbf{k})\right). \quad (7.31)$$

As shown in the previous chapter, for small $\mathbf{q}$ and $\hbar\omega$ just above threshold this probability scales as $P \propto q^2/\Delta_0^2$, where Δ_0 is the gap for particle-hole excitations. This means that the absorption signal indeed vanishes when $\mathbf{q} \to 0$.

7.7 Random-phase approximation

To investigate the possibility of collective excitations in the system, we now calculate corrections due to collisions between particles and holes. We do this in the so-called random-phase approximation (RPA). We start by writing down the action in momentum space

$$\begin{aligned} S[a^*, a] &= -\hbar \sum_{n\mathbf{k}} a^*_{n\mathbf{k}} G^{-1}(n\mathbf{k}) a_{n\mathbf{k}} + S_{\mathrm{I}}, \\ S_{\mathrm{I}} &= -\frac{U}{2N_s\hbar\beta} \sum_{n,n',n'',\mathbf{k},\mathbf{k}',\mathbf{k}''} a^*_{n+n''\mathbf{k}+\mathbf{k}''} a^*_{n'-n''\mathbf{k}'-\mathbf{k}''} a_{n\mathbf{k}} a_{n'\mathbf{k}'}. \end{aligned} \quad (7.32)$$

To calculate the susceptibility for this system, a power expansion in terms of the interaction part of the action S_{I} must be made, which is roughly speaking given by $\langle a^4 \rangle = \sum_\alpha \langle a^4 S_{\mathrm{I}}^\alpha \rangle / \hbar^\alpha \alpha!$. The RPA now amounts to taking into account only the terms that consist of a string of bubble diagrams as illustrated in Fig. 7.2. This yields a geometric series in terms of the

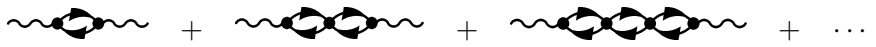

Figure 7.2: Feynman diagrams corresponding to the first three terms in the bubble summation.

lowest-order susceptibility, which can be easily summed to find

$$\chi(\mathbf{q}, \omega) = \frac{t(\mathbf{q})\chi_0(\mathbf{q}, \omega)}{1 - 2U\chi_0(\mathbf{q}, \omega)}. \quad (7.33)$$

In two and three dimensions, this correction does not qualitatively change the spectrum due to the fact that the real part of χ_0 is much smaller than $1/U$ for experimentally relevant values for U, as is shown in the previous chapter. For very large values of U, poles can arise in $\chi(\mathbf{q}, \omega)$, which will describe the collective modes due to density fluctuations in the Mott insulator.

7.8 Discussion

A very simple argument shows that in order to satisfy particle-number conservation, the two-photon scattering rate of atoms in a Mott-insulating state has to vanish when zero momentum is being transfered in the Raman process. In order to satisfy this requirement, a calculation of the scattering rate has to include vertex corrections, which are derived here by using a so-called Ward identity. It is relatively unexpected that a formal calculation such as presented in Secs. 7.4-7.6 should be required to make predictions for an experimental technique that is used throughout the field of Bose-Einstein condensation. This is a good illustration of the richness of the physics of a Bose-Einstein condensate in an optical lattice.

Furthermore, we have shown that there are no collective excitations in the limit where our model is applicable. In agreement with other studies we expect that in the limit of $U \to \infty$ collective excitations do exist. A comparison between our RPA approximation and the calculations presented by Rey *et al.* [58] is beyond the scope of this thesis and requires further study.

Bibliography

[1] P. S. Jessen, C. Gerz, P. D. Lett, W. D. Phillips, S. L. Rolston, R. J. C. Spreeuw, and C. I. Westbrook, Phys. Rev. Lett. **69**, 49 (1992).

[2] H. J. Metcalf and P. van der Straten, *Laser Cooling and Trapping* (Springer-Verlag, New York, 1999).

[3] G. Grynberg, B. Lounis, P. Verkerk, J.-Y. Courtois, and C. Salomon, Phys. Rev. Lett. **70**, 2249 (1993).

[4] K. B. Davis, M.-O. Mewes, M. R. Andrews, N. J. van Druten, D. S. Durfee, D. M. Kurn, and W. Ketterle, Phys. Rev. Lett. **75**, 3969 (1995).

[5] M. H. Anderson, J. R. Ensher, M. R. Matthews, C. E. Wieman, and E. A. Cornell, Science **269**, 198 (1995).

[6] C. C. Bradley, C. A. Sackett, J. J. Tollett, and R. G. Hulet, Phys. Rev. Lett. **75**, 1687 (1995).

[7] C. Orzel, A. K. Tuchman, M. L. Fenselau, M. Yasuda, and M. A. Kasevich, Science **291**, 2386 (2001).

[8] M. Dahan, E. Peil, J. Reichel, Y. Castin, and C. Salomon. Phys. Rev. Lett. **76**, 4508 (1996).

[9] D. Jaksch, C. Bruder, J. I. Cirac, C. W. Gardiner, and P. Zoller, Phys. Rev. Lett. **81**, 3108 (1998).

[10] M. P. A. Fisher, P. B. Weichman, G. Grinstein, and D. S. Fisher, Phys. Rev. B **40**, 546 (1989).

[11] S. Sachdev, *Quantum Phase Transitions* (Cambridge Univ. Press, Cambridge, 2001).

[12] E. D. van Ooijen, Ph.D. thesis, Utrecht University, to be published.

[13] O. Mandel, M. Greiner, A. Widera, T. Rom, T. W. Hänsch, and I. Bloch, Phys. Rev. Lett. **91**, 010407 (2003).

[14] M. Greiner, I. Bloch, O. Mandel, T. W. Hänsch, and T. Esslinger, Phys. Rev. Lett. **87**, 160405 (2001).

[15] M. Greiner, O. Mandel, T. Esslinger, T. W. Hänsch, and I. Bloch, Nature **415**, 39 (2002).

[16] K. I. Petsas, A. B. Coates, and G. Grynberg, Phys. Rev. A **50**, 5173 (1994).

[17] T. Busch, B.-G. Englert, K. Rzazewski, and M. Wilkens, Foundations of Physics, **28**, 549 (1998).

[18] T. D. Lee, K. Huang, and C. N. Yang, Phys. Rev. **106**, 1135 (1957).

[19] *Handbook of Mathematical Functions*, edited by M. Abramowitz and I. A. Stegun (Dover, New York, 1972).

[20] P. A. Molenaar, *Photoassociative reactions of laser-cooled sodium*, Ph.D. thesis, Utrecht University (1996).

[21] W. Ketterle, K. B. Davis, M. A. Joffe, A. Martin, and D. E. Pritchard, Phys. Rev. Lett **70**, 2253 (1993).

[22] M. D. Barrett, J. A. Sauer, and M. S. Chapman, Phys. Rev. Lett. **87**, 010404 (2001).

[23] T. Weber, J. Herbig, M. Mark, H.-C. Nägerl, and R. Grimm, Science **299**, 232 (2003).

[24] M. Born and E. Wolf, *Principles of Optics* 7th edition (Cambridge University Press, 1999).

[25] W. Ketterle, D. S. Durfee, and D. M. Stamper-Kurn, Proceedings of the International School of Physics "Enrico Fermi", Course CXL, edited by M. Inguscio, S. Stringari, C. E. Weiman (IOS Press, Amsterdam, 1999) pp. 67-176.

[26] P. S. Jessen and I. H. Deutsch, Adv. in At, Mol. and Opt. Phys. **37**, 95 (1996) and references therein.

[27] A. J. Kerman, V. Vuletić, C. Chin, and S. Chu, Phys. Rev. Lett. **84**, 439 (2000).

[28] G. K. Brennen, C. M. Caves, P. S. Jessen, and I. H. Deutsch, Phys. Rev. Lett. **82**, 1060 (1999).

[29] N. F. Mott, Proc. Phys. Soc. A **62**, 416 (1949).

[30] A. van Otterlo and K.-H. Wagenblast, Phys. Rev. Lett. **72**, 3598 (1994).

[31] E. Roddick and D. Stroud, Phys. Rev. B **48**, 16600 (1993).

[32] K. Sheshadri, H. R. Krishnamurthy, R. Pandit and T.V. Ramakrishnan, Europhys. Lett. **22**, 257 (1993).

[33] N. D. Mermin, Phys. Rev. **167**, 250 (1968).

[34] N. D. Mermin and H. Wagner, Phys. Rev. Lett. **22**, 1133 (1966).

[35] P. C. Hohenberg, Phys. Rev. **158**, 383 (1967).

[36] H. A. Jahn and E. Teller, Proc. Roy. Soc. (London) **A164**, 117 (1937).

[37] G. Nienhuis, P. van der Straten and S-Q. Shang, Phys. Rev. A **44**, 462 (1991).

[38] E. Tiesinga, C. J. Williams, F. H. Mies, and P. S. Julienne, Phys. Rev. A, **61**, 063416 (2000).

[39] E. Tiesinga, C. J. Williams, P. S. Julienne, K. M. Jones, P. D. Lett and W. D. Phillips, Jour. of Res. of the N.I.S.T. **101**, 505 (1996).

[40] A. Messiah, *Quantum Mechanics*, Vol. 2, (North-Holland, Amsterdam, 1961).

[41] M. R. Andrews, C. G. Townsend, H. -J. Miesner, D. S. Durfee, D. M. Kurn, and W. Ketterle, Science **275**, 637 (1997).

[42] B. P. Anderson, M. A. Kasevich, Science **282**, 1686 (1998).

[43] D. van Oosten, P. van der Straten, and H. T. C. Stoof, Phys. Rev. A **63**, 053601 (2001).

[44] M. Greiner, I. Bloch, O. Mandel, T. W. Hänsch, and T. Esslinger, Phys. Rev. Let. **87**, 160405 (2001).

[45] J. Javanainen, Phys. Rev. A **60**, 4902 (1999).

[46] K. Burnett, M. Edwards, C. W. Clark, and M. Shotter, J. Phys. B **35**, 1671 (2002).

[47] J. O. Andersen, U. Al Khawaja, and H. T. C. Stoof, Phys. Rev. Lett. **88**, 070407 (2002); U. Al Khawaja, J. O. Andersen, N. P. Proukakis, and H. T. C. Stoof, Phys. Rev. A. **66**, 013616 (2002); Phys. Rev. A **66**, 059902(E) (2002).

[48] F. Dalfovo, S. Giorgini, and L. P. Pitaevskii, Rev. Mod. Phys. **71**, 463 (1999).

[49] L.-M. Duan, E. Demler, and M. D. Lukin, Phys. Rev. Lett. **91**, 090402 (2003).

[50] L. Santos, M. A. Baranov, J. I. Cirac, H.-U. Everts, H. Fehrmann, and M. Lewenstein, cond-mat/0401502 (2004).

[51] M. Kozuma, L. Deng, E. W. Hagley, J. Wen, R. Lutwak, K. Helmerson, S. L. Rolston, and W. D. Phillips, Phys. Rev. Lett. **82**, 871 (1998)

[52] D. M. Stamper-Kurn, A. P. Chikkatur, A. Görlitz, S. Inouye, S. Gupta, D. E. Pritchard, and W. Ketterle, Phys. Rev. Lett. **83**, 2876 (1999)

[53] G. Grynberg, and C. Robiliard, Phys. Rep. **355**, 335 (2001).

[54] J. Zinn-Justin, *Quantum Field Theory and Critical Phenomena* (Oxford, New York, 1989).

[55] J. R. Schrieffer, *Theory of Superconductivity* (W. A. Benjamin, Inc., New York, 1964).

[56] L. van Hove, Phys. Rev. **89**, 1189 (1953).

[57] T. Stöferle, H. Moritz, C. Schori, M. Köhl, and T. Esslinger, Phys. Rev. Lett. **92**, 130403 (2004).

[58] A. M. Rey, P. B. Blakie, G. Pupillo, C. J. Williams, and C. W. Clark, cond-mat/0406552 (2004).

Samenvatting

Abstract

In de studie naar de structuur van de materie sluiten fysici gassen en zelfs individuele atomen op om hun eigenschappen te kunnen bestuderen. In dit proefschrift worden optische roosters beschreven, waarin atomen in een periodieke structuur worden vastgehouden met behulp van staande lichtgolven. Voor de beschrijving van optische roosters zijn technieken uit de atoomfysica, de vaste-stof fysica en de fysica van de gecondenseerde materie nodig.

Optische roosters

Een optisch rooster bestaat uit atomen die zijn opgesloten in een staande golf, die gemaakt wordt met behulp van laserbundels. Door de wisselwerking tussen het licht en de atomen worden zij aangetrokken naar de maxima of de minima van de intensiteit van het licht, afhankelijk van de verstemming van het licht ten opzichte van de resonantie frequentie van het atoom. Door licht te gebruiken met een hoge intensiteit en een grote verstemming, kan een situatie worden bereikt waarin de atomen een kracht ten gevolge van de wisselwerking voelen, maar nagenoeg geen licht meer verstrooien. In dit geval kunnen we spreken over een conservatieve kracht en mogen we een potentiaal toekennen aan deze kracht. Dan spreken we over een optisch rooster.

Door een geschikte configuratie van laserbundels te kiezen is het mogelijk om één, twee en drie-dimensionale optische roosters te maken. In een één-dimensionaal rooster ondervinden de atomen in één richting een periodieke potentiaal met een rooster afstand ter grootte van de helft van de golflengte van het licht. Als het laserlicht rood is verstemd, worden

de atomen in de loodrechte richtingen opgesloten binnen een afstand ter grootte van de diameter van de laserbundel. Als het laserlicht blauw is verstemd moet ook een magneetval worden gebruikt om de atomen in de loodrechte richting op te sluiten.

Een één-dimensionaal optisch rooster is relatief makkelijk te gebruiken. Een wolk van thermische atomen, gevangen in een magneto-optische val, heeft een dichtheid hoog genoeg om een één-dimensionaal optisch rooster te laden met enkele atomen per roosterpunt. Zo'n één-dimensionaal rooster heeft echter één nadeel: De opsluiting in de richtingen loodrecht op de laserbundels is zwak. De sterkte van deze opsluiting wordt namelijk bepaald door de diameter van de laserbundel, die typisch in de orde van enkele tientallen micrometers is. Dat betekent dat atomen opgesloten op een roosterpunt in de loodrechte richtingen een zeer grote afstand tot elkaar kunnen hebben in vergelijking met de dracht van hun onderlinge interactie, zodat dit systeem niet bijzonder geschikt is om de interactie tussen de atomen te bestuderen. Dit kan worden verholpen door met behulp van meer laserbundels een drie-dimensionaal rooster te maken. Dit brengt echter een nieuw probleem met zich mee. Doordat het aantal roosterpuntten van een drie-dimensional rooster veel hoger is dan voor een één-dimensionaal rooster is het niet langer mogelijk om enkele atomen per roosterpunt op te sluiten. Er wordt in dit geval slechts een klein deel van de roosterpunten bezet door een atoom. Om dit probleem te verhelpen dient het rooster te worden geladen uit een veel koudere en dichtere wolk van atomen dan die in een magneto-optische val.

Bose-Einstein condensatie

In een experimentele opstelling kunnen atomen uit een magneto-optische val worden geladen in een magnetische val, mits ze het juiste magnetische moment hebben. De atomen kunnen vervolgens verder worden verdicht door de sterkte van de magneetval te verhogen. Doordat hier sprake is van een gesloten systeem, moet de temperatuur van de atomen daardoor oplopen. Dit is een gevolg van de stelling van Liouville die stelt dat in een gesloten systeem het aantal bezette toestanden niet kan veranderen. Dat betekent, dat als de atomen in een kleinere ruimte worden opgesloten, hun gemiddelde snelheid zal verhogen en een hogere gemiddelde snelheid correspondeert met een hogere temperatuur. Er kunnen nu meer deeltjes per roosterpunt worden geladen, maar doordat hun snelheid is verhoogd,

kunnen ze nog steeds niet goed bestudeerd worden.

Echter in een magneetval is het mogelijk om zeer effectief te koelen met behulp van verdampingskoelen. De atomen zijn in de magneetval opgesloten, omdat hun magnetisch moment in de juiste richting staat. Het is echter mogelijk de atomen in een toestand te brengen, waarbij het magnetisch moment tegengesteld is en de atomen uit de magneetval worden geduwd. Dit kan met een radio-frequent (rf) magnetisch veld, dat loodrecht staat op het veld van de magneetval. Het proces zal plaatsvinden, op een positie waar de frequentie van dit veld gelijk is aan de Zeeman verschuiving die een atoom ondervindt. Omdat de Zeeman verschuiving aan de rand van de val groter is dan in het centrum, is het mogelijk voornamelijk de atomen aan de rand van de val te verwijderen zonder de atomen in het centrum te beïnvloeden. Doordat de atomen aan de rand de atomen zijn met de hoogste energie, kunnen we op deze manier de gemiddelde energie per atoom laten afnemen. Als in de magneetval twee atomen met elkaar botsen, is er een kans dat één van beide atomen bij die botsing een energie krijgt die zo hoog is dat het atoom door het rf-veld wordt verwijderd. Als de dichtheid van atomen hoog is, zodat er veel van deze botsingen tussen atomen plaatsvinden, zal door de botsingen en de aanwezigheid van het rf-veld de temperatuur van de atomen dalen. Dit proces staat bekent als verdampingskoelen en is volstrekt analoog aan het proces waardoor een kopje koffie afkoelt. In de praktijk duurt dit proces te lang en wordt tijdens het verdampingskoelen het rf-veld langzaam verlaagd om het proces te versnellen.

De atomen die we hier beschrijven, hebben een zogenaamd bosonisch karakter. Hierdoor geldt dat de kans, dat een atoom een bepaalde toestand gaat bezetten, groter wordt naarmate er meer identieke atomen al in die toestand zitten. In een thermisch gas is de bezettingsgraad van toestanden lager dan één deeltje per toestand, waardoor het bosonische karakter nagenoeg geen rol speelt. Doordat bij verdampingskoeling de temperatuur echter steeds wordt verlaagd en de dichtheid wordt verhoogd, komt er een moment dat er één deeltje in de grondtoestand terecht komt. Vanaf dat moment wordt de kans aanzienlijk dat bij botsingen tussen warme atomen in de val één van beide botsingspartners in de grondtoestand terecht zal komen. Door dit proces zal een groot gedeelte van de atomen in de grondtoestand van de val terecht komen. In dat geval spreken we van Bose-Einstein condensatie.

Als een Bose-Einstein condensaat in een één-dimensionaal optisch rooster wordt geladen is de dichtheid hoog genoeg om honderden atomen per roosterpunt te kunnen vangen. Dit betekent dat er in feite een hele verzameling van Bose-Einstein condensaten is gemaakt, waartussen een koppeling is door middel van tunneling van atomen door de potentiaal-barrieres van het rooster. Deze koppeling is instelbaar door de intensiteit van de laserbundel te veranderen. Het is ook mogelijk om een drie-dimensionaal rooster te laden met enkele atomen per roosterpunt.

Quantum fase overgangen

Het overgaan van een normaal gas naar een Bose-Einstein condensaat is een zogenaamde tweede-orde fase overgang. Technisch gesproken betekent dit dat de ordeparameter van de fase overgang, in dit geval de condensaatdichtheid, continu maar niet differentieerbaar veranderd. Deze fase overgang kan worden gemaakt door de temperatuur te verlagen, of door bij constante temperatuur de totale dichtheid te verhogen.

Als dit Bose-Einstein condensaat is overgeladen naar een optisch rooster, kan er nog een fase overgang plaatsvinden. Als het rooster ondiep is, kunnen de atomen vrij tunnelen van de ene roosterpunt naar de andere, waardoor informatie over de complexe fase van de golffunctie van het condensaat kan worden uitgewisseld tussen alle roosterpunten. Hierdoor is er in het rooster sprake van fase correlaties op lange afstanden. Dit betekent dat de atomen in het rooster zich bevinden in een superfluïde toestand, zodat de atomen wrijvingsloos door het rooster kunnen bewegen. Als echter het rooster dieper wordt gemaakt, wordt het tunnelen moeilijker voor de atomen. Daarnaast wordt de energie ten gevolge van de interactie tussen deeltjes steeds hoger; de atomen worden immers in een roosterpunt dichter op elkaar geperst. De combinatie van deze twee processen zorgt ervoor, dat de atomen voor een bepaalde roosterdiepte vastvriezen in hun roosterpunt en niet langer door het rooster bewegen. De atomen in het rooster zijn dan in een isolerende toestand. Dit gebeurt al bij een eindige waarde van de roosterdiepte: er is hier sprake is van een fase overgang. De fase overgang wordt echter niet gedreven door extensieve grootheden als de temperatuur en de dichtheid, maar door de diepte van de potentiaal. De fase overgang vindt formeel alleen plaats als de temperatuur gelijk is aan het absolute nulpunt. De fase overgang heeft daardoor een fundamenteel ander karakter dan de fase overgang van een normaal gas naar een Bose-Einstein conden-

saat: Bij de laatste vindt de fase overgang plaats door thermodynamische processen, bij de eerste vindt de fase overgang juist alleen plaats op het punt waar thermodynamische processen geen rol meer spelen. Dit type fase overgang staat bekent als een quantum fase overgang.

Dit proefschrift

Bij de bestudering van de bovengenoemde fase overgang wordt gebruik gemaakt van het zogenaamde Bose-Hubbard model. Dit model beschrijft het gedrag van bosonen in een rooster in termen van de tunneling waarschijnlijkheid en de interactie-energie. In hoofdstuk 2 wordt beschreven hoe deze parameters afhangen van experimentele parameters, zoals de golflengte en intensiteit van het roosterlicht, en van microscopische parameters, zoals de massa en de botsingseigenschappen van het atoom. Daarnaast worden configuraties besproken, waarmee optische rooster met verschillende kristallografische structuren kunnen worden gemaakt. Omdat wij deze systemen experimenteel willen realiseren, wordt er hard gewerkt aan een opstelling om Bose-Einstein condensatie te bereiken in een damp van natrium atomen. In deze opstelling worden de natrium atomen eerst gevangen in een magneto-optische val, waarna ze worden overgeladen in een magnetische val. Omdat deze wolk van atomen met het blote oog niet zichtbaar is, beelden we de wolk af door er een korte laserpuls doorheen te schijnen. Met behulp van een speciale camera kan de schaduw van de wolk worden gemeten. Op deze manier kunnen we meten dat we enkele honderden miljoenen natrium atomen kunnen verzamelen. Nu kan worden begonnen aan de verdampingskoeling van deze atomen, maar daar zijn bij het schrijven van dit proefschrift nog geen resultaten over te melden.

Vanaf hoofdstuk 4 worden theoretische resultaten gepresenteerd. In hoofdstuk 4 wordt een theorie opgesteld waarmee we voorspellen onder welke experimentele omstandigheden de quantum fase overgang kan worden waargenomen. Ook bekijken we hoe de energie van een deeltje in de isolerende toestand wordt beïnvloed door de interactie met alle andere deeltjes. In hoofdstuk 5 beschouwen we één- en twee-dimensionale roosters, waarin een condensaat van vele honderden atomen op ieder roosterpunt is opgesloten. We laten zien dat de fase overgang in dit geval veel moeilijker is te realiseren, doordat de condensaten op ieder roosterpunt zich uitbreiden in de richtingen loodrecht op het rooster. In hoofdstuk 6 stellen we een

experiment voor om de energie van een deeltje in de isolerende toestand te bepalen. Door twee laserbundels met een klein verschil in frequentie en met een kleine onderlinge hoek op de atomen te laten vallen, kunnen we een kleine hoeveelheid energie en impuls overdragen op de atomen. Door te meten onder welke hoeken en bij welke frequentie verschillen er een interactie plaatsvindt kunnen de eigenschappen van de isolerende toestand met een hoge nauwkeurigheid worden bepaald. Bij de berekening in hoofdstuk, moeten bepaalde correctie termen worden uitgerekend. Een formele afleiding van deze termen wordt gegeven in hoofdstuk 7.

Vooruitblik

Experimenten met atomen in een optisch rooster hebben laten zien dat het mogelijk is om een quantum fase overgang waar te nemen in een laboratorium. Het zou dus ook mogelijk kunnen zijn om ook andere quantum fase overgangen waar te nemen door bijvoorbeeld atomen met verschillende spin toestanden in het rooster te vangen. Ook zijn er voorstellen om in één-dimensionale optische roosters de excitaties van de condensaten op ieder roosterpunt te meten en hun gedrag te onderzoeken als de koppeling tussen de condensaten sterker of zwakker wordt gemaakt. Het wordt bijvoorbeeld verwacht dat het gedrag van vortices in zo'n verzameling gekoppelde condensaten interessante verschijnselen zal opleveren, doordat de vortices in de verschillende condensaten een effectieve koppeling ondervinden door tunneling van atomen van een condensaat naar naburige condensaten. Hierdoor kunnen deze vortices zich afhankelijk van de diepte van de roosterpotentiaal al dan niet als één lange vortex gedragen. Daarnaast bieden optische roosters de mogelijkheid om de botsingseigenschappen van de atomen te bestuderen onder unieke omstandigheden. Met behulp van foto-associatie kunnen quasi-moleculen worden gemaakt met grote interatomaire afstanden in vergelijking met echte moleculen. Deze quasi-moleculen worden gemaakt uit paren van atomen die door het rooster zeer dicht op elkaar zijn opgesloten in vergelijking met atomen in een Bose-Einstein condensaat. Hierdoor vervaagt in het rooster de grens tussen vrije atomen en moleculen.

Curriculum Vitae

Ik ben geboren op 23 januari 1976 te Utrecht. Van 1988 tot en met 1995 doorliep ik het Voortbereidend Wetenschappelijk Onderwijs aan het Niels Stensen College, eveneens in Utrecht. In 1995 begon ik met een studie Natuurkunde aan de Universiteit Utrecht, die ik in 2000 met succes heb afgesloten in de richting Experimentele en Theoretische Natuurkunde op respectievelijk de onderwerpen "*Ionization and mechanics in a He* MOT*" o.l.v. Drs. M. van Rijnbach, Dr. M. Pieksma, en Prof. dr. P. van der Straten en "*Quantum phases in an optical lattice*" o.l.v. Prof. dr. P. van der Straten en Prof. dr. ir. H. T. C. Stoof. Hierna ben ik begonnen met het promotie onderzoek wat geleid heeft tot het schrijven van dit proefschrift. Tijdens mijn promotie ben ik naar diverse conferenties geweest, waaronder:

"Cold Molecules 2001: Coherent control and cold molecules",
Gif-sur-Yvette, France, 21-25 oktober 2001.
"Cold Molecules 2002: Ultracold molecules and Bose-Einstein condensation",
Les Houches, France, 3-8 maart 2002.
"Obergurgl Meeting 2003, Quantum Optics Innsbruck",
Obergurgl, Austria, 23 februari - 1 maart 2003.
"Bose-Einstein condensation: from Atoms to Molecules",
Durham, UK, 30 maart - 3 april 2004,

Daarnaast heb ik het voorrecht gehad om een zomerschool te mogen bijwonen aan het Como meer:

International School of Physics "Enrico Fermi" COURSE CVLXVIII:
"Experimental Quantum Computation and Information",
Varenna, Italie, 17-27 juli 2001.

Ook heb ik verschillende malen mijn werk gepresenteerd in de vorm van

mondelinge presentaties, waaronder:

"Quantum phases in an optical lattice",
Najaarsvergadering NNV sectie AQ Lunteren 2000 (16 november 2000).
Landelijk Seminarium Statistische Mechanica 2001 Leiden(15 februari 2002).
Group Meeting Labratoire Kastler Brossel, Paris (2 februari 2004).
Group Meeting Ultracold Quantum Gases, Mainz (18 maart 2004).

Vanaf 1 oktober 2004 zal ik als post-doctoraal onderzoeker aan het werk gaan in de groep van Prof. dr. I. Bloch, aan de Johannes Gutenberg Universiteit in Mainz (Duitsland).

Publications

- *Quantum phases in an optical lattice*
  D. van Oosten, P. van der Straten, and H. T. C. Stoof,
  Phys. Rev. A **63**, 053601 (2001).

- *Thermal fluctuations and the superfluid to Mott insulator transition*
  D. van Oosten, P. van der Straten, and H. T. C. Stoof,
  Phys. Rev. A **67**, 033606 (2003).

- *Ultracold atoms in optical lattices*
  D. B. M. Dickerscheid, D. van Oosten, P. J. H. Denteneer, and H. T. C. Stoof,
  Phys. Rev. A **68**, 043623 (2003).

- *Inelastic light scattering from an Mott insulator*
  D. van Oosten, D. B. M. Dickerscheid, B. Farid, P. van der Straten,
  and H. T. C. Stoof, submitted to Phys. Rev. Lett.

Dankwoord

Een dankwoord schrijven is een drama, als je niet iemand vergeet, spel je wel iets verkeerd. Toch is het een belangrijk deel van ieder proefschrift en ik heb dus ook mijn best gedaan om iedereen die heeft bijgedragen aan mijn promotie op een rijtje te zetten.

Om het geheel een beetje in een causaal verband te gieten zal ik beginnen met het bedanken van mijn ouders. Als ik jullie hier echt zou gaan bedanken voor alles wat jullie voor me hebben gedaan, zou dit dankwoord te lang worden. Laat ik volstaan met hetgeen wat in mijn ogen (naast de talloze financiële injecties in mijn scholing/studie) het belangrijkste is geweest wat ik van jullie heb meegekregen, namelijk nieuwsgierigheid. Jullie hebben mij laten zien dat het leuk is om dingen uit te zoeken. Of het om de binnenkant van een verbrandingsmotor ging of om computer programmeren, jullie hebben er altijd alles aan gedaan om mijn nieuwsgierigheid te prikkelen.

De volgenden in het rijtje zijn mijn beide promotoren. Peter maakte ik voor het eerst mee als docent van het vak moderne experimentele methoden en van Henk kreeg ik thermische en statistische fysica. Doordat het werk van Peter mij zo interessant leek en doordat Henk erop stond dat je de natuur alleen echt kon doorgronden als je een theoretische achtergrond hebt, heb ik besloten om het dan maar allebei te doen. Ik heb van dat besluit nooit spijt gehad en ik ben jullie dus ook zeer dankbaar dat jullie het voor mij hebben mogelijk gemaakt om de keuze tussen theorie en experiment zolang mogelijk uit te stellen.

Als experimenteel fysicus kun je niet zonder technici. Ik heb het genoegen gehad om met veel technici samen te kunnen werken. Allereerst de mannen van het IGF. Op Gerard kon ik tijdens mijn afstudeeronderzoek al rekenen. Het werk dat John, Manfred en Mari voor ons hebben verzet is enorm, zonder hun vakmanschap was onze opstelling er nooit gekomen. Als

groep hebben wij ook het geluk dat er een hele verzameling van technici op onze verdieping aanwezig is, die wil ik natuurlijk ook allemaal bedanken. Hans staat altijd klaar om mee te denken en te helpen met de lasers. Dat laatste geldt natuurlijk ook voor Cees. Jitse heeft met al zijn advies en slimme oplossingen een hoop van onze vacuüm-zorgen opgelost. Bij Paul kun je altijd aankomen als er heel snel een constructief probleem moet worden opgelost. Frits, jij hebt de hele opstelling voor ons in elkaar gesoldeerd. Als jouw machtige hand het wil, ligt het hele experiment stil.

Sinds een paar jaar delen wij als laserkoelers een programma met de groep van Jaap. Het was leuk om op het AU-seminar ideëen uit te wisselen met de snelle jongens van de andere kant van de gang en de andere laserkoelers Driss en Lennart. Ook gaat mijn dank uit naar de hele BEC-groep bij theorie. Wie niet mogen ontbreken in dit lijstje zijn de studenten die bij mij hebben gewerkt: Elmar en het dynamische duo Tart en Bim. Daarnaast zou ik graag alle promovendi en postdocs noemen die ik mee heb gemaakt bij atoomfysica, maar dat zou te lang duren. Ik wil daarom volstaan met de helium-groep: Mark, Jan, Geraldine en natuurlijk Michiel.

Het belangrijkste zijn de directe collega's. Bij theorie waren dat Dennis en Jani die mij menigmaal als kamergenoot hebben moeten tolereren. In de experimentele groep waren dat natuurlijk Carolijn, Johny, Richard en Erik. Ik wens jullie veel plezier en sterkte met de opstelling, we hebben met z'n allen een leuk staaltje werk geleverd, nu wordt het tijd om de vruchten te gaan plukken. Erik, jij bent de volgende die promoveert, veel succes met de laatste loodjes en met de keuzes die je hierna moet gaan maken.

Als afsluiting wil ik mijn lieve vrouw Marianne bedanken. Je bent er altijd voor me geweest, ook al is een promovendus in zijn laatste jaar niet altijd de leukste echtgenoot.